DEVELOPMENT OF A PIEZOELECTRIC TOOL ACTUATOR FOR PRECISION TURNING

by

Andrew Stanley Woronko
B.A.Sc. (Mechanical Engineering), 1999
University of Waterloo

A THESIS SUBMITTED IN PARTIAL FULFILLMENT OF
THE REQUIREMENTS FOR THE DEGREE OF
MASTER OF APPLIED SCIENCE

in

THE FACULTY OF GRADUATE STUDIES
MECHANICAL ENGINEERING

We accept this thesis as conforming
to the required standard

THE UNIVERSITY OF BRITISH COLUMBIA

December 2001

In presenting this thesis in partial fulfillment of the requirements for an advanced degree at the University of British Columbia, I agree that the Library shall make it freely available for reference and study. I further agree that permission for extensive copying of this thesis for scholarly purposes may be granted by the head of my department or by his or her representatives. It is understood that copying or publication of this thesis for financial gain shall not be allowed without my written permission.

DEPARTMENT OF MECHANICAL ENGINEERING

The University of British Columbia

2324 Main Mall

Vancouver, BC, Canada

V6T 1Z4

Date: December 17, 2001.

Abstract

Precision turning as an alternative to conventional finish machining operations of cylindrical components offers significant reductions in manufacturing cost and cycle time. In this thesis the development of a piezoelectric tool actuator for precision turning of shafts is presented. A review of research conducted in the areas of precision turning, piezoelectric actuator development, and micropositioning systems design is presented. Mounted to a conventional turning machine, the tool actuator overcomes the limitations of machine tool feed drives by providing precise control of the finishing depth of cut. In this manner part tolerances are achieved in one setup on a single machine, without the need for subsequent finishing operations.

Design of the actuator system was driven by constraints on motion range and resolution, size, and structural properties. Tool motion is provided through the use of a high voltage piezoelectric translator housed within a monolithic solid flexure. A capacitive position sensor provides feedback of tool motion to the controller. In order to be practical in an industrial setting the actuator design is compact, and provides an interface for exchangeable tooling. The specifications of the actuator are 36 micron stroke, 370 N/micron stiffness, and 3200 Hz natural frequency (radial direction). A sliding mode control scheme was implemented to regulate tool position, and reject disturbances due to cutting forces and actuator non-linearity.

The actuator was experimentally verified through machining tests in both laboratory and industrial sites. Results showed that positioning resolution of 20 nm is achievable in precision finishing, and that the commanded controller position was accurately reflected on the machine workpiece. Average surface roughness for 4340 steel (36-40 HRC) was less than 0.3 microns, and less than 0.15 microns for hardened 4320 steel (58-62 HRC).

Table of Contents

List of Figures

List of Tables

Acknowledgments

Completion of this work would not have been possible without the support of my colleagues, friends, and family. Firstly I wish to thank my research supervisor, Dr. Yusuf Altintas, for his insightful input and guidance, and most importantly for his confidence in my work throughout the duration of my research. I wish to express my gratitude to my colleagues in the Manufacturing Automation Laboratory at UBC, as not only did they offer their constant help with technical issues, but provided a highly enjoyable and rewarding graduate study experience.

This work has been funded by the Institute for Robotics and Intelligent Systems (IRIS), Pratt and Whitney Canada, and Caterpillar Inc. I acknowledge the support of Manufacturing Engineering Development at Pratt and Whitney Canada, and wish to especially thank Dr. Serafettin Engin for his hard work and assistance in preparing and conducting cutting test experiments. Evaluation of the actuator system at the Caterpillar Technical Center was supported by the Advanced Production Technologies division.

Finally I wish to express my sincere gratitude to my family, who have always encouraged me, provided meaningful advice, and their unquestioned support. This work is dedicated to them.

Nomenclature

a	depth of cut
b	width of a solid circular hinge
B_1, B_2	sensor dynamics parameters
C	damping of the actuator system
$\hat{C}$	estimated damping of the actuator system
d	distance between sensor plates
d_o	nominal sensor displacement setting
$\hat{d}$	disturbance estimate
δ_{GU}	required displacement of Guiding Unit flexures for PZT preload
δ_{CU}	required displacement of Clamping Unit flexures for PZT preload
ΔL_o	nominal stroke of a piezostack actuator
ΔL	reduced stroke of a piezostack actuator
E	modulus of elasticity
f	feed rate
f_n	natural frequency
f_N	Nyquist frequency
f_s	control sampling frequency
F_d	disturbance force on the actuator
F_f	cutting force in feed direction
$F_{friction}$	static friction force generated by Clamping Units
F_i	input force to the actuator
F_L	load required to displace flexures at full stroke

F_N	normal force exerted by Clamping Units
F_M	measured radial force for feedforward force control
$F_{P,GU}$	Guiding Unit piezostack preload
$F_{P,CU}$	Clamping Unit piezostack preload
F_{RES}	resultant maximum load on flexures
F_r	cutting force in radial direction
F_t	cutting force in tangential direction
FS	factor of safety
FS_1	force measured by force sensor 1
FS_2	force measured by force sensor 2
h	uncut chip thickness
h_{min}	minimum uncut chip thickness for chip formation
G_{ff}	feedforward force transfer function
G_{xx}	actuator direct transfer function in x direction
G_{yy}	actuator direct transfer function in y direction
G_{zz}	actuator direct transfer function in z direction
K	stiffness of the actuator system
$\hat{K}$	estimated stiffness of the actuator system
K_A	amplifier gain
K_B	bending stiffness of a solid circular hinge
K_F	gain relating input force to input voltage
K_{FS}	force sensor calibration factor
K_s	feedback gain control parameter
$K_{s,r}$	resultant axial stiffness of a single flexure

K_S	axial stiffness of a solid circular hinge
K_{SF}	calibration factor of the integrated force sensors
K_R	resultant radial stiffness of the actuator
K_t	nominal piezostack stiffness specified by the manufacturer
K_x	resultant radial stiffness of the Guiding Unit flexures
$K_{x,F}$	resultant radial stiffness of a single flexure
$K_{x,FB}$	radial stiffness of a single flexure due to bending
$K_{x,FS}$	radial stiffness of a single flexure due to axial deformation
κ	boolean control parameter which imposed limits on control signal
λ	control parameter which determines dynamics of sliding surface
λ_c	cutoff value for roughness profile filter
m	effective mass of flexures and moving section
m_{eff}	effective mass of moving components
m_{tool}	mass of the tool assembly
m_{ms}	mass of the moving section of the Guiding Unit
m_{PZT}	mass of the piezostack actuator
$m_{f,GU}$	mass of the Guiding Unit flexures
M	mass of the actuator system
$\hat{M}$	estimated mass of the actuator system
M_r	moment on adapter flange due to radial cutting force
M_t	moment on adapter flange due to tangential cutting force
M_f	moment on adapter flange due to feed cutting force
μ	coefficient of static friction for titanium-titanium contact
μ_f	coefficient of friction in the flank region of the tool

n	spindle rotational speed
P	unfiltered surface profile
P_f	frictional power in the flank region of the tool
r	radius of a solid circular hinge
R	filtered surface roughness profile
R	tool nose radius
R_a	average roughness
R_y	maximum peak to valley roughness
R_z	average ten point roughness
ρ	control parameter
S	sliding surface
t	thickness of a solid circular hinge
t_p	bearing ratio
T_s	control sampling period
U	potential energy
U_{out}	output voltage of capacitive sensor
$u(t)$	control signal
V	Lyapunov function
V_c	cutting surface speed
V_f	output voltage from charge amplifier
W	filtered surface waviness profile
W	external work
ω	excitation frequency
$x(t)$	actuator displacement at time t

$\dot{x}(t)$	actuator veloctiy at time t
$\ddot{x}(t)$	actuator acceleration at time t
x_a	actuator displacement
x_d	desired actuator position
$X(s)$	actuator position (Laplace domain)
$X_m(s)$	measured actuator position (Laplace domain)
ζ	damping ratio

AISI	American Iron and Steel Institute
BUE	Built Up Edge
CBN	Cubic Boron Nitride
CNC	Computer Numerical Control
DSP	Digital Signal Processing
D/A	Digital to Analog
EDM	Electrical Discharge Machining
FCE	Fast Cyclic Executive
FE	Finite Element
HRC	Rockwell hardness, C scale
ISO	International Standards Organization
JIS	Japanese Industrial Standards
MAL	Manufacturing Automation Laboratory
PECM	Pulse Electrochemical Machining
PC	Personal Computer
PI	Proportional Integral
PID	Proportional Integral Derivative
PWC	Pratt and Whitney Canada
PZT	Lead-zirconate-titanate
SMC	Sliding Mode Control

Chapter 1

Introduction

Increasing demands for the reduction of the manufacturing costs of precision components has highlighted the need for viable and cost effective alternatives to conventional precision machining strategies. A typical precision shaft machining operation may involve both turning and grinding processes. Rough, semi-finish, and finish machining are first performed on a computer numerically controlled (CNC) turning centre, then a grinding machine is used for fine finishing of the part. It is in this final grinding stage that the part tolerances are commonly achieved. Conventional CNC lathes are hindered by friction and backlash in the feed drives, such that the positioning accuracy of a given axis is limited. The positioning accuracy is different for each machine, but typically a value of 5-20 microns is assumed. It is evident that cylindrical parts requiring high dimensional tolerances of a few microns cannot be manufactured on a conventional lathe, therefore the grinding operation (or turning using a high precision machine) is a necessity.

In a precision turning operation all tolerances are achieved on the turning machine, without the need for grinding. In general turning offers a higher production rate, less capital and tooling costs, and is more environmentally friendly than grinding. Clearly by performing the entire operation on the same machine the cycle time per part is reduced as no machine tool change is necessary. High precision lathes have recently become available to meet precision turning requirements. The main drawback is their high capital cost, which may be difficult to justify for manufacturing plants already possessing conventional turning machines. As well many high precision machines require a special environment providing vibration and thermal isolation, which adds to set up costs on the shop floor.

The alternative is the use of a precise motion tool actuator mounted to a conventional lathe. In this way coarse motion is performed by the turning machine's CNC feed drives, and fine positioning is performed solely by the tool actuator. Commonly piezoelectric actuators are used to deliver fine motion in machining applications. In this work the development of a piezoelectric actuator for precision turning is presented. The actuator is intended as a plug-in to a conventional turning machine, whereby the lathe feed drives execute coarse motion, and the actuator regulates the tool position during finishing. The complete system has been developed, including electromechanical design and analysis, manufacturing, and assembly of the actuator, followed by system identification and controller design, and finally experimental testing in both laboratory and industrial settings.

The thesis is divided into six chapters. Chapter 2 presents a review of research conducted in the areas of piezoelectric tool actuator development and the design of micropositioning systems. Precise positioning alone cannot guarantee achieving part tolerances in the turning process. The final shape is affected by the cutting tool geometry and material, machine tool rigidity, workpiece material, and the cutting conditions; specifically cutting speed and feed rate. Thus an overview of the turning process, surface roughness generation in turning, and precision turning of hardened steels is provided, as well as a brief discussion of form errors in turning. Careful consideration must be paid to each of these areas in order to guarantee the system meets precision machining requirements.

Chapter 3 presents an overview of the design requirements and constraints, followed by the general and detailed component design. The actuator must provide a sufficient range of motion, while maintaining high positioning resolution. As well the design must have adequate mechanical properties, such as high stiffness and natural frequency, and compact size. The main features of the design are the use of a high voltage piezoelectric translator, solid flexures to transmit motion to the tool free of friction and backlash, exchangeable tooling, and the option to clamp the tool once positioned. The analysis stages are outlined, and analytical and numerical models are

developed to determine the mechanical properties of the solid flexures. Properties of the feedback sensor assembly, support plates, and clamping units are presented as well.

The identification of the manufactured and assembled actuator system is presented in Chapter 4. This includes the direct output displacement to input force transfer functions, in all three translational directions, for both the unclamped and clamped modes of operation. Using the transfer function in the radial direction the system model is developed for controller design. A sliding mode controller is derived and implemented, and the resulting response is discussed. The non-linearities associated with piezoceramic actuators are quantified, they include hysteresis and creep. Finally the instrumentation for closed loop digital control is described, and the properties of the feedback sensor are discussed.

To evaluate the system, experimental testing was performed at the Manufacturing Automation Laboratory (MAL) at UBC, and with two industrial partners; Pratt and Whittney Canada and Caterpillar Inc. The objectives of the experiments were to determine the achievable positioning resolution of the controller while machining, the relationship between the commanded control input and the actual workpiece surface profile, and the achievable surface roughness for both medium and high hardness steels. The usefulness of the actuator system was investigated through implementation at the industrial sites. The obtained results are presented and discussed in Chapter 5.

Finally the major accomplishments of the thesis are summarized in Chapter 6, and recommendations for future work in precision turning with the aid of tool actuators are given.

Chapter 2

Literature Review

2.1. Overview

The economic benefits of single step precision machining, coupled with advancements in machine tool technology and cutting tool materials, have led many researchers to investigate precision turning as an alternative to conventional grinding processes. Tool actuators that can provide precise and accurate positioning during the cutting process have received a great deal of attention, as they offer a low cost alternative to high precision machines for finishing operations. This chapter includes a review of research conducted in the development of piezoelectric tool actuators for precision turning. The achievable positioning accuracies, mechanical properties, and control schemes used are presented for actuator systems related to the current work. Since tool actuators are considered micropositioning systems, related work in micropositioning systems design is presented as well, with emphasis on the design of solid flexure hinges. An overview of the turning process in given, which includes the cutting forces and the effects of tool geometry. The motivation for this work is the limited positioning accuracy of conventional machine tool drives, thus the sources of positioning errors are presented. The quality of the finished part, which is quantified by the form errors and surface roughness, has been studied extensively. The use of both high precision machines and fast tool servos for the reduction of form errors is discussed, and the dominant factors in generation of surface roughness are presented. Recently a great deal of attention has been given to turning of hardened steels instead of grinding. An overview of the research work in this area is provided, including cutting tool materials, chip formation, and surface integrity.

2.2. Precision turning

2.2.1. Tool geometry and forces in turning

The longitudinal turning process, used for reduction of a cylindrical workpiece diameter, is illustrated in Figure 2.1. A cutting tool is positioned to a depth of cut, a, into the workpiece, and fed along the length of the part at feedrate f as the workpiece rotates at speed n. During the machining process the tool experiences loads F_f, F_t, and F_r in the feed, tangential, and radial directions, respectively, while forming the chip. The geometry of the cutting tool is characterized by the back and side rake angles, the side and end cutting edge angles, the side and end relief angles, as well as the tool nose radius (Figure 2.2). The effects of the tool geometry are an important consideration in the development of a precision turning process. The rake angles influence the shear angle in the cutting process, and may be positive, neutral, or zero. Positive rake angles increase the shear angle and thus reduce the cutting forces. As well positive rake angles produces a better surface finish by facilitating chip flow away from the workpiece [1]. The drawback associated with positive rake angles is lowered tool strength, which makes negative rake angle tools suitable for interrupted cutting and turning of hardened materials to reduce the risk of tool fracture. The end cutting edge angle provides clearance between the cutting tool and the newly machined surface, and may cause rubbing of surface if too small. The side cutting edge angle determines the angle of approach of the cutter into the workpiece and aids chip flow away from the tool. A negative angle allows the tool to slowly engage the workpiece thus reducing shock on the tool. For finishing operations a positive side cutting edge angle allows for a higher degree of detail in profiling. The side and end relief angles provide clearance between the tool and machined surface. With increased tool wear the relief angles are reduced, which may adversely affect the surface finish [2]. The tool nose radius affects the achievable surface finish. Based on the geometry a large nose radius produces a better finish, but increased the radial forces which may cause vibration of the workpiece.

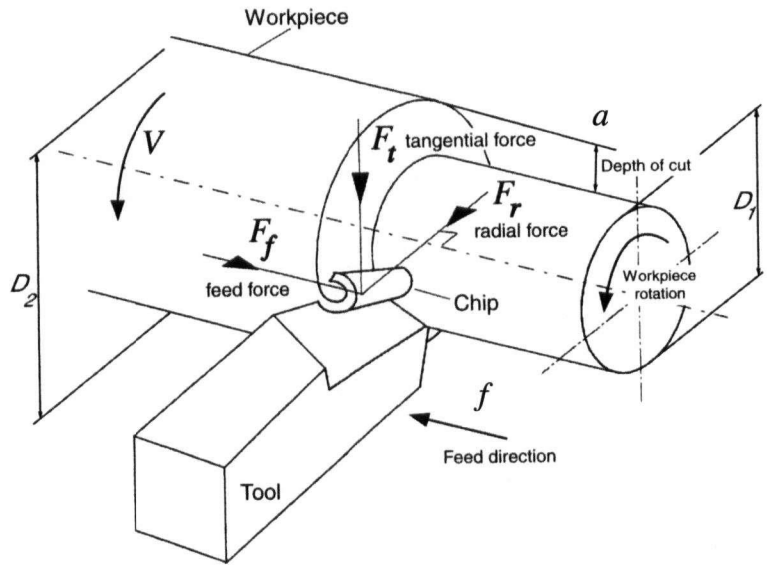

Figure 2.1 : Turning process and cutting forces [1].

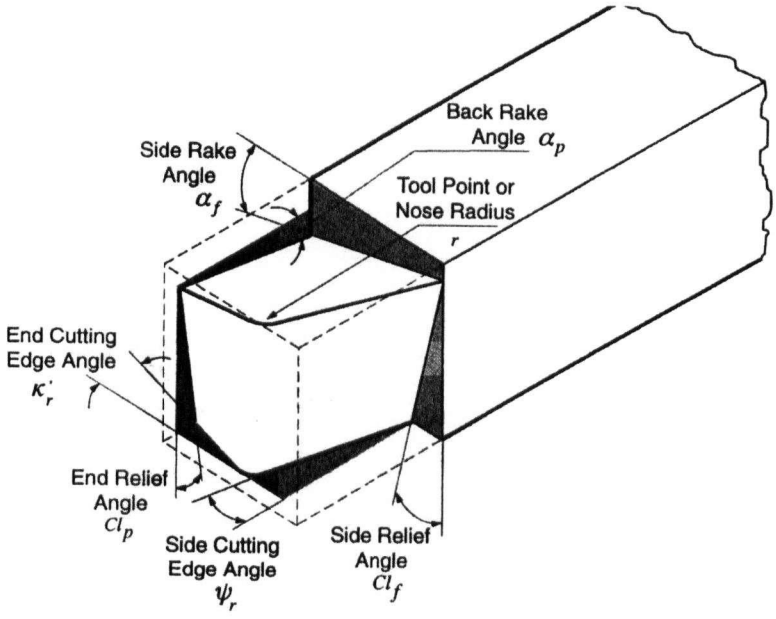

Figure 2.2 : Geometry of the turning tool [1].

2.2.2. Accuracy of machine tool feed drives

The motivation for the development of a precision turning actuator is the limited positioning accuracy of conventional machine tool feed drives. An example of a common feed drive assembly is shown in Figure 2.3. A servomotor provides rotary motion to the leadscrew via either a timing belt or direct transmission. The leadscrew is supported by thrust bearings at either end. The rotary motion of the leadscrew is converted to linear table motion via a preloaded nut. The table rests on friction guideways, which control the direction of motion and absorb static and dynamics forces [1]. Table motion is controlled using feedback from a rotary encoder mounted to the servomotor shaft. Linear position is related to the encoder feedback based on the leadscrew pitch and gear reduction. The actual table position may be affected by backlash and slippage in the timing belt transmission, friction in the bearings, leadscrew, and guides, and backlash in the leadscrew nut and timing belt. Although the feed drive control resolution may be on the order of +/- 1 micron, the actual table positioning accuracy may vary as much as 20 microns. Konig et al [3] suggested conventional lathes are not capable of substituting precision grinding operations. Clearly the achievable accuracy depends on the design and wear of the machine tool used. Vibration and thermal deformation of the leadscrew assembly may also cause deviation in table position.

Linear encoders have recently been introduced to eliminate these effects by measuring the linear table position in relation to the fixed guideways or machine bed [4]. Although the effects of backlash in the feed drive assembly can be eliminated this way, the smoothness of the table motion remains affected by friction and stick-slip. As well linear encoders added to industrial machine tools may not have sufficient resolution for precise positioning, and are commonly susceptible to damage from the chips and cutting fluids used in the machining process. A tool actuator is used to compensate the feed drive inaccuracies by providing the tool motion (for short stroke only) and keeping the machine tool feed drive command fixed, or locking the feed drive possible on some machines. In this way, as long as the desired dimension change is within the

actuator stroke, the positioning is accurate and the delivered motion is smooth, provided the actuator is properly designed.

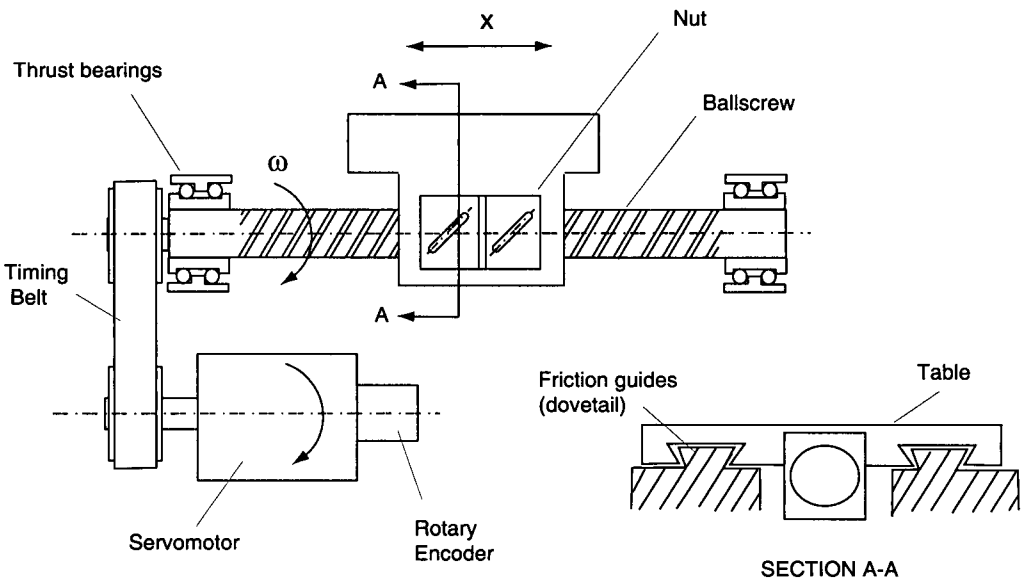

Figure 2.3 : Axis feed drive of a CNC machine tool.

2.2.3. Part quality

The quality of the finished workpiece is judged according to the design specifications, and can be determined by examining the achieved form and surface roughness. For cylindrical components, form can include the dimensional accuracy on diameter, roundness, straightness, and flatness. The surface texture of a part describes both the surface waviness, as well as the surface roughness. The low frequency waviness component, resulting from machine tool properties, can be considered as contributing to form error. Surface roughness, characterized by high frequency variations in the surface profile height, is determined by the machining process conditions.

2.2.3.1. Form errors

Ni [5] attributed CNC machine tool inaccuracy to (1) geometric errors of machine components and structures, (2) errors induced by thermal distortions, (3) deflections caused by cutting forces, and (4) servo errors and NC interpolation errors. These errors limit the achievable form of a machined part. In a single point turning operation the static cutting force in the radial direction deflects the workpiece by an amount determined by the workpiece stiffness at that point. Clearly the workpiece stiffness varies along its length, with a maximum near the chuck and tailstock and minimum in the centre. When the workpiece deflects the effective depth of cut will be reduced, causing a form error on the part. The varying workpiece stiffness causes the form error to vary as well (for constant cutting force), resulting in a barrel shaped part. In order to achieve a certain diameter several passes will be necessary. For finishing operations the depth of cut should be set small to reduce the cutting force and thus workpiece deflection [1]. Alternatively for a repeated process the depth of cut can be dynamically varied during machining to achieve the desired effective depth of cut into the workpiece, provided the workpiece stiffness and cutting forces are known.

During cutting, mechanical work involved in chip formation is converted into heat. Although most heat is conducted into the exiting chip, a percentage is conducted into the workpiece, tool, and machine. With an increase in temperature these components undergo thermal expansion, and the effective depth of cut is increased such that upon cooling the workpiece is overcut. Stephenson et al [6] developed a boundary element method to predict workpiece expansion in turning, and also performed cutting tests. For aluminum cylinders they measured expansion as high as 0.08 mm, and 0.009 mm for hardened steel. The setup and specifications of the machine tool directly affect the turned part. Lathe spindle run-out, or eccentricity, will affect part roundness. Misalignment of the tailstock and spindle will cause the shaft to have a taper along its length. Finally vibration of the tool or workpiece during cutting will cause waviness on the surface of the

machined part. In extreme cases self-excited chatter vibrations can cause severe loading on the machine tool as well as leaving poor surface finish.

Typically form errors produced during the turning process can be removed by subsequent finishing operations such as grinding. High precision lathes offer the ability to overcome many of the sources of form error in turning through optimized machine design for reduced static and thermal deformation, hydrostatic spindles, and aerostatic bearings [7], [8]. Jochman and Wirtz [9] performed cutting tests on 100Cr6 steel (60-62 HRC) using a high precision lathe with hydrostatic bearing systems. They achieved roundness and cylindricity form errors less than 0.2 microns and 1.0 microns, respectively, as well as mean profile height surface roughness less than 1.0 microns. Although it should be noted that the length of cut was 15 mm, thus the squareness of the feed drives would most likely not show any effect. The drawback of high precision machines is the high capital cost, limited workpiece size, and requirements for thermal and vibration isolation. A precision tool actuator is well suited for compensation of such form errors, provided the form errors are known and repeatable. For example, Kim and Kim [10] used a piezoelectric tool actuator to reduce surface waviness from 3.3 microns to 0.3 microns on a diamond turning machine. The dominant mode of the feed drive on a diamond turning machine was compensated by Fawcett [11] using a piezoelectric tool actuator to reduce surface waviness.

2.2.3.2. Surface roughness

In this work only two dimensional surface profiles are considered, as is standard for cylindrical parts. De Chiffre et al [12] presented the 2D parameter conventions for ISO 4287:1997. It is important to distinguish between three profile types; the unfiltered (P) profile, the roughness (R) profile, and the waviness (W) profile. The P profile corresponds to the actual surface profile on the part, and it includes both the roughness and waviness components. In turning the roughness profile represents individual feed marks of the tool along the surface, and varies with high frequency determined by the feedrate. Conversely the waviness profile is a result of tool or work-

piece vibration, and generally occurs at much lower frequency. The R and W profiles can be obtained from the measured P profile using an appropriate filter. Figure 2.4 illustrates how waviness and roughness profiles are obtained from the unfiltered surface profile of a turned workpiece, where the unfiltered profile contains the raw profile compensated for inclination.

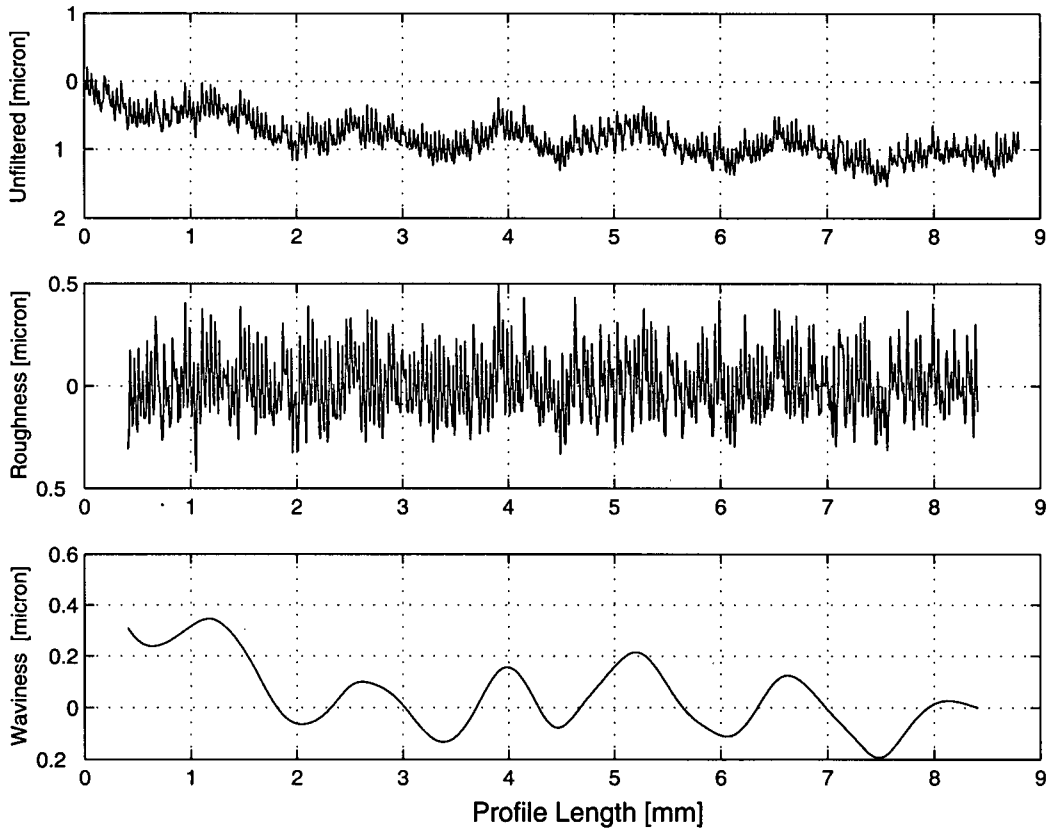

Figure 2.4 : Unfiltered, roughness, and waviness profiles of a turned surface.

Several parameters can be calculated from the roughness profile. The most useful are the arithmetic mean deviation, R_a, the maximum profile height, R_z, the root mean square deviation of the profile, R_q, and the bearing ratio t_p. Note that these parameters can apply to P and W profiles as well (eg. P_a, P_z, P_q). The surface roughness is dependent on several parameters, including the tool properties (material, shape, geometry, wear resistance), cutting conditions (cutting speed, fee-

drate, depth of cut), and workpiece properties (material, hardness) [13], [14], [15]. Note that machine tool deflection, thermal deformation, and positioning accuracy are considered factors which affect part form, not surface roughness. Ideally surface roughness is influenced solely by feed rate and tool nose radius, as illustrated in Figure 2.5. At each revolution of the workpiece the tool with radius R advances a distance equal to the feed rate f, and leaves a feed mark on the surface. Based on the intersection of the circular feed marks the maximum roughness is given by Equation 2.1 [16], as well as an approximation of the average roughness. The equations are based on the assumption that the cutting takes place entirely on the nose radius of the tool, such that the tool angles do not affect the geometry of the feed mark. This is common practice in finishing operations where the depth of cut is small. The maximum roughness for generalized geometry and cutting conditions have been presented by Jun [13]. In practice the achieved surface deviates from the ideal surface of Figure 2.5. The challenge in precision turning is thus to achieve a surface finish as close to the ideal surface as possible.

$$R_y = \frac{f^2}{8R}, \quad R_a \approx \frac{f^2}{32R} \tag{2.1}$$

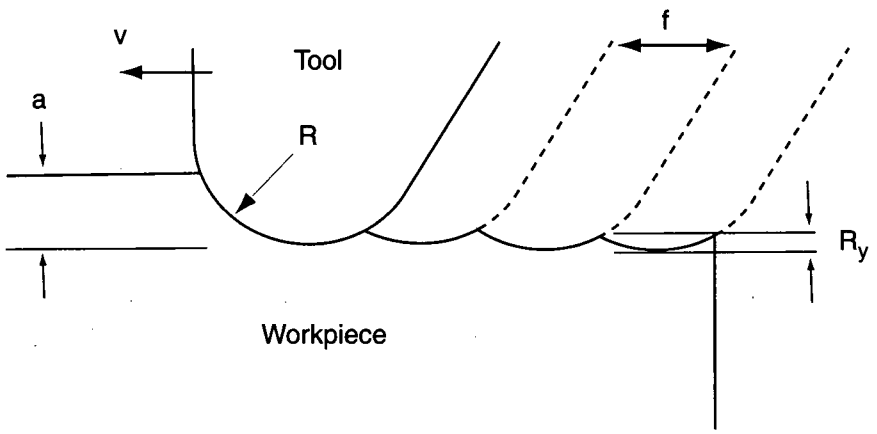

Figure 2.5 : Feed marks left on the workpiece surface during the turning process.

The existence of tool wear will have an adverse effect on the achievable surface finish. Wear in the flank of the tool, effectively decreasing the relief angle, can cause increased rubbing of the tool against the newly machine surface [1]. Wear along the cutting edge, such as grooving or notching, will cause a repeated pattern of spikes to appear in the roughness profile. It has been observed that a groove at the trailing edge of the tool can form, which leads to increased feed mark height [14], [17], [18]. Built up edge (BUE) can occur when the cutting speed is too low. In this case softened material welds to the front of the tool edge, and changes the effective undeformed chip thickness [14], [19]. This causes an undesirable surface finish, as the BUE periodically leaves with the chip and forms again. Increasing the cutting speed serves to form a continuous chip free of BUE [13]. El-Wardany et al [15] observed that increasing the cutting speed in turning of AISI 1552 hardened steel lowered the average roughness, especially at low feedrate. As well it was determined that depth of cut had a minimal effect on roughness. Jun [13] noted that as the cutting speed is increased further roughness increased, which was attributed to higher temperatures causing rapid wear and softening of the work material. Typically a cutting fluid is used to reduce temperatures on the tool and in the work zone, and to disperse small particles which may otherwise weld to the surface of the tool. Use of cutting fluids also reduce the amount of friction on the rake face and in the flank of the tool, which generally improves the surface finish.

The phenomenon of material side flow in finish turning of hardened steels was investigated by Kishawy and Elbestawi [17], as well as El-Wardany et al [15], [20]. Material side flow has a detrimental effect on the surface finish, and is characterized by two mechanisms. In the first material is squeezed between the tool flank and newly machine surface when the uncut chip thickness, h, is less than a minimum value, h_{min}. The second mechanism is the flow of plastified material in the cutting zone through the tool via a worn trailing edge. The minimum chip thickness determines whether a chip is formed through shearing, and is affected by many factors such as tool geometry and material, work material, and cutting speed. When the chip thickness is less

than h_{min}, the work material is plastically and elastically deformed (often termed "ploughing"), and no cutting takes place. Rather than being carried away from the work zone as a chip, the plastified material is left on the surface of the workpiece, known as material side flow. The material can be squeezed by the tool in both the feed and tangential directions, resulting in a surface finish which deviates from the ideal. The fraction of the chip area which exceeds the minimum chip thickness increases with decreasing feedrate f, and increasing tool nose radius R, as depicted in Figure 2.6. Chen [18] concluded that material flow was reduced by increasing the workpiece hardness, due to the reduced plasticity of the material.

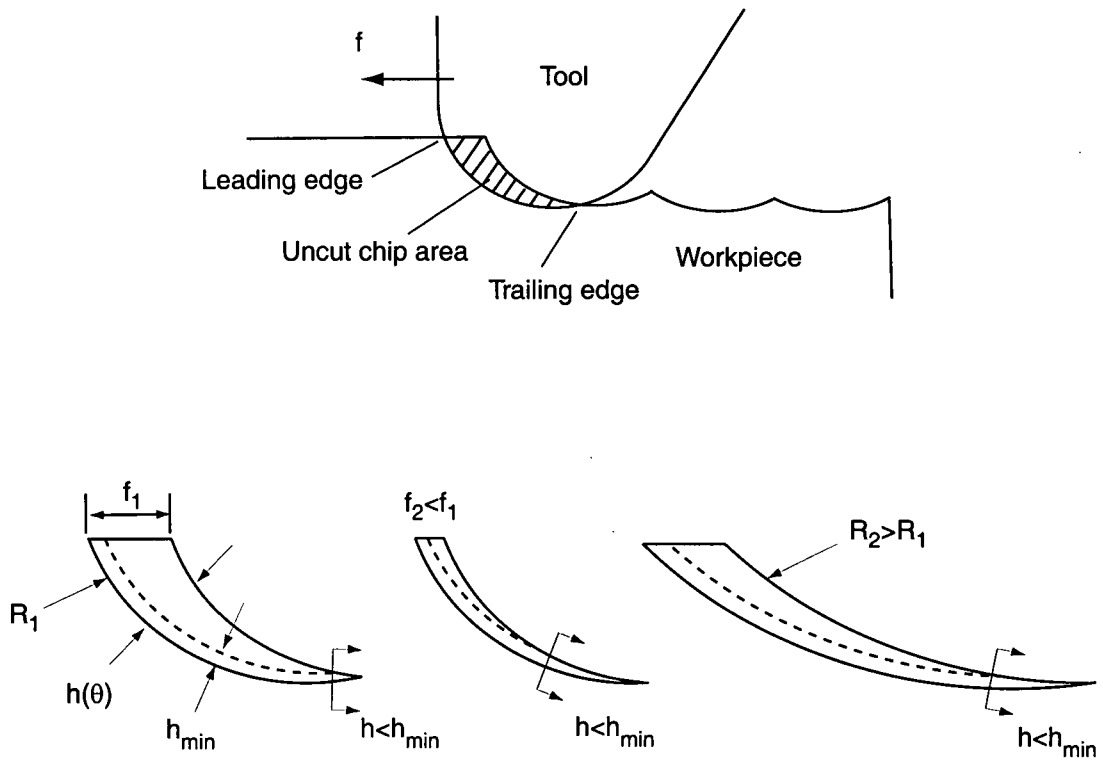

Figure 2.6 : Effect of feedrate and tool nose radius on the fraction of the uncut chip area in which $h < h_{min}$.

2.2.4. Hard turning

In precision hard turning the cutting tool material and geometry, the cutting conditions, the machine tool properties, and the surface integrity of the part must be considered to determine the achievable tolerances and functionality. Machining of hardened steels (hardness greater than 50 HRC) has been facilitated by the advent of new cutting tool materials such as Cubic Boron Nitride (CBN) and ceramics such as Al_2O_3/TiC. Compared with conventional carbide tool materials, they offer high hardness and temperature stability. This is necessary as thermal and mechanical loads in hard turning are higher than typically encountered with softer materials. The reduced level of tool wear using CBN is such that hardened cylindrical components (eg. gears, shafts) which were previously ground can be machined on a turning centre. To reduce loads on the cutting tool, a small depth of cut (within the nose radius) and low feed are required. At low depth of cut the radial cutting force is highest [3], [18] due to the effect of the tool nose radius and large negative rake angle, and increases dramatically over time with increasing flank wear [8].

Chip formation in hard turning is characterized by a segmented chip, rather than a continuous chip generated when softer metals are machined [3], [8], [21], [22], [23], [24]. The high material hardness combined with large negative rake angles cause large compressive forces in the shear zone which inhibit plastic deformation of the material. The compressive stresses are reduced near the free surface of the workpiece, enabling a shear crack to form. The crack propagates until the level of compressive stress is sufficiently high, at which point the remaining chip is sheared through plastic deformation. Thus a segmented chip consisting of undeformed segments held together by plastified material is formed. Due to the cyclic nature of the chip formation, the cutting tool experiences low amplitude, high frequency oscillations (greater than 10 kHz) in the cutting forces [8].

Many researchers have investigated microstructural changes in the surface of a part due to hard turning. The high temperatures generated by friction in the flank can cause the workpiece to be rapidly austenitized and then self-quenched forming a thin surface layer in which the micro-

structure is altered. This is commonly referred to as "white layer", as an etched layer appears white when viewed under an optical microscope. The white layer is characterized by increased levels of martensite due to rapid cooling. The structure of the white layer is well know to affect the residual stresses on the surface of the part, which may have an adverse effect on fatigue life. Since martensite has a lower specific volume than austenite, transformation to martensite causes tensile residual stresses to be superimposed on the compressive surface stresses achieved through mechanical compression in the machining process [3]. The heat generated in the flank region is a result of the cutting power in the flank, which can be expressed by $P_f = \mu_f \cdot \sqrt{F_r^2 + F_f^2} \cdot V_c$ [8], where μ is the coefficient of friction in the flank, F_r is the radial cutting force, F_f is the feed force, and V_c is the cutting speed. Clearly reduction of these values minimizes the generated heat in the flank region, and may reduce the appearance of white layer.

Thiele et al [25] determined that tool edge geometry showed a strong influence on white layer formation and residual stresses of hardened 52100 steel (60 HRC). It was observed that large honed cutting edges produced continuous white layers and deeper compressive stresses compared with sharp tools, and that white layer thickness correlated to residual stresses. Matsumoto et al [26] performed hard turning of bearing steel, and showed as well that deep compressive stresses could be achieved by applying large edge honing or increasing the effective rake angle, although no microstructural changes were observed. The effect of material composition was studied by Ramesh et al [27], who concluded that machining a 4340 steel (57 HRC) showed less white layer formation than 52100 steel of the same hardness, especially at low feedrates.

The fatigue life of hard turned specimens was investigated by Smith and Melkote [28], who determined that white layer formation showed no clear affect on axial fatigue life, and that variations in tool edge preparation affected the residual stress distribution. Ueda et al [29] measured the temperature in the flank of CBN tools in machining, and determined that the temperature in the flank is highly affected by cutting speed, reaching 950°C at 300 m/min, which exceeds the austenitizing temperature of many steel alloys. Chou and Evans [30] developed a thermal model

which predicted white layer formation, and concluded that the primary factor was flank wear land rubbing. As well Liu and Wang [31] developed a model to predict the effect of tool flank wear on heat transfer, thermal damage, and cutting mechanics in hard turning.

2.3. Piezoelectric tool actuator development

Piezoelectric translators are widely used as driving elements in tool positioning systems, converting electrical energy into mechanical deformation. They have several features which are advantageous in metal cutting applications, namely high stiffness, high force generation, unlimited positioning resolution, and no stick slip or friction. The main disadvantages of piezoelectric translators are limited stroke, heat generation in dynamic applications, and risk of brittle fracture due to tensile or shear stresses. The most common piezoceramic material is lead-zirconate-titanate (PZT). After poling by an electric field, raw PZT crystals exhibit tetragonal symmetry, an anisotropic structure. Electric dipoles, formed due to charge separation between positive and negative ions, align during poling. After poling the dipoles stay roughly aligned, causing a remanent polarization. When an electric field is applied to a poled piezoceramic material the dipoles increase their alignment proportional to the voltage, and the crystal grows in the direction aligned with the field and contracts along the axes normal to the field. Although the deformation is small, when several PZT disks are mounted in series (known as a stack actuator) the resulting displacement is significant.

Many authors have investigated the use of piezoelectric actuators for use as fast tool servos for machine tools. Using a fast tool servo attached to a standard lathe turret, Zhu et al [32] developed a sliding mode control scheme and investigated the effect of cutting conditions on surface finish quality. The fast tool servo, designed by Schumacher [33], was comprised of a PZT translator housed within parallel flexures onto which the toolholder was mounted. A laser sensor provided the position feedback signal. The actuator had a radial stiffness of 37 N/micron, natural

frequency of 600 Hz, maximum stroke of 60 micron, and a positioning resolution of 0.2 micron. Jun [13] showed that grinding quality surface finish was achievable by precision turning with the actuator at a 5 micron depth of cut.

In order to increase the stroke of piezoelectric positioning systems, some authors have developed novel approaches. Bracht [34] designed an inchworm type actuator, whereby one PZT stack provides the tool motion, and eight PZT stacks mounted transverse to the driver stack clamp and unclamped either side of the actuator. The maximum stroke was 300 micron. The system was to operate in one of two modes; position control or clamped. The stiffness of the design was 1142 N/micron in the clamped mode. A two-stage system incorporating a voice coil motor for coarse motion and a PZT actuator for fine motion was developed by Sugita et al [35]. The system was designed for turning of aluminum pistons, and the authors achieved +/- 2 micron accuracy. The static stiffness of the system was 64 N/micron. Pahk et al [36] used a ball screw drive combined with a piezoelectric actuator for coarse and fine positioning of the tool tip. The total stroke was 200 mm with an positioning accuracy of 10 nm. The control scheme used was proportional-integral-derivative (PID) with a digital filter. The design of linear piezomotors was studied by Zhu and Zhang [37]. The design requirements for machine tool applications were given as high resolution, high stiffness, high output force, adequate compactness, and a monolithic flexure frame. The actuator developed used a driving piezostack element, and two clamping piezostack elements to produce inchworm-like motion. The achieved positioning resolution was 5 nm with a travel range of 11 micron for a single step. Although the positioning resolution is high, it is unknown how the piezomotor would perform in a machining operation as no cutting tests were performed.

Many authors have investigated the use of piezoelectric tool actuators for diamond turning applications. Diamond turning involves the machining of high precision components, such as optics and integrated circuit manufacturing, performed on high precision lathes which require special environments for thermal stability and vibration isolation. Although the tool actuator presented in this thesis is intended for conventional turning centres, a review of tool actuators for

diamond turning is useful nonetheless. Cuttino et al [38] used a fast tool servo with a piezoelectric actuator housed in annular flexures to machine non-axisymmetric parts in single point diamond turning. The system had 0.025 micron resolution, 70 N/micron stiffness, 100 micron range, and a natural frequency of 250 Hz. The accuracy of the tool during machining was 0.6 micron. Kim and Kim [10] used a piezoelectric actuator to control the depth of cut as well as to compensate waviness during machining. The system was mounted to a precision lathe with aerostatic bearings and granite bed in a thermostatic room. A proportional-integral (PI) controller was used with piezoelectric voltage feedback to reduce surface waviness from 1.3 microns to 0.7 microns.

Rasmussen et al [39] used a piezoelectric tool actuator to compensate dynamic errors during machining, such as non-uniform workpiece deformation, spindle motion error, and vibration. A repetitive control strategy was employed to generate non-circular aluminum workpieces, with 21 micron variation in the depth of cut. The peak to peak surface errors were 5 micron. The actuator had a static stiffness of 19.25 N/micron, 52 microns of travel, and a natural frequency of 1000 Hz. A strain gage was used for position feedback. A micro-cutting device using a piezolectric actuator housed within parallel springs was developed by Hara et al [40] for use with a diamond tool on an ultra-precision lathe. The mechanical properties were natural frequency of 4.8 KHz and 80 N/micron stiffness, the control resolution was 5 nm. In machining of an Ni-P plated steel disk the effective depth of cut measured on the part agreed with the actuator command within +/- 0.1 micron for a commanded depth of cut range of 0.05 to 1 micron. Shamoto and Moriwaki [41] used piezoelectric actuators for elliptical vibration diamond cutting of hardened steel, whereby the tool is elliptically vibrated in the tangential direction to reduce frictional forces on the rake face. Piezoelectric strips located on a circular bar were excited with a phase shift to achieve elliptical motion of the tool.

Okazaki [42] achieved positioning resolution of 25 nm for a piezoelectric actuator design for diamond turning machines. The static stiffness of the actuator was 2 N/micron, and a state feedback with state observer controller was implemented. Kim and Nam [43] investigated controller

design of a piezoelectric actuator for a ultra-precision turning. They concluded a piezoelectric voltage feedback was faster and more stable compared with displacement feedback control, although the achieved settling time was only 0.15 seconds, and the displacement resolution of 0.5 micron is large for a precision process. Hanson and Tsao [44] developed a fast tool servo using a piezoelectric actuator for variable depth of cut boring. A repetitive control scheme was used to compensate periodic disturbances due to spindle eccentricity and fixturing, and a proportional-integral (PI) controller was added to handle random disturbances. In turning of aluminum shafts tracking error of less than 2.05 microns were achieved.

2.4. Design of micropositioning systems

An overview of the principles of precision design of micropositioning systems was presented by Schellekens et al [45]. The main elements to be considered for precision design are component geometry, kinematics, and dynamics. Limitations in manufacturing cause part geometries to deviate from the ideal, causing macroscopic (straightness, roundness, flatness) and microscopic errors such as surface roughness. The surface finish of mating components, even under clamping loads, can affect the overall stiffness, damping, hysteresis, and thermal conductivity of the structure as a whole. Kinematic factors such as actuator response, feedback resolution, control strategy, and mechanical repeatability can limit the accuracy of the system. The dynamics of the structure must be considered to minimize inertial loads. For rotational motions unbalanced forces must be minimized by ensuring symmetry, and keeping the mass of moving components low reduces inertial loads for translational motions. In addition, motion trajectories should be commanded such that discontinuities in the acceleration and jerk profiles are minimized to ensure smooth motion and reduce the risk of exciting the modes of the structure.

For design the generalized Abbe principle is commonly applied, and stated below. This principle can be applied to positioning systems as well to ensure the commanded position is reflected in the application.

A displacement measuring system should be in line with the functional point whose displacement is to be measured. If this is not possible, either the slideways that transfer the displacement must be free of angular motion, or angular motion data must be used to calculate the consequences of the Abbe offset.

Micropositioning systems requiring small precise movements often use solid flexure hinges over rigid body joints in the translation mechanism. Solid flexures are well known to provide motion free of rolling or sliding friction, zero backlash, and do not require lubrication [45], [46], [47], [48]. Typically any material non-linearity can be neglected as it is insignificantly low compared with motion range [45]. Flexure mechanisms can be designed for as many degrees of freedom (DOF) as required by the application. In this study only linear single DOF mechanisms are considered. The limited stroke of piezoelectric actuators is such that flexure mechanisms are often designed to provide amplification of the input displacement, which is accomplished through appropriate selection of the geometry of the structure. In general an increase in displacement amplification causes a decrease in stiffness [34], [49] at the location of the output displacement.

Figure 2.7 presents examples of flexure mechanisms which transmit linear motion. The output displacement x results from the input force F. The parallel flexure in (a) is based on the four bar linkage. The output motion is linear, yet there is a parasitic motion error in the transverse direction [50]. The displacement amplification is simply the ratio $\frac{x}{y} = \frac{L_1}{L_2}$ where y is the input displacement. The parasitic motion can be compensated for using the compound parallel flexure design in (b) [48], [50], which adds an additional four bar linkage mechanism. In (c) linear motion is achieved, although in this case the hinges must be strained in the axial direction to per-

mit motion. Although the achieved amplification can be very high, the non-linear nature of the input-output relationship is a problem for control. The displacement amplification of the double compound flexure in (e) is given by $\frac{x}{y} = \frac{L_2 L_4}{L_1 L_3}$ [52]. Furukawa et al [51] presented the non-linear displacement amplification of the mechanism (d) by the equation given below.

$$\frac{x}{y} = \frac{L_1}{L_2}\left[1 + \left(1 + \frac{L_1^2}{L_2^2}\right) \cdot \frac{y}{4L_1} + \left(1 + \frac{L_1^2}{L_2^2}\right) \cdot \frac{y^2}{8L_1^2} + \ldots\right]$$

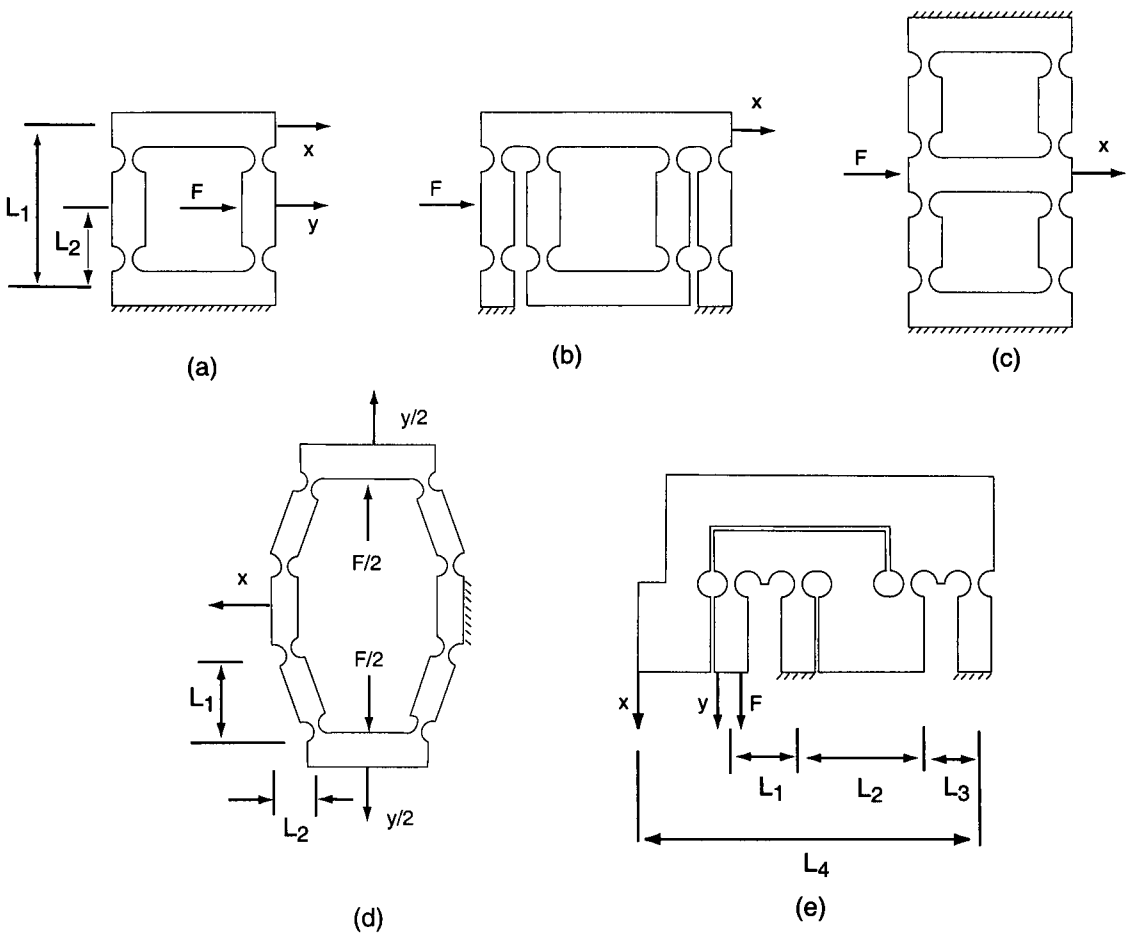

Figure 2.7 : Examples of solid flexure mechanisms transmitting linear motion.

The hinge profile plays in important in the mechanical properties of the flexure. Figure 2.8 presents single hinge types. The circular hinge offers lowest stress and highest stiffness, whereas the right angle hinge has low stiffness but high stress concentrations in the corners of the hinge. The elliptical and corner-filleted profiles may provide an adequate compromise depending on the application according to Xu and King [49], who compared the properties of each profile using finite element (FE) analysis. It was determined that the elliptical hinge profile is most suitable for high displacement mechanisms due to higher flexibility and longer fatigue life compared with square filleted hinges for similar displacements. A low profile stage for precision joining was designed by Yang and Jouaneh [53], which featured the use of a half-notch hinge, shown in Figure 2.8, which has half the compliance of a single notch hinge. Ultimately the optimum hinge design depends on the requirements of the structure, and a trade off exists between stress and stiffness. As well as stiffness in the direction of motion decreases, a proportional decrease in stiffness in the directions perpendicular to the motion may be undesirable.

Machining errors in the hinge profile can cause the output displacement to deviate from the desired value. Xu and Qu [48] presented analytical relations for the effect of machining errors on positioning accuracy of a micropositioning stage. Ryu and Gweon [50] studied the effects of tolerances on hinge width, drilled hole radius and centre location, as well as the perpendicularity of drilled holes. It was concluded that machining imperfections have serious influences on both in plane and out of plane parasitic motions. Considering shape changes and residual stresses caused by the machining process, wire Electrical Discharge Machining (EDM) is often used to obtain an accurate hinge profile [42]. Xiaowei et at [47] proposed a combined electrical machining process for the production of flexure hinges. Pulse electrochemical machining (PECM) of the hinge profile following the EDM was performed to remove thermally affected zones and improve surface finish.

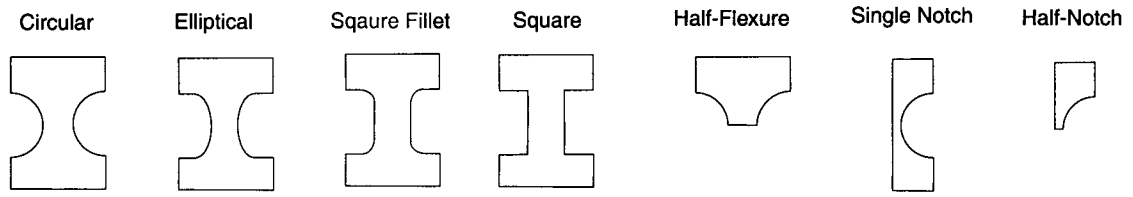

Figure 2.8 : Solid flexure hinge profiles.

Paros and Weisbord [54] investigated the design of solid circular hinges, as shown in Figure 2.9. Equations 2.2 and 2.3 were developed for bending stiffness, K_B, and axial stiffness, K_S, based on hinge thickness (t), radius (r), width (b), and modulus of elasticity (E). It is assumed that deformation is concentrated entirely within the web, and that the remaining part of the hinge is rigid, and that under load only bending and axial deformation exist. As well it is assumed that the centre of the hinge remains fixed, while in practice the hinge centre may change with deformation [46], affecting the accuracy of the output displacement. A linear scheme was proposed by Her and Chang [46] for displacement analysis of micropositioning stages. Each flexure hinge of the mechanism is treated as rigid body hinge plus a torsional spring, axial extensions are not considered, and bending stiffness is assumed to be constant over the motion range. Through finite element simulation they showed bending stiffness is not constant, and shows a linear decrease with increasing angular displacement. For displacement angles within +/- 1 degree the bending stiffness varied only 1.5 %, thus it can be considered constant for small displacements. For large hinge radius to thickness ratios, the FE simulation of hinge bending stiffness deviated from Equation 2.2.

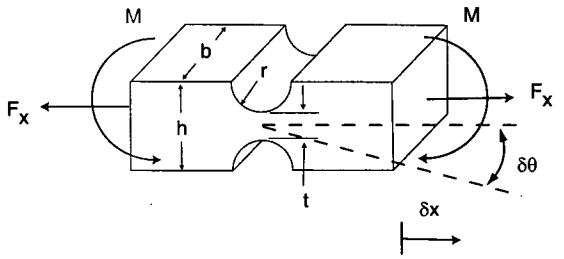

Figure 2.9 : Circular solid flexure hinge geometry.

$$K_B = \frac{M}{\delta\theta} = \frac{2Ebt^{5/2}}{9\pi r^{1/2}} \tag{2.2}$$

$$K_S = \frac{F_x}{\delta x} = \frac{Eb}{\pi(r/t)^{1/2} - 2.57} \tag{2.3}$$

Chapter 3

Actuator Design and Analysis

3.1. Introduction

This chapter presents the precision turning actuator, with focus on the system operation, component design, and structural analysis. The objectives of the design, as well as the constraints to be satisfied are discussed and related to the precision turning process. The overall design of the system is presented, followed by the detailed component structural design and analysis. The major components discussed are the piezeoelectric driving element, the Guiding Unit which transmits motion to the tool via solid flexures, the feedback sensor assembly, the Clamping Unit assembly, and the tool assembly. The analysis is focused primarily on the main structural component of the actuator, the Guiding Unit. An analytical model is developed for preliminary selection of flexure hinge geometry, which is then optimized for stiffness using a finite element (FE) model. Using the determined properties of the flexure hinges, the maximum inertial load is predicted and used to set the required preload on the piezoelectric translator. Given the preload, stiffness, and stroke, the maximum load on the Guiding Unit is calculated and input into the FE model to predict the maximum stresses. The stresses are then compared with the material properties of the structure. The dominant natural modes of the flexure hinge, rear support plate, and sensor bracket are determined as well through finite element analysis.

3.2. Design objectives and constraints

The purpose of the tool actuator is to allow for precision turning on conventional lathes such that the grinding operation, generally required for high tolerances on cylindrical parts, can be

eliminated. The design must satisfy constraints on tool positioning, the design envelope, the mechanical properties, and system operation. For a tolerance of less than one micron on a diameter, the variance in depth of cut can be maximum 0.5 microns, thus this is the maximum allowable positioning resolution of the actuator. The total stroke must be large enough to reduce the number of finishing passes, and greater than the accuracy of a conventional feed drive, thus a value of 35 microns is chosen. In order for the system be usable in an industrial setting the actuator must be compact and self-contained, and be able to interface to any standard lathe with minimal interference with other tools in the turret. Ideally the design should be symmetric to avoid moments within the structure. Depending on the process (turning, grooving, facing, etc.), different types of toolholders may be required, and the actuator must allow for easy exchange of standard toolholders. The tool tip must align with the radial axis, such that a commanded actuator displacement is directly reflected as a change in depth of cut during the turning process. To reduce static deflection the actuator should have high mechanical stiffness in all directions, as well the natural frequency must be sufficiently high such that the cutting forces do not excite the modes of the system.

The radial component of the cutting forces in finish hard turning can reach as high as 500 N [8], thus the minimum design stiffness in the radial direction is 200N/micron to allow a 2.5 micron reduction in depth of cut (5 microns on diameter) under maximum load. The minimum natural frequency of any mode of the structure is 1000 Hz, such that only the workpiece, machine tool spindle or feed drive dynamics are excited at lower frequencies. In addition the actuator must provide the capability to rigidly lock the tool once positioned, which is desirable for roughing operations in which the depth of cut is large and the cutting forces are highest. In this case the radial stiffness should be double that of the unclamped operation. Finally there must be the option to measure the radial cutting force, which provides insight to the cutting process (eg. tool forces, spindle eccentricity) and a measure of the disturbance seen by the actuator controller. The design constraints are summarized in Table 3.1.

Item	Constraint
Stroke	> 35 micron
Positioning resolution	< 0.5 micron
Max. x dim	100 mm
Max. y dim	150 mm
Max. z dim	100 mm
Turret Interface	Compatible with standard turret
Radial Stiffness	> 200 N/micron (unclamped) > 400 N/micron (clamped)
Natural Frequency	> 1000 Hz (any mode)
Operation modes	Position control or rigidly clamped
Tool Adapter	Accept standard exchangeable toolholders
Force Measurement	In radial direction only
General design	Compact and self-contained Symmetric about y and z axes Tool tip aligned with radial axis

Table 3.1 : Actuator design constraints.

3.3. Design overview

A solid model of the precision turning actuator, mounted to the Hardinge Superslant lathe turret in the Manufacturing Automation Laboratory at UBC, is presented in Figure 3.1. The actuator turret interface is clamped to a toolholder slot using a 19.04 mm x 19.04 mm cross section wedge set. The feed drive of the CNC turning machine provides feed motions in the radial (x) and feed (z) directions, and the actuator provides fine tool positioning in the radial direction relative to the stationary actuator housing. The overall actuator dimensions are given in Figure 3.5. The actuator envelope is 95.5 mm in the radial direction, 143 mm in the tangential direction, and 85 mm in the feed direction, all of which satisfy the design constraints. The tool stick-out is 67 mm in the radial direction, and 20 mm in the feed direction. The actuator is symmetric about the y and z axes, and the tool tip is aligned with the x-axis. Mounted to the Hardinge turret the actuator

occupies one toolholder slot, and interferes with the two adjacent slots. Despite this the actuator is considered to be compact as industrial turning machines have considerably larger turrets and toolholder slots such that interference with other tools is minimal.

The external and internal components are presented in Figures 3.2 and 3.3, respectively. A piezoelectric stack actuator is housed under preload within the Guiding Unit, as shown in Figure 3.4. With an applied voltage the piezostack expands and contracts along the radial (x) direction. An alignment washer locates the piezostack to the centre of the assembly. The Guiding Unit is a monolithic structure which transmits motion from the piezoelectric translator to the tool assembly. Four solid flexures, each with two circular solid hinges, deform due to the load applied by the piezostack. Due to the symmetric arrangement of the flexures the deformation is linear without parasitic error, and motion is directly transmitted to the tool assembly. The Tool Adapter contains a Komet ABS N25 clamping system, which allows for the use of exhangeable Komet toolholders depending on the turning application (eg. longitudinal turning, grooving, facing, etc.). The Tool Adapter is aligned to the Guiding Unit via two alignment dowels and fastened using four M4 bolts.

The Guiding Unit is enclosed and supported by the Top and Bottom Plates. A capacitive position sensor is used to measure the relative displacement of the Guiding Unit flexures. The sensor consists of a stationary probe fastened to the fixed Top Plate, and a moving target fastened to the moving section of the Guiding Unit. Two Clamping Units, each containing a piezoelectric stack actuator, serve to rigidly clamp the moving section (see Figure 3.4) if necessary for roughing operations to prevent machine tool chatter. For machining operations involving cutting fluids the actuator must be sealed to prevent leakage into the assembly. Acrylic covers are used to protect the position sensor as well as the gap between the Guiding Unit flexures and the Top and Bottom plates, as shown in Figure 3.6. A silicone sealant is required along the cover edges and all interfaces, including metal-metal contact zones.

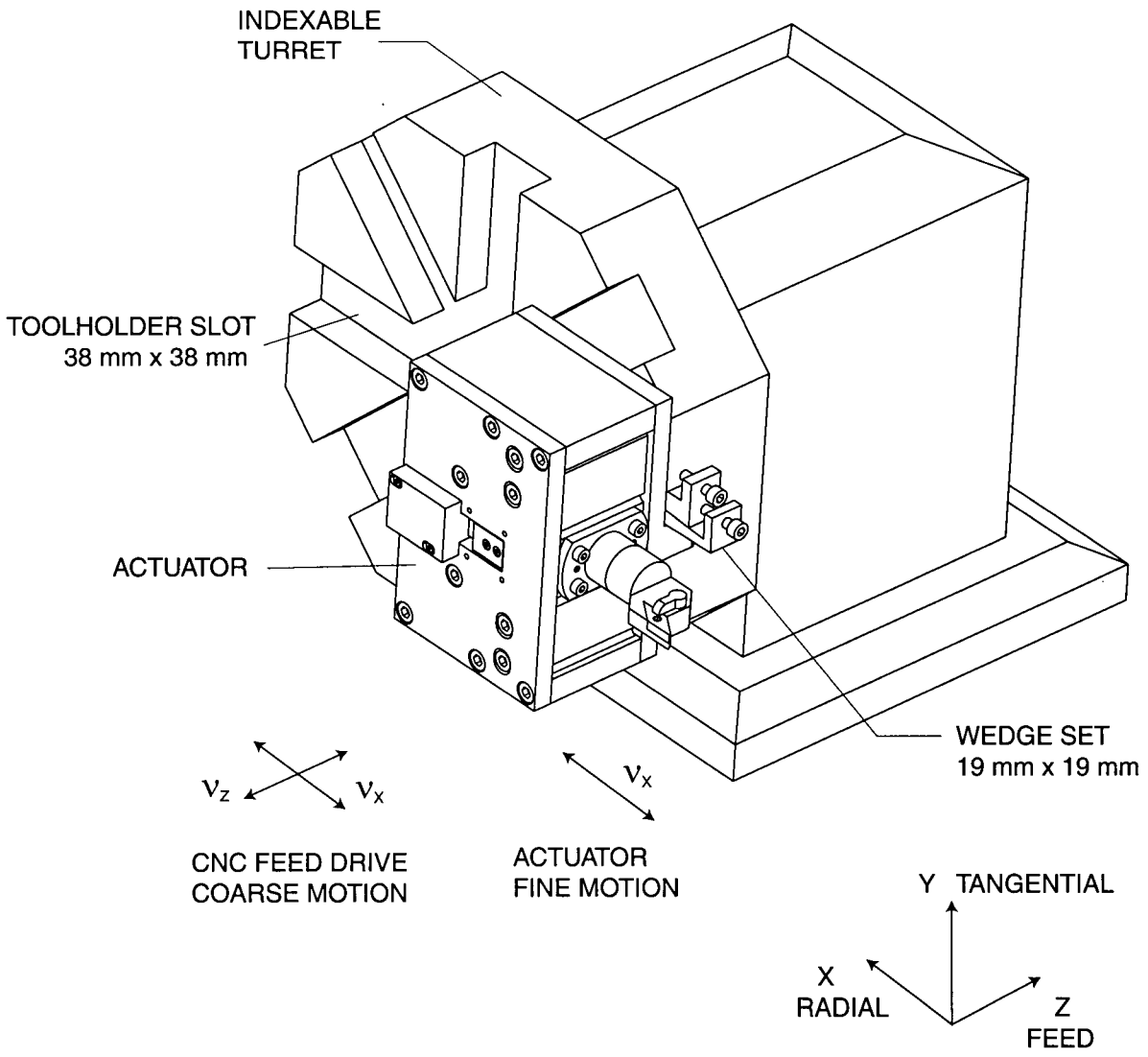

Figure 3.1 : Actuator mounted to a Hardinge lathe turret.

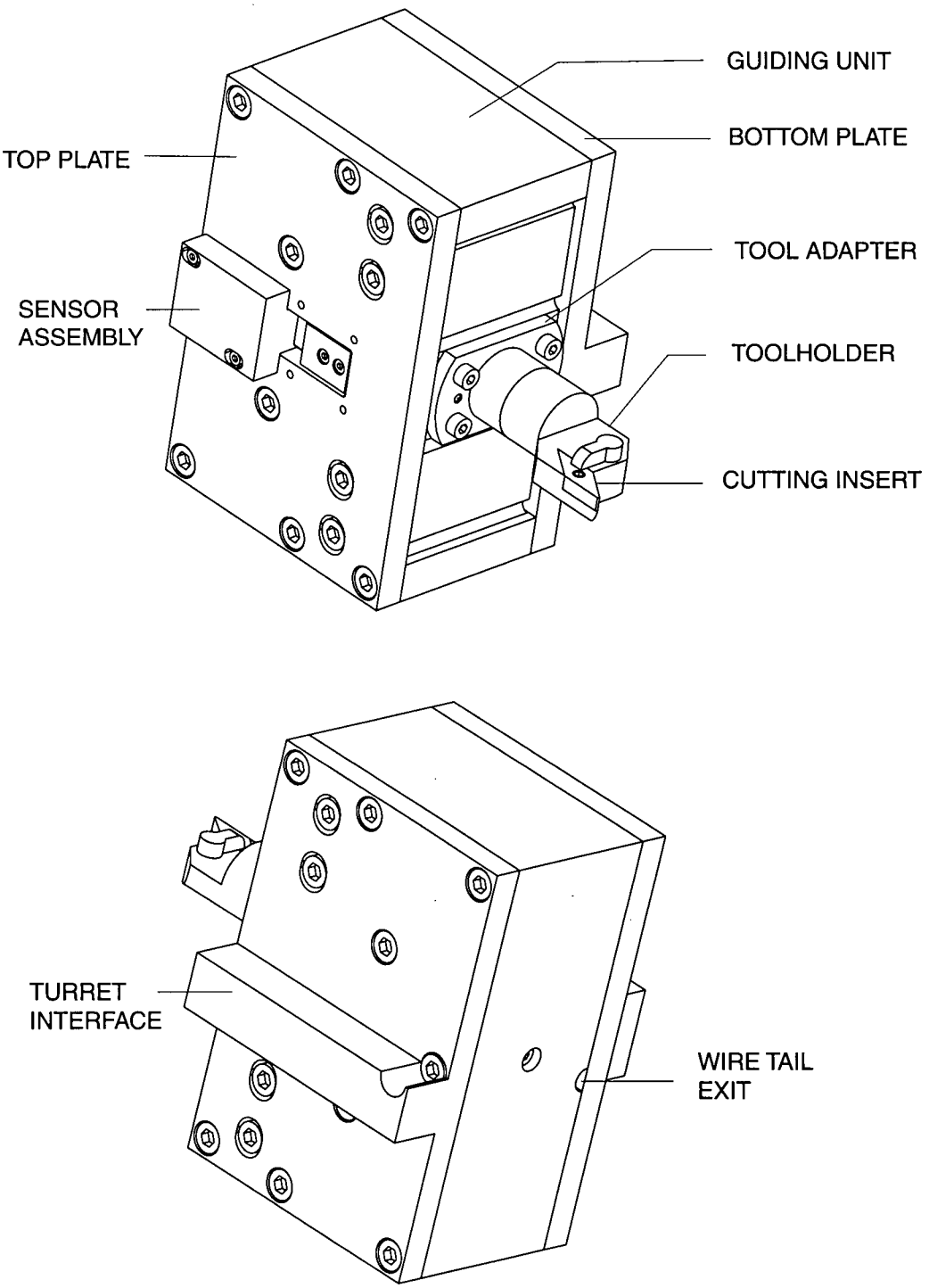

Figure 3.2 : Actuator external views and major components.

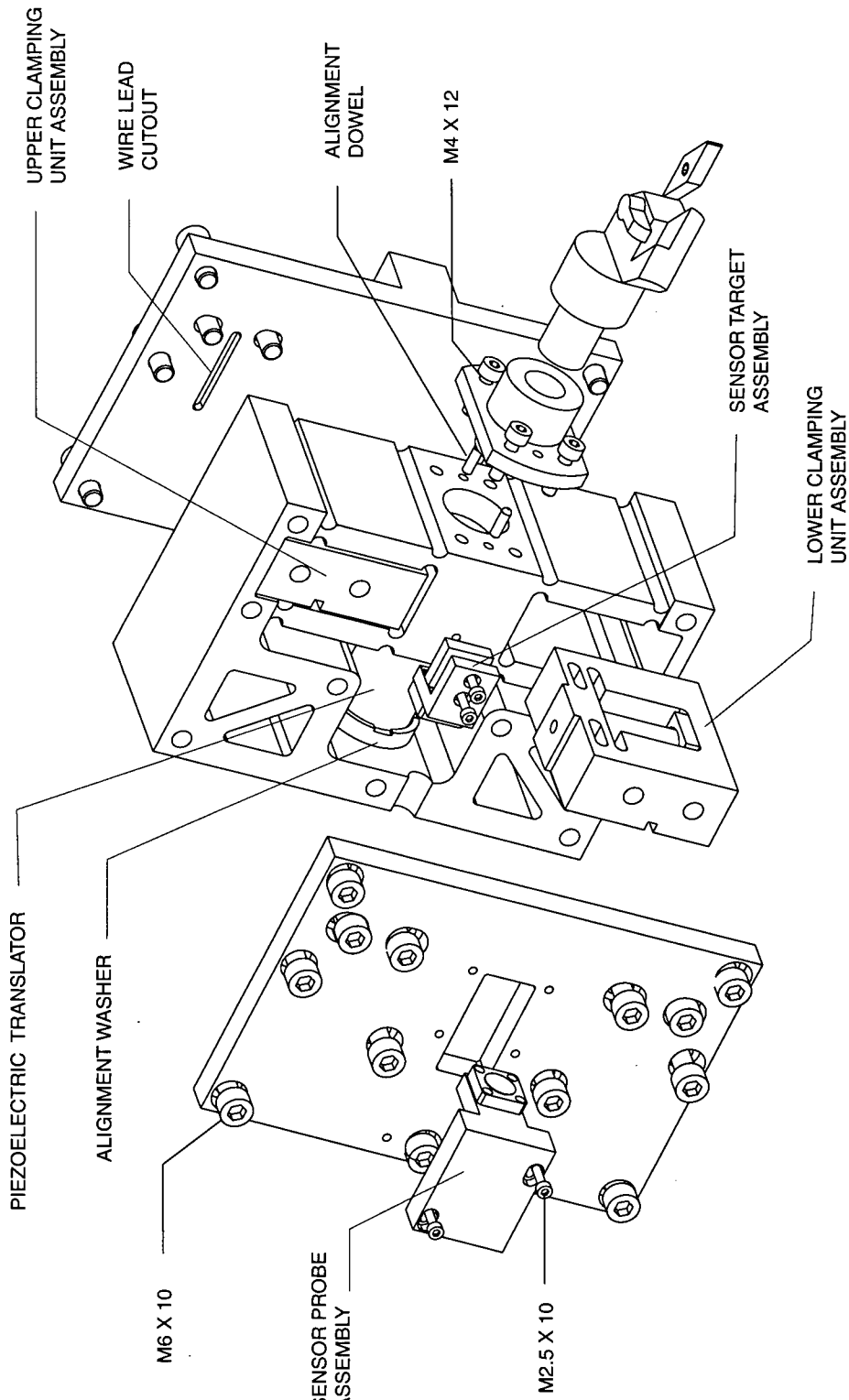

Figure 3.3 : Exploded view of the actuator assembly.

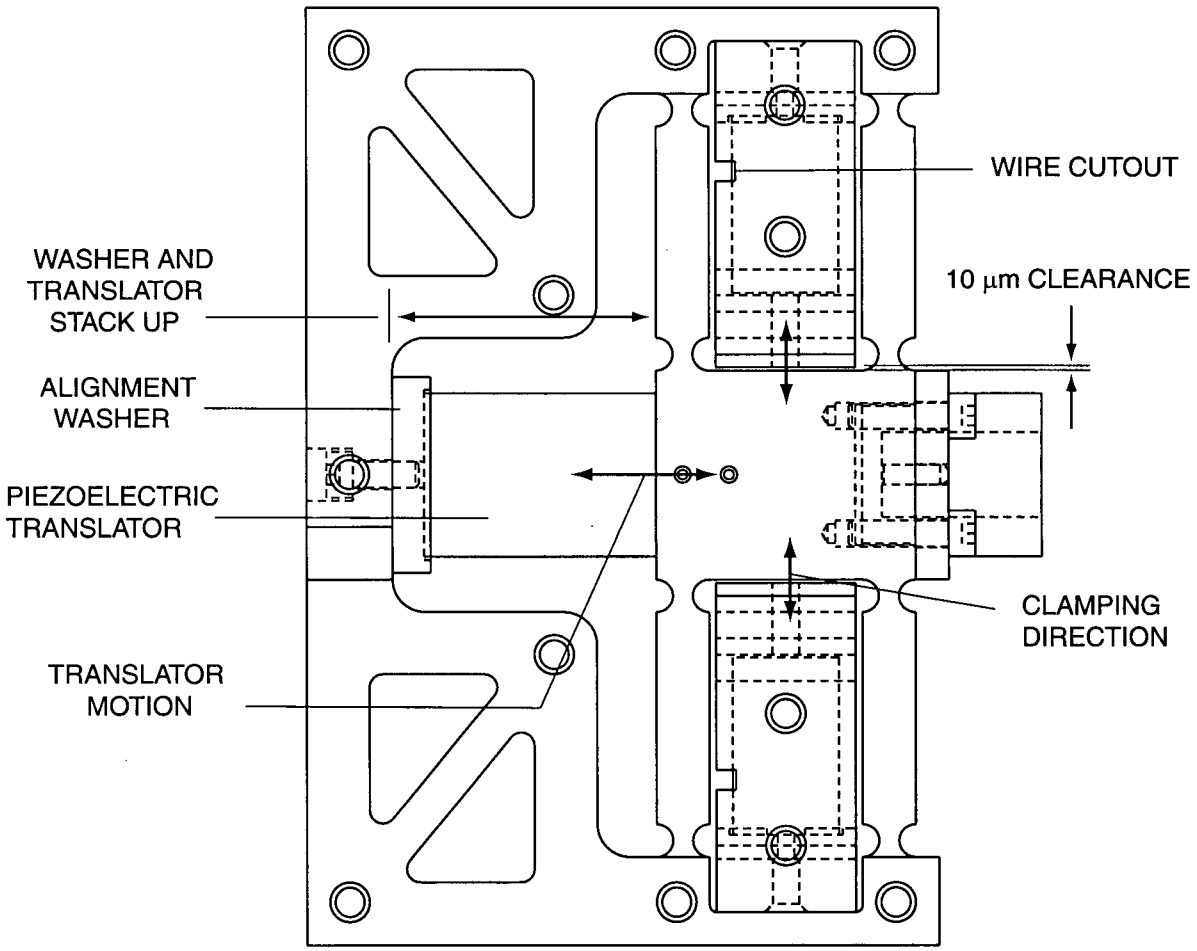

Figure 3.4 : Internal view of actuator with support plates removed.

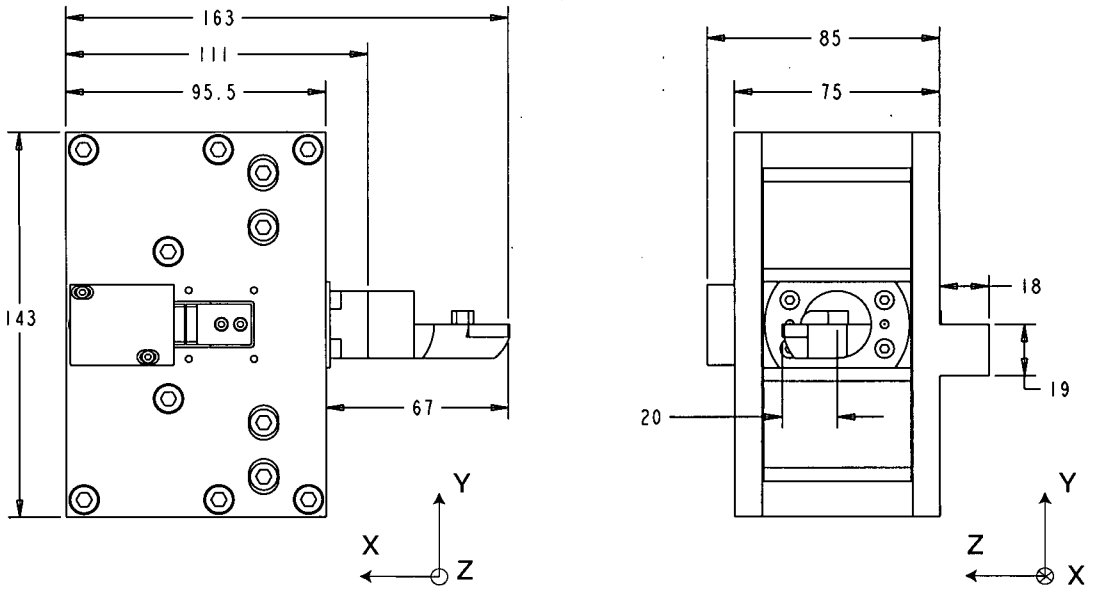

Figure 3.5 : Actuator overall dimensions (in mm).

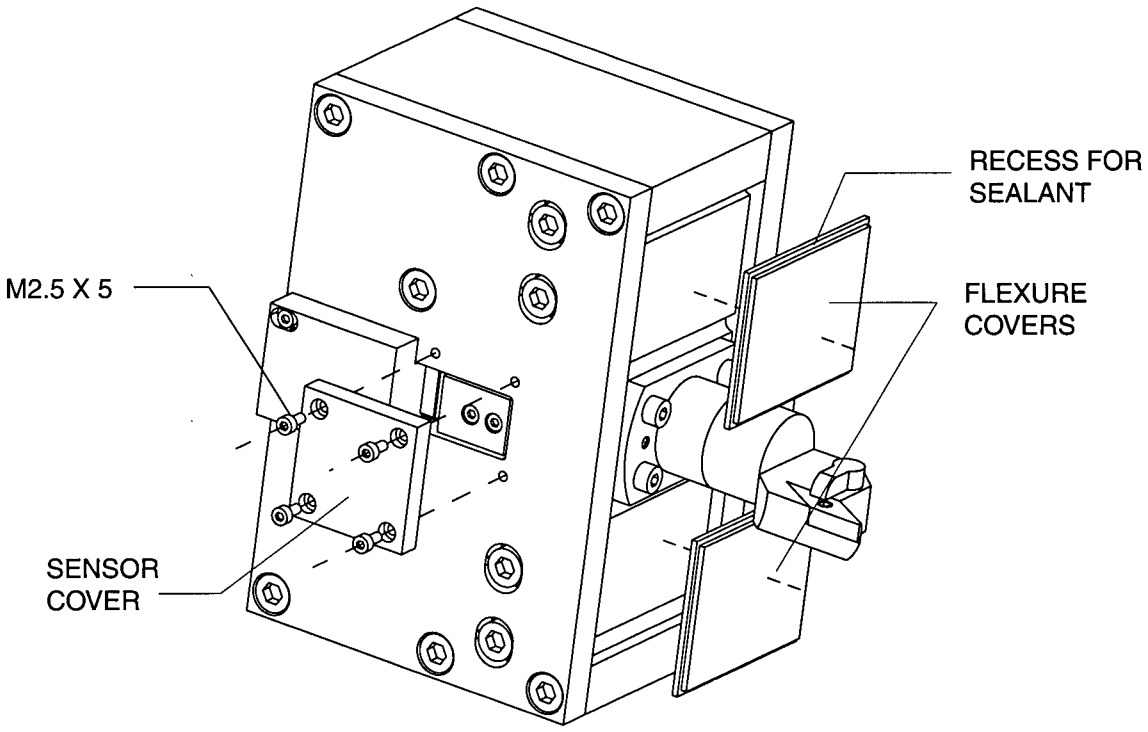

Figure 3.6 : Actuator covers for use with cutting fluids.

3.4. Precision turning process

The precision turning operation using the actuator for longitudinal shaft turning is outlined in Figure 3.7. Roughing operations at large depths of cut and feed rates are performed with conventional tooling and CNC control (Step 1). Following roughing, the actuator is used to perform semi-finish turning, whereby the lathe CNC executes both radial (x) and feed (z) motions with the actuator tool position, x_a, controlled to a zero reference position (Step 2). Typically the depth of cut in finishing is 0.1 mm to 0.4 mm. After each pass the operator must measure the diameter of the workpiece and compare it to the specified design value. When the dimension is within the effective stroke of the actuator (25-30 microns) the radial position of the CNC is fixed, and the actuator tool position is retracted a small amount ($-10 \le x_a \le -5$ micron) to clear the workpiece (Step 3). The feed motion of the CNC positions the tool at the beginning of the cut, and the final precision depth x_a is commanded to the actuator based on the measurement of the shaft diameter. With the CNC depth still unchanged, the feed motion is executed for the finish cut (Step 4). By fixing the CNC motion the effects of the feed drive assembly backlash and friction are eliminated, and tool positioning in the radial direction is entirely relative to the actuator reference position set in the previous pass. The final step is repeated until the required diametrical tolerance is met, which may take several passes due to static deflection and thermal expansion of both the machine and workpiece. In a conventional shaft turning process Step 4 is performed on a grinding machine to achieve the dimensional accuracy, which requires a change of machine tool and workpiece setup. For finish and precision machining operations the actuator is under position control using the feedback from the capacitive position sensor. The details of the instrumentation and controller design are described in Chapter 4. The actuator may be operated in open loop mode for roughing operations where small deviations in depth of cut are of little importance. With Clamping Units activated the actuator should be operated in open loop mode, as motion of the clamped Guiding Unit can damage the Clamping Unit piezostacks.

1. ROUGH TURNING

- STANDARD TOOL
- FEED AND DEPTH SET BY CNC

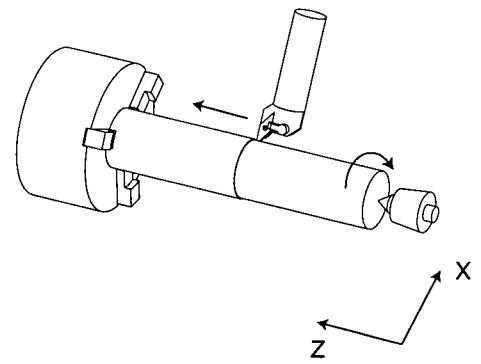

2. FINISH TURNING - ACTUATOR

- FEED AND DEPTH SET BY CNC
- ACTUATOR CONTROLLED TO ZERO POSITION

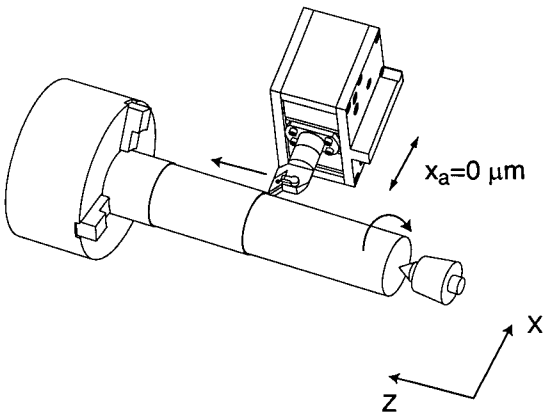

3. FIX CNC X-AXIS

- RETRACT ACTUATOR TO CLEAR WORKPIECE
- RETURN TO START OF CUT USING CNC Z-AXIS MOTION

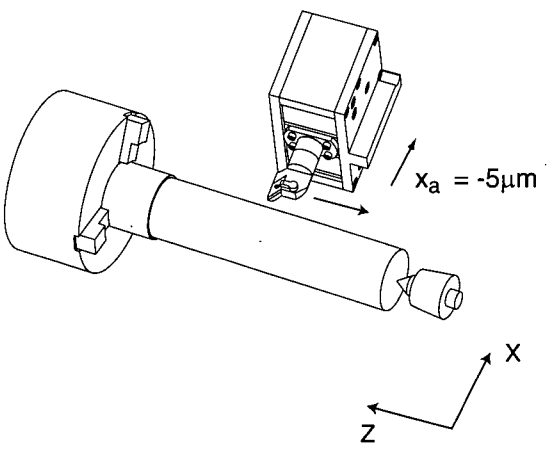

4. PRECISION TURNING

- SET DEPTH WITH ACTUATOR ONLY
- CNC CONTROLS FEED MOTION IN Z-DIR

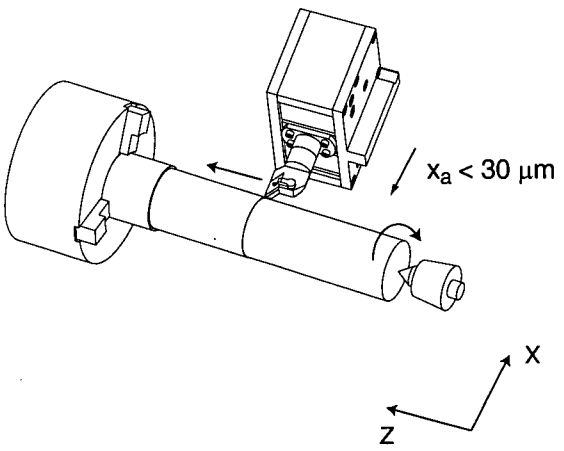

Figure 3.7 : Steps in the actuator assisted precision turning operation.

3.5. Component design and analysis

3.5.1. Tool assembly

The tool assembly is presented in Figure 3.8. In order to satisfy the requirement for exchangeable toolholders, a clamping system, ABS N25 offered by Komet USA, is embedded in the Tool Adapter. The male connection on the tool contains a floating pin, which mates with the receiving screw on the female connection of the adapter as shown in Figure 3.9. The connection is fastened by tightening the thrust screw on the female connection. The tool is aligned in the y and z directions, relative to the adapter, via two orientation pins which form a clearance fit with keyways on the adapter. The clamping system allows for any Komet ABS N25 toolholder to be used. The flange design of the steel Tool Adapter reduces the tool stick out in the radial direction compared with standard cylindrical adapters. To minimize the shear stress in the flange the rear diameter of the adapter is designed to be less than the tool diameter. In this way the radial load is transmitted directly to the Guiding Unit body without generating shear stress in the flange. The Tool Adapter is aligned in the y-z plane using two steel alignment dowels, and four M4 bolts fasten the adapter to the Guiding Unit.

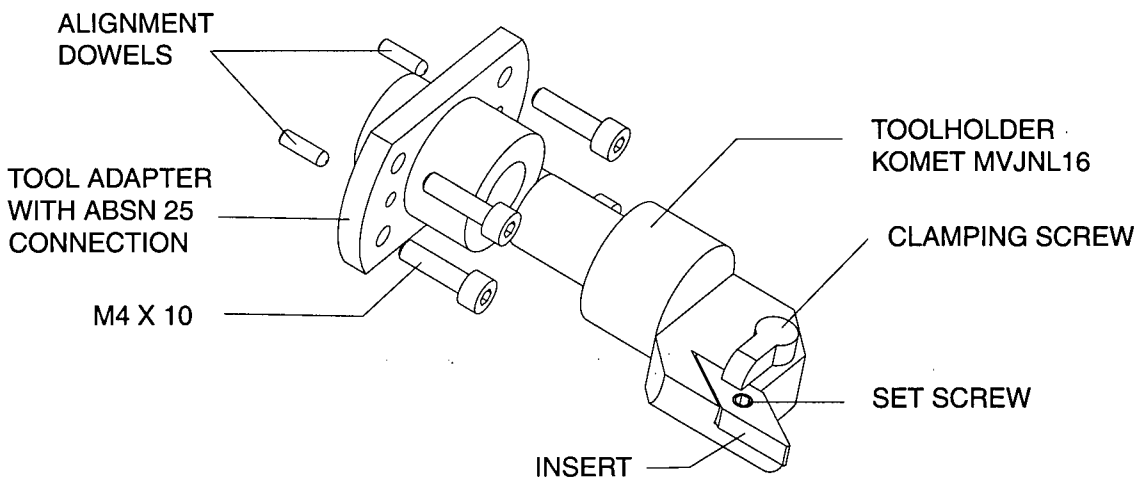

Figure 3.8 : Actuator tool assembly.

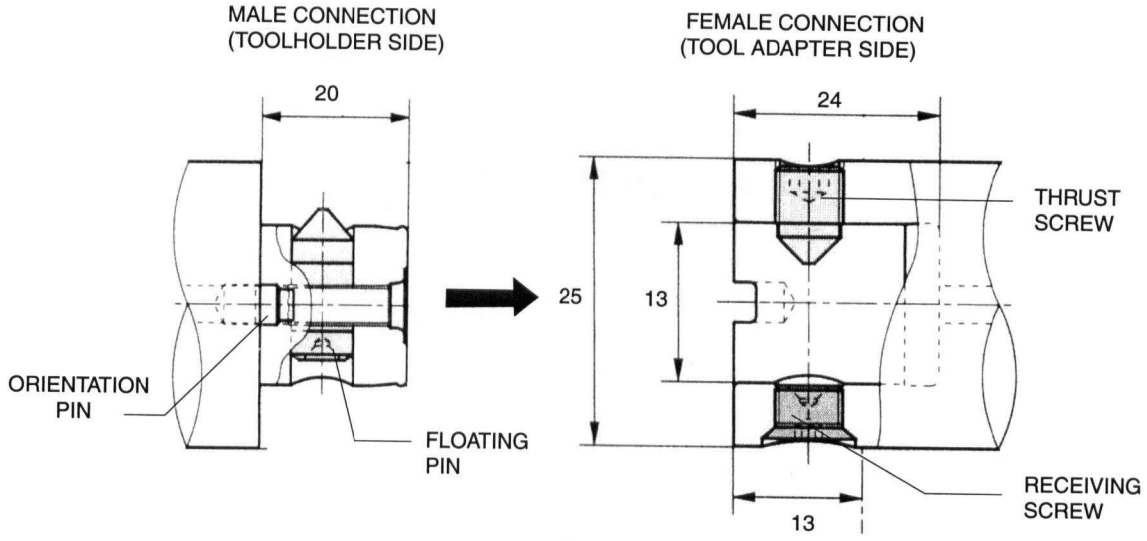

Figure 3.9 : Komet ABSN25 clamping system (dimensions in mm).

For the measurement of radial cutting forces, two single axis load cells can be mounted between the Tool Adapter and Guiding Unit through the mounting bolts, as shown in Figure 3.10. For increased rigidity two washers, surface ground to the thickness of the load cells, are mounted on the two remaining bolts. The specifications of the load cells are given in Table 3.2. By placing each load cell on opposite sides of the y and z axes the radial cutting force can be determined regardless of the resultant moments on the Tool Adapter due to cutting forces in all three directions. The cutting forces F_t, F_f, and F_r are transmitted to the Tool Adapter, and cause moments M_t, M_f, and M_r on the flange. The resulting force seen by the force sensors are FS_1 and FS_2,

$$FS_1 = \frac{F_r}{4} - \frac{M_r}{4L_1} - \frac{M_f}{4L_1} - \frac{M_t}{4L_2}$$

$$FS_2 = \frac{F_r}{4} + \frac{M_r}{4L_1} + \frac{M_f}{4L_1} + \frac{M_t}{4L_2}$$

where L_1 and L_2 are shown in Figure 3.10. The radial force is given by Equation 3.1.

$$F_r = 2 \times (FS_1 + FS_2) \tag{3.1}$$

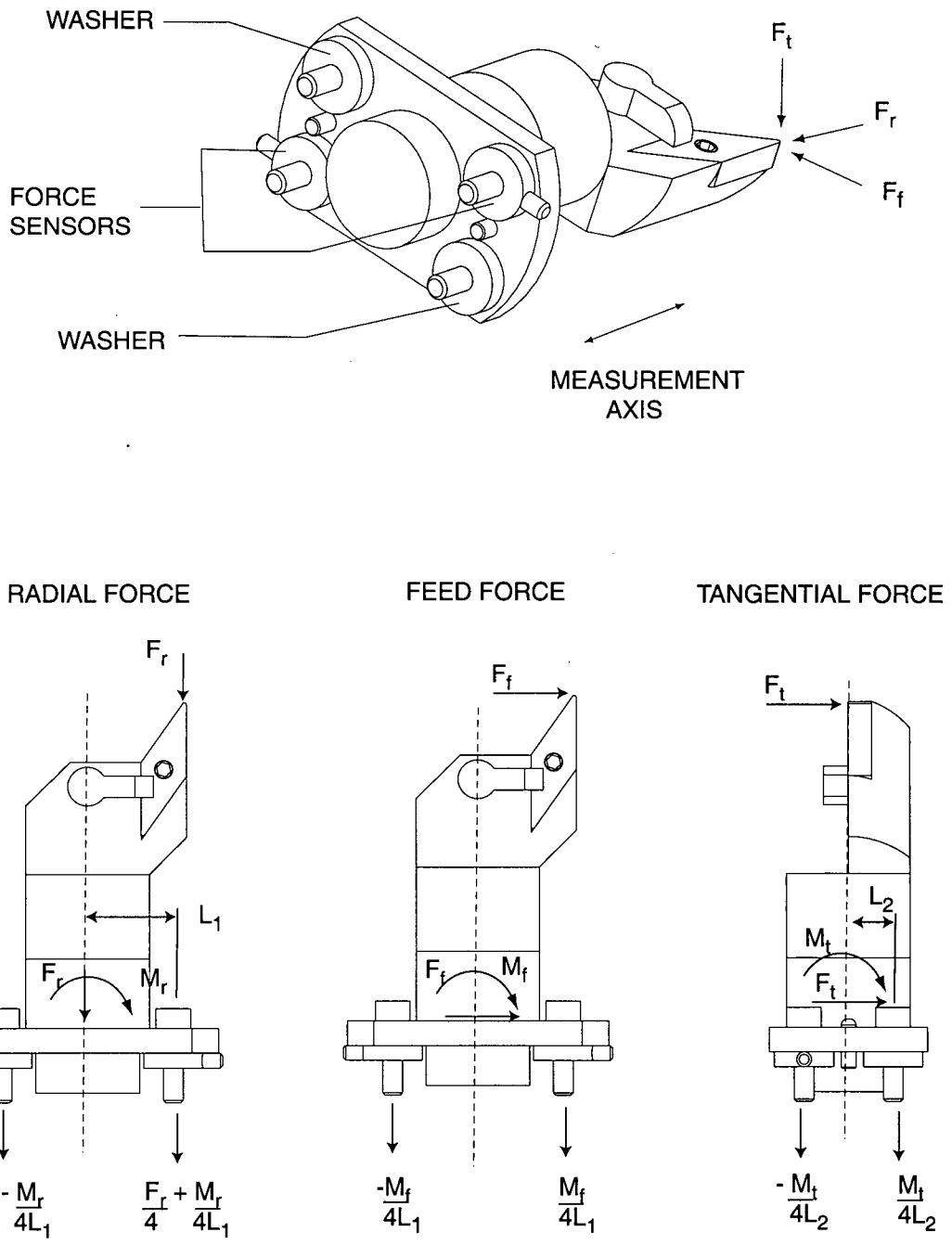

Figure 3.10 : Force sensor arrangement for measurement of radial cutting forces.

Model	Kistler 9132A
Range	10 kN
Resolution	< 0.01 N
Stiffness	1.8 kN/micron
OD	12 mm
ID	4.1 mm
Thickness	3 mm
Preload	50% FS for series connection

Table 3.2 : Single axis force sensor specifications.

3.5.2. Piezoelectric driving element

A high voltage piezoelectric translator is chosen as the driving element as it offers many advantages for machine tool applications over other actuators. In general, piezoelectric actuators provide sub-nanometer expansion, smooth motion (no friction or stick-slip), high mechanical stiffness, and high force generation. The main drawbacks are low resistance to tensile and shear stresses, small stroke, high heat generation, and non-linear deformation. The translator used is a stack actuator, composed of many thin disks of lead-zirconate-titanate (PZT) ceramic material, connected with electrodes. The PZT material exhibits the piezoelectric effect, whereby an applied electric field causes a proportional mechanical deformation. The deformation is the result of changing alignment of the atoms within the PZT crystal structure, and is not associated with a change in crystal structure. Although the degree of deformation is quite small, when many PZT disks are stacked together the resultant deformation is substantial. In general, the maximum deformation of a stack actuator is approximately 0.1% of the stack length.

Stack actuators can be delivered in both preloaded and bare configurations. Since a stack is comprised of many thin PZT disks, preloading is required to maximize the contact area between disks as well as reducing the effect of the flexible bonding material. Thus the preload maximizes the stack stiffness and stroke, and for dynamic operation to ensures the stack remains in contact

with the structure. A preloaded actuator is delivered encased in steel with a small flexure mechanism providing the preload as shown in Figure 3.11. A bare stack requires the user to provide the stack preload. To meet the design constraints on the radial dimension of the actuator, a bare stack was selected as it offered a 30 % reduction in length compared with a preloaded stack. In this case the Guiding Unit flexures must provide adequate preload of the piezoceramic. This is achieved by selecting a proper stack up length of the PZT translator and Alignment Washer (Figure 3.4), which exceeds the available space in the Guiding Unit. By deflecting the flexures to accommodate the PZT stack a constant preload is provided. To satisfy the stroke and stiffness constraints, a stack actuator with a 40 micron stroke and 25 mm diameter from Piezomechanik GmbH was selected. The specifications of the piezostack are listed in Table 3.3.

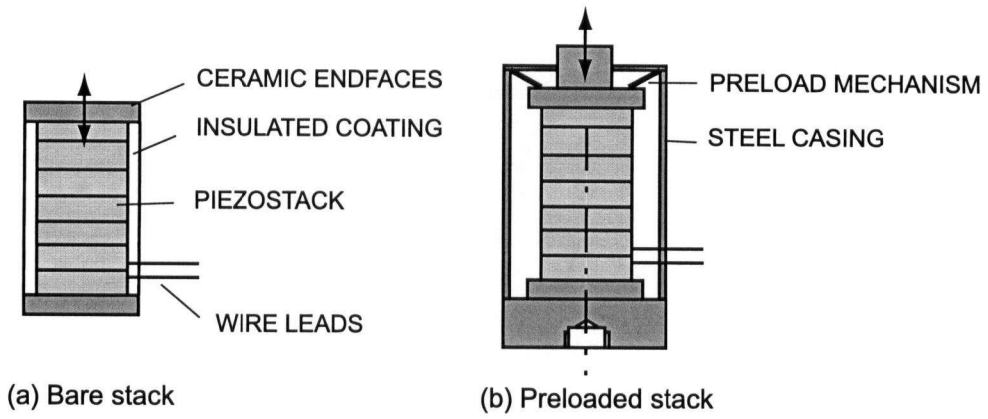

Figure 3.11 : Bare and preloaded piezostack configurations.

Stroke	40 micron
Length	36 mm
Diameter	25 mm
Stiffness	450 N/micron
Resonant Frequency	25 kHz
Capacitance	1 μF
Blocking Force	16 000 N
Voltage Range	0 to +1000V

Table 3.3 : Driving piezoelectric actuator specifications.

3.5.3. Guiding Unit

The Guiding Unit is the main structural component of the precision turning actuator. The component model is shown in Figure 3.12, along with dimensions of the hinge profile. The four solid flexures, each with two circular hinges, allow the moving section to deform linearly in the radial direction under applied load from the piezoelectric stack actuator. The advantages of solid hinges over jointed mechanisms are increased rigidity, zero friction or stick slip, and no wear. The Guiding Unit, as well as the Top and Bottom plates, are machined out of titanium alloy Ti-Al6-V4, which has a high strength to density ratio compared with steel. The material properties are given in Table 3.4. The entire structure is machined using wire EDM to avoid residual stresses and contour errors along the hinge profiles, commonly associated with milling and drilling operations. The flexure and hinge dimensions are optimized for minimal size and maximum rigidity. The spacing between the flexures is set based on the size of the clamping units which apply clamping forces on the moving section of the Guiding Unit when activated.

Density	4.43 Mg/m^3
Modulus of Elasticity	120 GPa
Modulus of Rigidity	44 GPa
Yield Strength	924 MPa
Ultimate Strength	1000 MPa
Poisson's Ratio	0.36
Fatigue Limit	560 MPa
Coef. of thermal expansion	9.4 E-6 /°C

Table 3.4 : Titanium alloy (Ti-6Al-4V) properties [55].

The structural properties of the Guiding Unit are determined by the geometry of the flexure hinges. The first step in optimization of the hinge profile is to determine the stiffness requirement. When housed within a flexible structure, the stroke of a piezoelectric actuator is reduced according to Equation 3.2, where K_t is the stack stiffness, K_x is the flexure stiffness, ΔL_o is the stroke under free conditions (nominal), and ΔL is the reduced stroke.

$$\Delta L = \Delta L_o \cdot \frac{K_t}{K_t + K_x} \tag{3.2}$$

The rigidity of the Guiding Unit must be limited, as increasing stiffness decreases the overall stroke of the system. Thus a compromise is required between minimum stiffness in the radial direction and maximum stiffness in the perpendicular directions. The maximum reduction in stroke is set to 5% (2 microns), such that the constraint on stroke is safely satisfied. Based on the actuator stiffness K_t = 450 N/micron, and nominal stroke ΔL_o = 40 microns, the maximum allowable radial stiffness of the flexures, K_x, is 23 N/micron. This corresponds to an effective stroke ΔL of 38 microns.

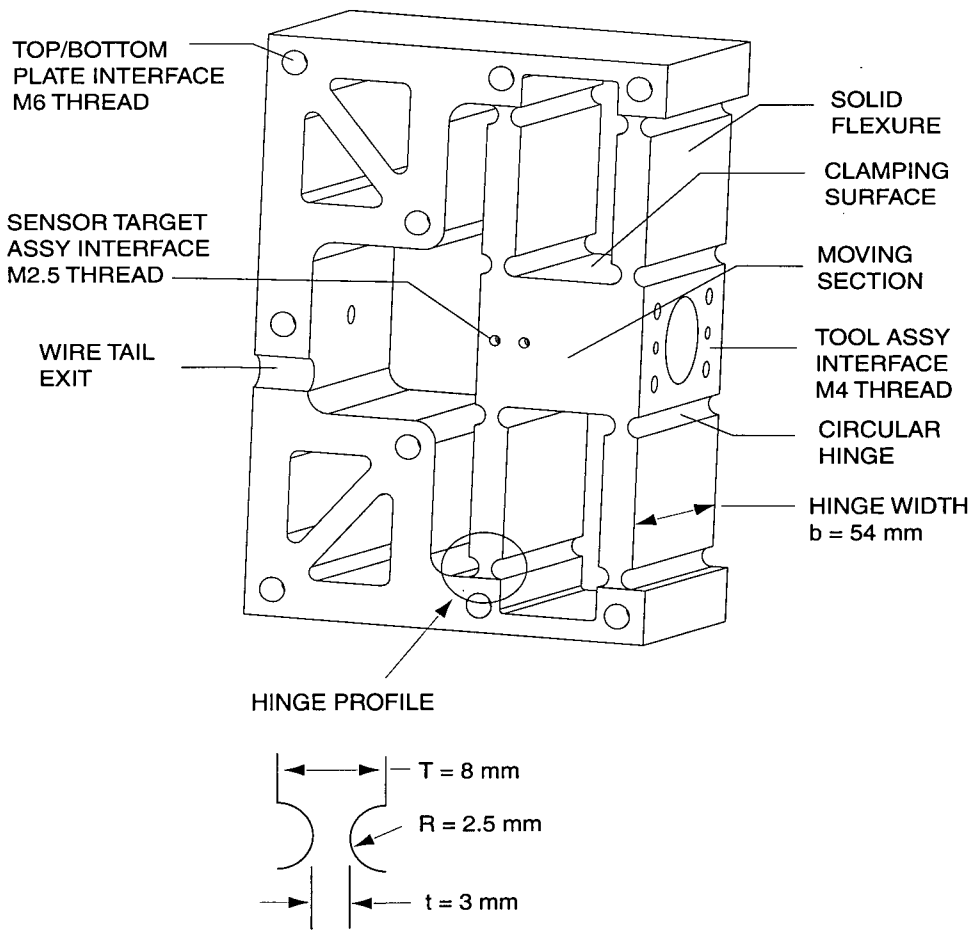

Figure 3.12 : Actuator Guiding Unit and flexure hinge profile.

3.5.3.1. Analytical model of flexures

An analytical model of the Guiding Unit flexures was developed to predict the static stiffness of the flexure hinges in the radial direction for a range of hinge parameters (radius and thickness). Figure 3.13 presents the Guiding Unit structure (a), the approximated model considering the flexibilities of the circular hinges (b), the linear spring model where each flexure is modeled as an equivalent linear spring $K_{x,F}$ (c), and the equivalent radial stiffness K_x (d), which is the sum of the equivalent linear stiffness for each flexure acting in parallel. The system is considered rigid except for the flexure hinge rotational (K_B) and axial (K_S) flexibilities which are given by Equations 2.2 and 2.3. The torsional and axial springs act at the hinge centres. The equivalent radial stiffness for a single flexure is determined by adding the effective linear stiffness due to hinge bending, $K_{x,FB}$, and stretching, $K_{x,FS}$, as shown in Figure 3.14. The values $K_{x,FB}$ and $K_{x,FS}$ are determined by equating the potential energy of the displaced system to the external work done by a force F, acting at the centreline of the structure in the radial direction, deforming the structure a distance x. Motion is constrained to the x-direction due to the compound arrangement of the flexures, thus the translational degree of freedom x has a roller support.

First the effect of bending stiffness is considered, illustrated in Figure 3.14. A force F_1 displaces the flexure a distance x. Due to the roller support constraint the rotational displacement of each of the two torsional springs, θ, is the same. The following relation is obtained for small angles of rotation,

$$\theta \approx \tan\theta = \frac{x_2}{L_1} = \frac{(x_2 - x)}{L_2}$$

solving for the displacement yields $x = \theta(L_1 - L_2)$, or $\theta = \frac{x}{(L_1 - L_2)}$.

The total potential energy for the two deformed torsional springs with equal spring constants and displacements is expressed as

$$U = \frac{1}{2}K_B\theta^2 + \frac{1}{2}K_B\theta^2 = K_B\theta^2$$

substituting for the rotation θ,

$$U = \frac{K_B x^2}{(L_1 - L_2)^2}$$

The external work done by the force F_1 in deforming a virtual linear spring $K_{x,FB}$ a distance x is

$$W = \int_0^x F_1 dx = \int_0^x K_{x,FB} x dx$$

$$W = \frac{1}{2}K_{x,FB}x^2$$

Equating the potential energy and external work (no kinetic energy) yields Equation 3.3 for the equivalent stiffness in the radial direction due to the flexure rotational stiffness

$$K_{x,FB} = \frac{2K_B}{(L_1 - L_2)^2} \tag{3.3}$$

The equivalent stiffness $K_{x,FS}$ due to flexure axial stiffness is derived in a similar fashion. From the geometry of Figure 3.14 the following relation is obtained, where δL is the combined elongation of both springs.

$$\delta L = L_4 - L_3 = \sqrt{L_3^2 + x^2} - L_3$$

The resultant stiffness, $K_{S,r}$, for the two springs K_S acting in series is

$$K_{S,r} = \frac{K_S}{2}$$

The potential energy for an elongation δL is given by

$$U = \frac{1}{2}K_{S,r}\delta L^2 = \frac{1}{2}K_{S,r}(\sqrt{L_3^2 + x^2} - L_3)^2$$

The external work done on the flexure due to force F_2 is expressed with the equivalent virtual spring stiffness $K_{x,SF}$. Note that the linear stiffness $K_{x,SF}$ is a function of the displacement x (at zero displacement there is no stiffness, and at infinite displacement stiffness approaches $K_{S,r}$).

$$W = \int_0^x F dx = \int_0^x K_{x,SF}(x) x dx$$

Equating the derivatives of the work and potential energy yields the expression for $K_{x,SF}$ given by Equation 3.4.

$$\frac{dW}{dx} = \frac{dU}{dx}$$

$$K_{x,SF}(x) = K_{S,r}\left(1 - \frac{L_3}{\sqrt{x^2 + L_3^2}}\right) \tag{3.4}$$

The equivalent linear springs $K_{x,FB}$ and $K_{x,SF}$ act in parallel, and are added to obtain the equivalent linear stiffness for a single flexure $K_{x,F}$ in Equation 3.5.

$$K_{x,F} = K_{x,FB} + K_{x,SF} = \frac{2K_B}{(L_1 - L_2)^2} + K_S\left(1 - \frac{L_3}{\sqrt{x^2 + L_3^2}}\right) \tag{3.5}$$

Finally the resultant radial stiffness of the system due to both bending and stretching of the four flexures acting in parallel is given by Equation 3.6.

$$K_x = 4K_{x,F} = \frac{8K_B}{(L_1 - L_2)^2} + 4K_S\left(1 - \frac{L_3}{\sqrt{x^2 + L_3^2}}\right) \tag{3.6}$$

where $K_B = \frac{2Ebt^{5/2}}{9\pi r^{1/2}}$, and $K_S = \frac{Eb}{\pi(r/t)^{1/2} - 2.57}$

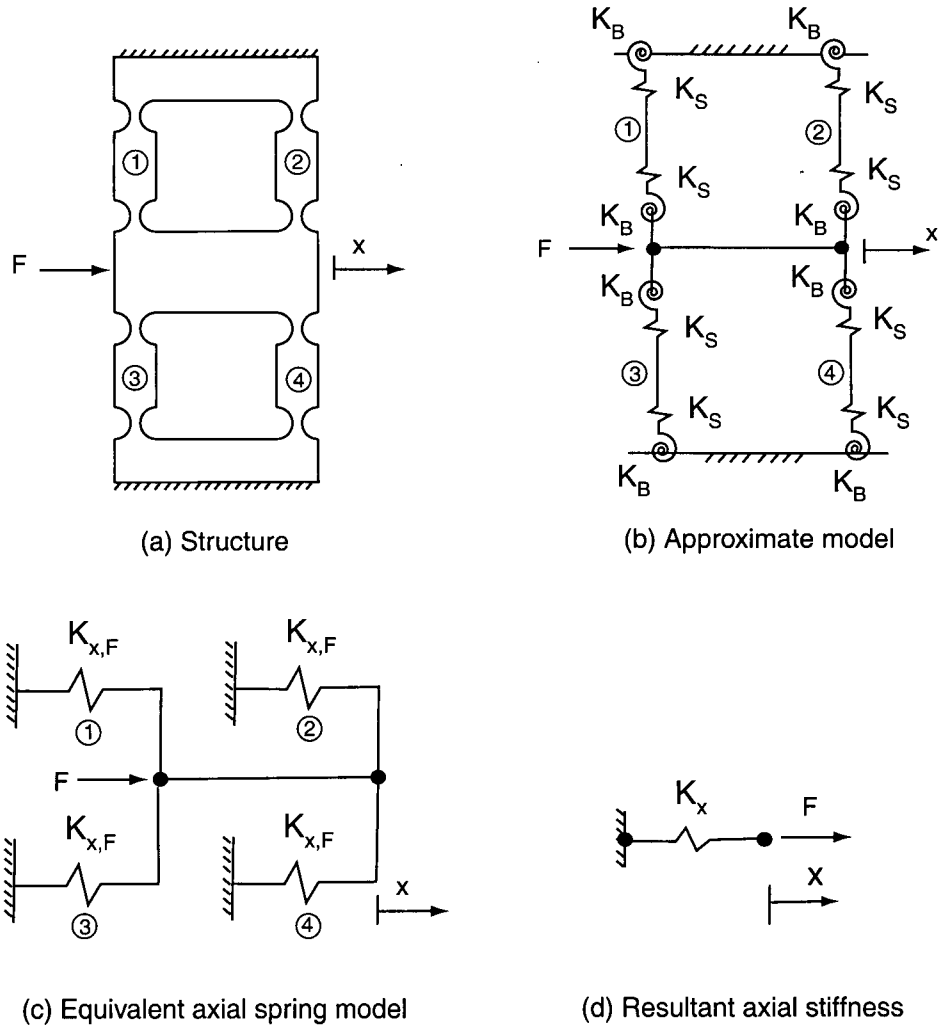

Figure 3.13 : Guiding Unit model for equivalent linear stiffness based on flexure hinge flexibility in rotational and axial directions.

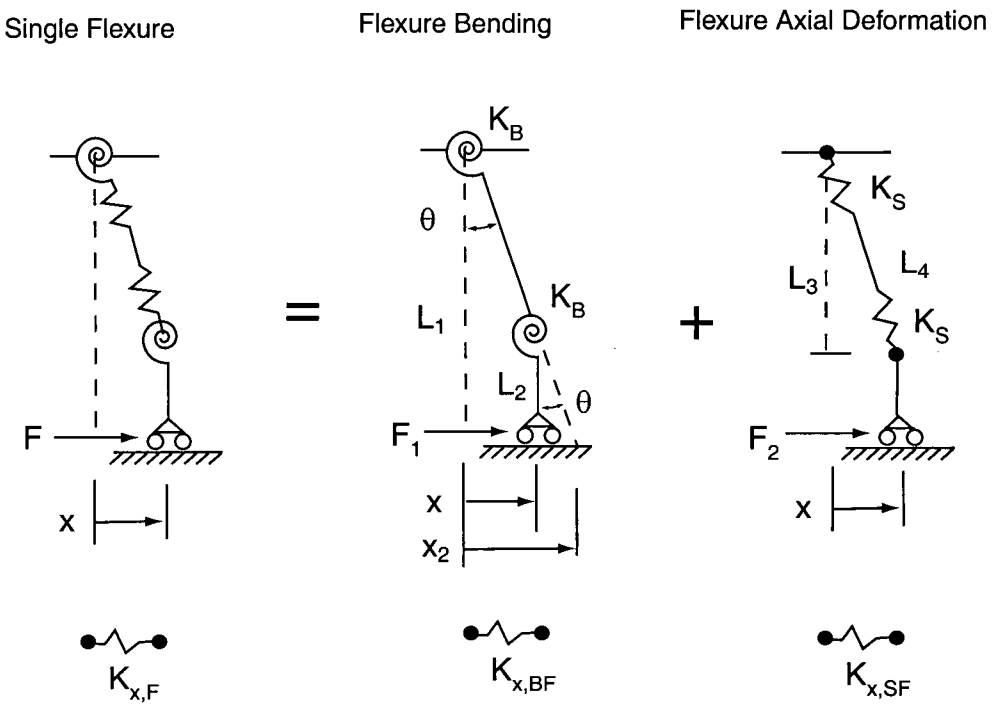

Figure 3.14 : Superposition of a single hinge bending and axial stiffness to obtain the equivalent linear stiffness.

The following parameters are given from the initial design; L_1 = 0.056 [m], L_2 = 0.019 [m], L_3 = 0.042 [m], b = 0.054 [m], and E = 120 [GPa]. The dependence of the linear stiffness K_x on the displacement x (Equation 3.6) is eliminated by considered the relative contributions of bending and axial stiffness. For linear displacements of the structure less than 0.1 mm, the axial stiffness contributes less than 1% of the total stiffness, thus it can be ignored for small displacements. In order to size the circular hinge the radial stiffness is plotted versus hinge radius for a range of hinge thickness values in Figure 3.15. Plotted in the figure is the target stiffness of 23 N/micron, which is satisfied by selecting a preliminary hinge geometry with 3.25 mm radius, and 3.0 mm thickness.

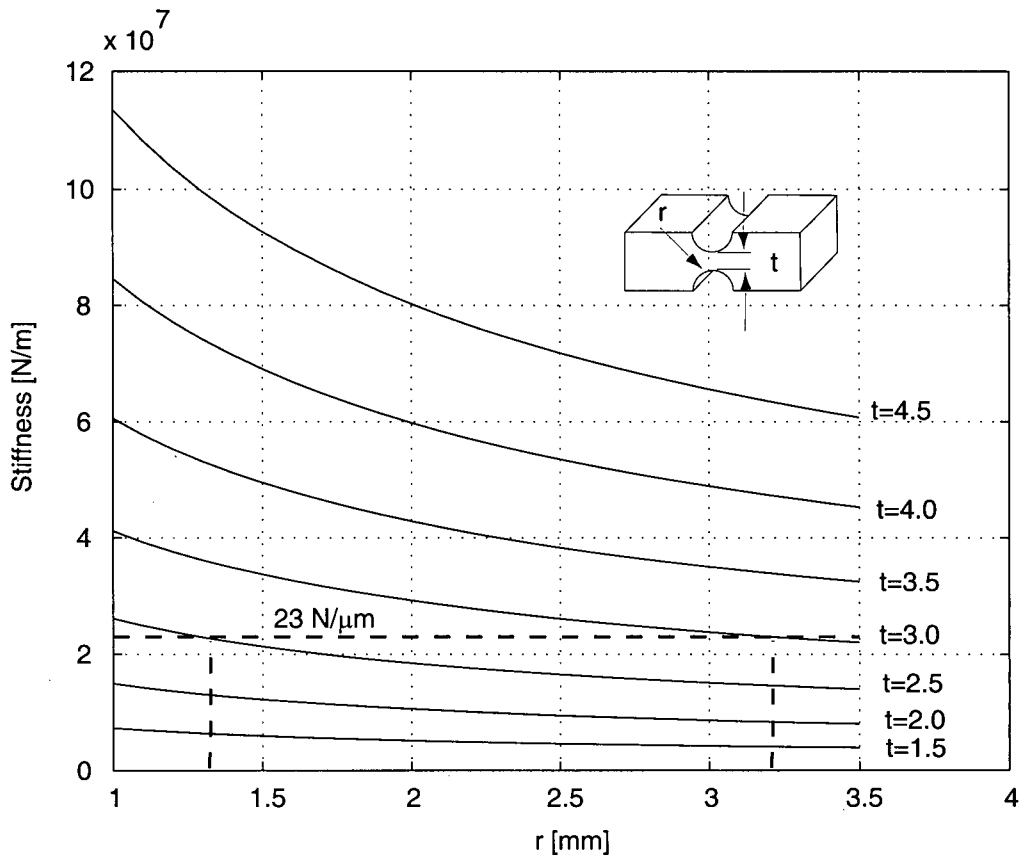

Figure 3.15 : Guiding unit stiffness versus hinge radius for varying hinge thickness.

3.5.3.2. Finite element model of flexures

A finite element model of the Guiding Unit flexures was created in ANSYS consisting of 8 noded block elements (SOLID45). This model was used to determine the stresses under maximum loading, the stiffness in each direction, as well as the mode shapes and natural frequencies of the flexures. The circular hinge had 10 elements distributed along the profile. The bases of the flexures were constrained in all directions to zero displacement, representing the bolting locations to the support plates. Starting with the preliminary values determined from the analytical model,

the hinge geometry is optimized. The target stiffness is achieved when the hinge radius is reduced to 2.5mm, at a hinge thickness of 3mm. The finite element model showed lower stiffness compared to the analytical model, as in the analytical model the structure was considered rigid except for the hinge bending and axial deformation. The stiffness in each direction was determined by applying a 1 N load in the desired direction, and determining the maximum deformation in the same direction (inverse being the stiffness). For the radial direction the load was applied as a pressure of 2038 Pa to the area (4.9e-4 m^2) in contact with the piezoelectric translator. The results are summarized in Table 3.5. As expected the structure is substantially stiffer in the feed and tangential directions compared with the radial stiffness. The first three mode shapes of the structure are presented in Figure 3.16. The first mode is axial displacement of the flexures in the radial direction, and occurs at 1215 Hz which exceeds the design constraint of 1000 Hz. The second mode at 5690 Hz is torsion about the y axis, and the third mode corresponds to transverse motion in the feed direction at 6826 Hz

Direction	Load [N]	Displacement [micron]	Stiffness [N/micron]
Radial (x)	1	0.0436	23
Tangential (y)	1	0.000496	2016
Feed (z)	1	0.00142	704

Table 3.5 : Guiding Unit stiffness determined from finite element model.

The flexures and piezoelectric translator act as two springs in parallel, thus the overall stiffness of the system in the radial direction, assuming the back plate of the Guiding Unit is fixed, is given by:

$$K_R = K_t + K_x = 450 + 23 = 473 \text{ [N/micron]}$$

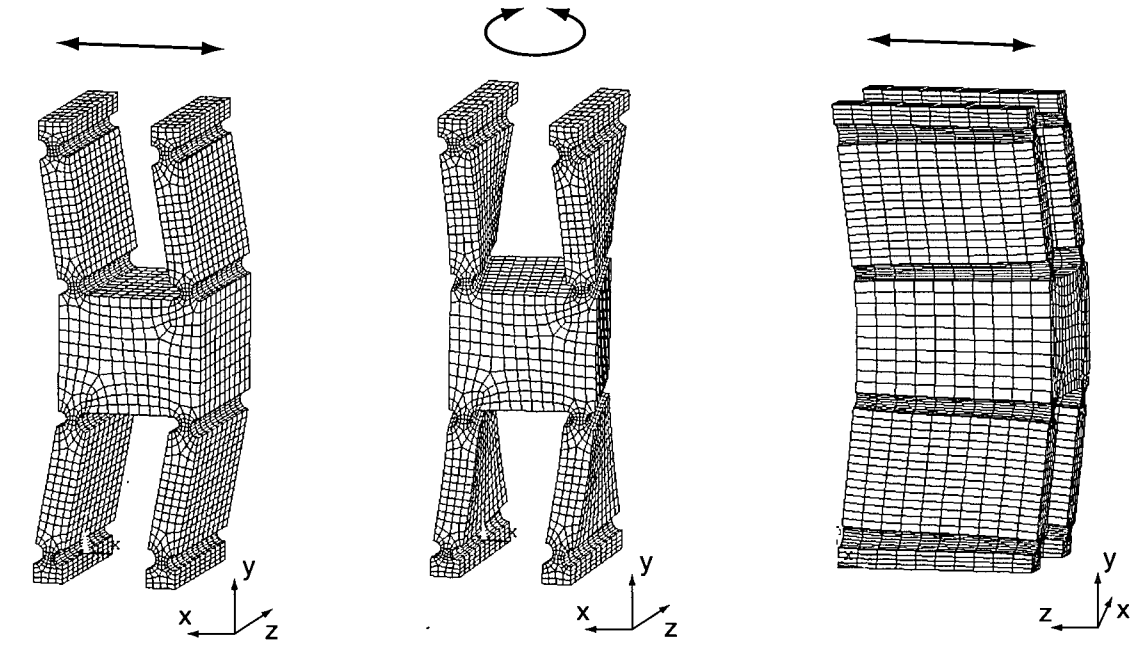

Figure 3.16 : Mode shapes of the Guiding Unit flexures determined from FE model.

The effective mass of the moving components is the sum of the tool assembly, the moving section, and a fraction of the PZT translator and flexure masses. As a rule one third of the PZT mass is considered for dynamic cases. The mass is approximated as 1.1 kg.

$$m_{eff} = m_{tool} + m_{ms} + \frac{1}{3}m_{PZT} + \frac{1}{3}m_{f,GU}$$

$$m_{eff} = 0.5 + 0.38 + 0.1 + 0.12 = 1.1 \text{ [kg]}$$

The natural frequency in the radial direction assuming a single degree of freedom system is

$$f_N = \frac{1}{2\pi}\sqrt{\frac{K_R}{m_{eff}}} = 3302 \text{ [Hz]}$$

The maximum load in the radial direction applied to the flexures is the sum of the piezoelectric translator preload and the force required to displace the flexures the maximum stroke of the translator. The preload must be higher than any inertial forces on the moving section such that the piezoelectric translator remains in contact with the Guiding Unit at all times. The amplitude of the dynamic load F_d for a structure of mass m vibrating at natural frequency ω with amplitude A is given by Equation 3.7. For the flexures the effective mass is considered, and the maximum vibration amplitude is simply half the stroke, as in Equation 3.8. The maximum dynamic load for the Guiding Unit flexures is given by Equation 3.9, where f_{GU} is the frequency of mode 1 (1215 Hz), ΔL is the actuator stroke (40 micron), and the effective mass consists of the mass of the moving section m_{ms} and one third of the flexure mass m_f.

$$F_d = m\omega^2 A \tag{3.7}$$

$$F_d = 4\pi^2 \cdot m \cdot f^2 \cdot \frac{\Delta L}{2} \tag{3.8}$$

$$F_{d,GU} = 4\pi^2\left(m_{ms} + \frac{m_{f,GU}}{3}\right) f_{GU}{}^2 \cdot \frac{\Delta L}{2} = 582 \text{ [N]} \tag{3.9}$$

The preload on the structure must be greater than the dynamic load to ensure the flexures remain in contact with the PZT translator. Using a factor of safety of 2, the PZT preload $F_{P,GU}$, is set to 1164 N.

$$F_{P,GU} = FS \times F_{d,GU} = 1164 \text{ [N]}$$

The maximum load F_L due to piezoelectric translator expansion is the product of the flexure stiffness and maximum actuator expansion, given by Equation 3.10. The resultant maximum load on the Guiding Unit flexures, F_{RES} is the sum of the preload and force required to displace the flexures the full actuator stroke. From Equation 3.11 the maximum load is 2084 N.

$$F_L = K_X \cdot \Delta L = 920 \text{ [N]} \tag{3.10}$$

$$F_{RES} = F_{d,GU} + F_L = 2084 \text{ [N]} \tag{3.11}$$

With the maximum load applied in the radial direction, the resulting Von Mises stresses are given in Figure 3.17, with the maximum stress being 135 MPa. This value is well below the fatigue limit of titanium alloy. The stress is distributed entirely within the circular hinges, as there is no bending of the flexures or of the moving section in the symmetric structure. In order to provide the preload, the flexures must be initially displaced 51 microns in the radial direction based on the flexure stiffness and preload, according to Equation 3.12.

$$\delta_{GU} = \frac{F_{P,GU}}{K_x} = \frac{1164\ \text{N}}{23\ \text{N}\mu m^{-1}} = 51\ [\mu m] \tag{3.12}$$

The initial displacement is achieved via surface grinding of the alignment washer such that the stack up length of the piezoelectric translator and alignment washer (Figure 3.4) is 51 microns greater than the available space in the Guiding Unit frame. Surface grinding of the alignment washer is necessary as the manufacturer's tolerance on piezostack length is +/- 0.5 mm. The flexures are deformed using the four tapped holes at the tool adapter interface to accommodate the piezoelectric translator and alignment washer.

3.5.4. Position sensor assembly

A capacitive position sensor is chosen due to its high resolution, small size, and ease of integration to the design. The sensor consists of two plates, a fixed probe and a moving target, forming an air capacitor. As the target moves the change in capacitance between the two plates is compared to a reference capacitor within the electronics card, and a voltage corresponding to the change in position is output. The output voltage U_{out} is given by Equation 3.13, where d is the plate spacing, and d_o is the nominal range,

$$U_{out} = 10 \times \left(\frac{d}{d_o} - 1 \right) \tag{3.13}$$

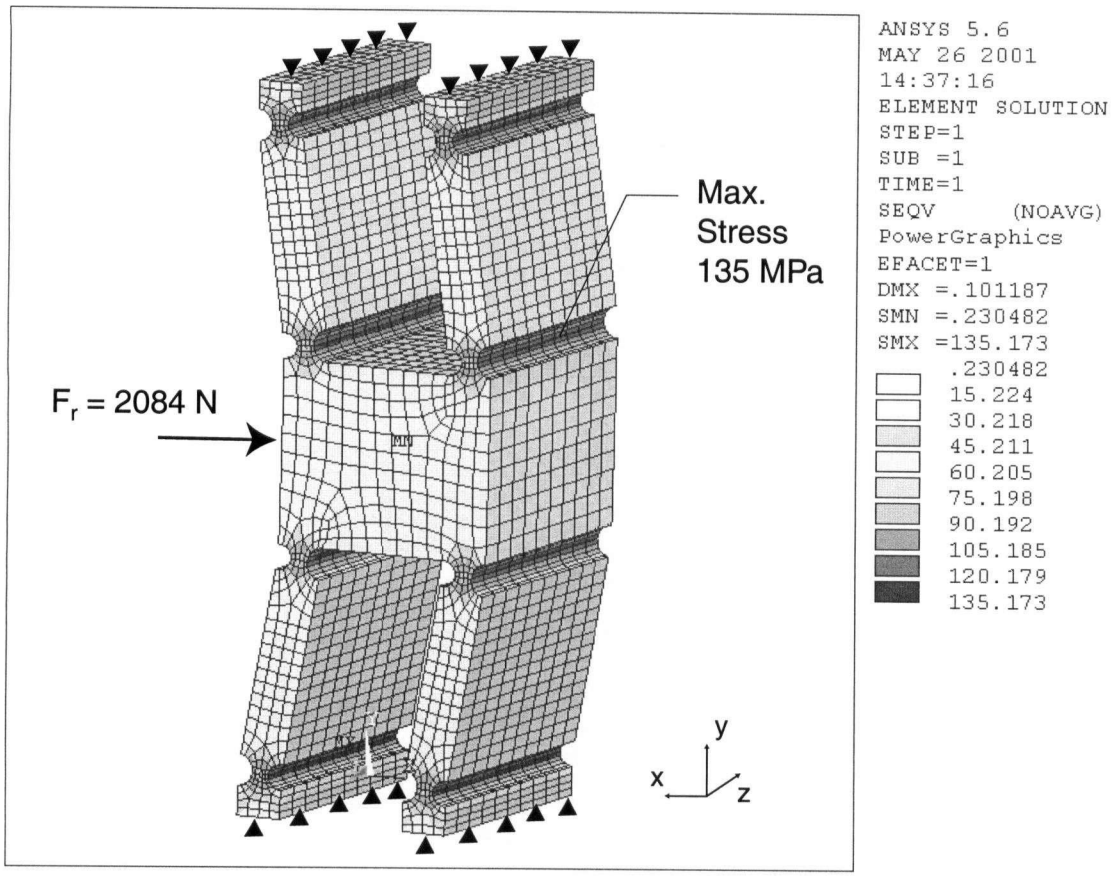

Figure 3.17 : Finite element result for Guiding Unit stresses under maximum radial load.

The position sensor assembly is presented in Figure 3.18, and the sensor specifications are given in Table 3.6. The mounting brackets are machined out of aluminum to match the plate casing material, such that thermal deformation in the assembly has limited effect on sensor plate flatness. The weakest component is the probe bracket, which has longer overhang than the target bracket. Any vibration of the probe bracket will cause error in the position measurement, thus the first mode of the bracket must have a sufficiently high frequency. A finite element model of the probe bracket was created, consisting of five noded tetragonal elements, and a modal analysis was conducted. The bracket is constrained to zero displacement at the bolting locations to the Top Plate. The first bending mode of the bracket occurs at 6756 Hz, shown in Figure 3.19.

Range	50 micron (extendable to 150 micron)
Resolution	5 nm
Bandwidth	Adjustable 300, 1000, or 3000 Hz
Material	Aluminum
Resonant Frequency	20 KHz
Sensitivity	0.2 volt/micron

Table 3.6 : Capacitive position sensor specifications.

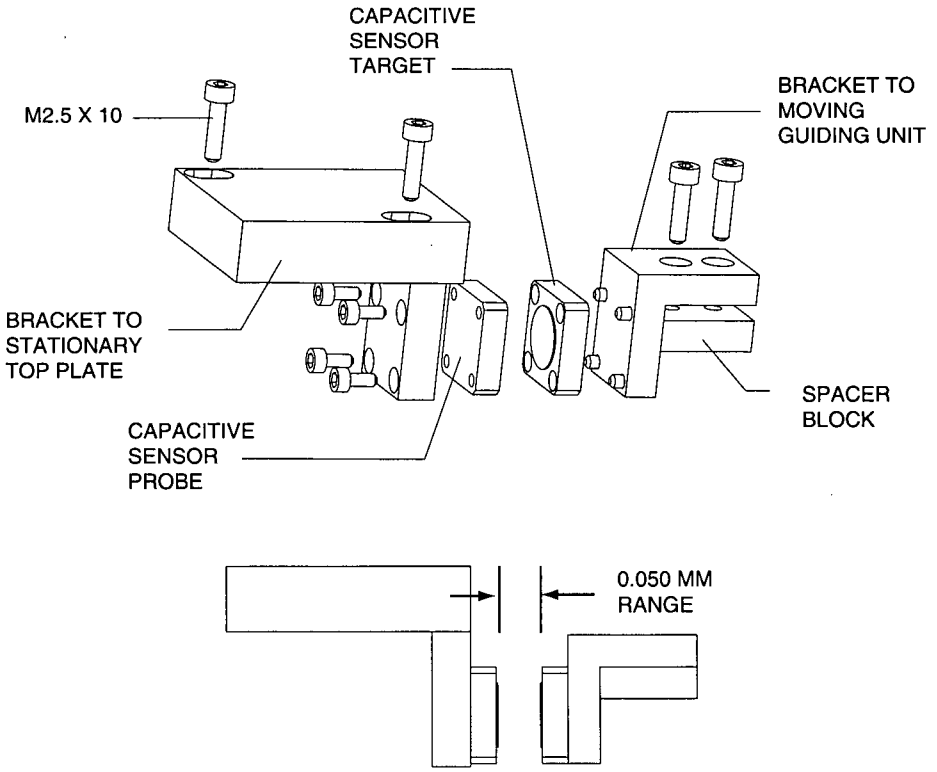

Figure 3.18 : Capacitive position sensor assembly.

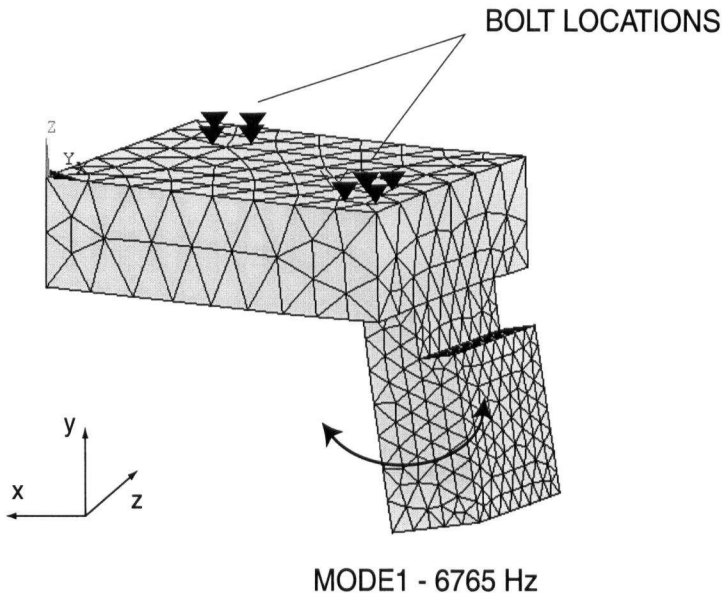

Figure 3.19 : Finite element result for first bending mode of the sensor probe bracket.

3.5.5. Support plates

The Guiding Unit is supported by the Top and Bottom plates, each of which provides nine mounting locations to the Guiding Unit structure (see Figure 3.3). As well the support plates provide a stationary interface for the two Clamping Units at four counterbore locations on each plate. The counterbores are enlarged to allow for adjustment in the position (y direction) of the Clamping Units relative to the Guiding Unit moving section. Wire cutouts are included on the Bottom Plate to allow passage of the Clamping Unit piezostack input cables underneath the flexures. Of the Guiding Unit support plates, the Bottom Plate is most crucial as it provides the interface to the turret slot. The plate should be rigid such that cutting forces do not excite bending and twisting modes at the turret interface. Eight noded block elements were used to create a finite element model of the plate, and a modal analysis was performed, with the results shown in Figure 3.20. The first and second bending modes of the plate occur at 1551 Hz and 2741 Hz, respectively. The

third mode is torsion about the y axis, and occurs at 3047 Hz. All frequencies are above the design constraint of 1000 Hz.

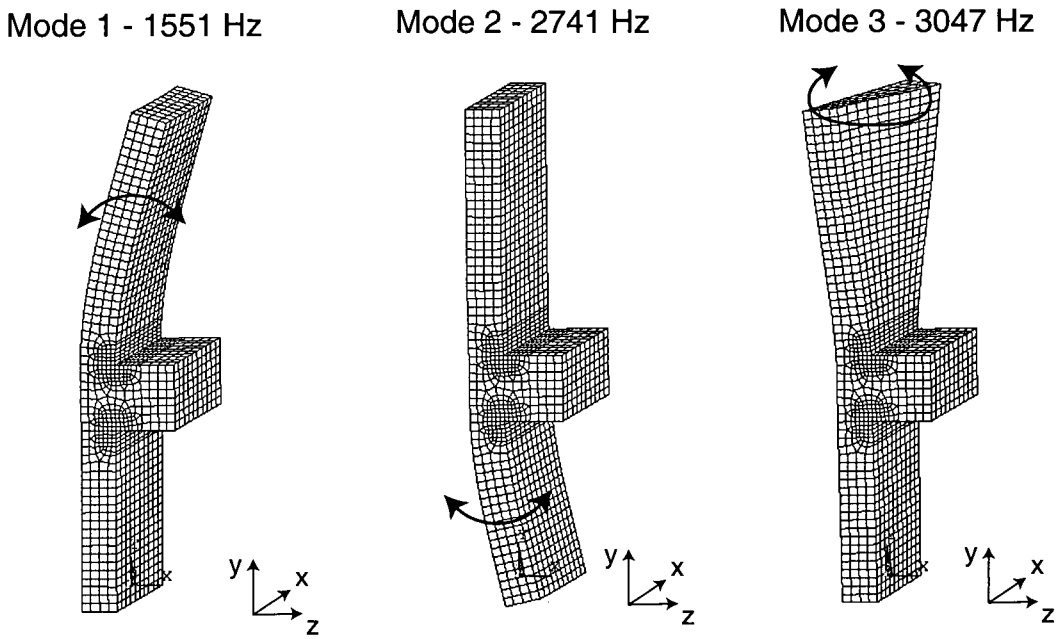

Figure 3.20 : Finite element result for first three Bottom Plate vibration modes.

3.5.6. Clamping Units

The Clamping Unit assembly was designed by Bracht [34] for use in a long range two stage piezoelectric drive, and is presented in Figure 3.21. The assembly consists of a housing with solid flexures, a piezoelectric stack actuator, and an alignment washer. Four M6 bolt locations are used to fasten the Clamping Unit to the Top and Bottom plates. As with the Guiding Unit, expansion generated from the piezostack is transmitted through the flexures to the top surface. By activating the piezoelectric driving element, the flexure of the Clamping Unit deforms until it is in contact with the moving section of the Guiding Unit. When both clamping units are activated the moving section of the Guiding Unit is clamped (Figure 3.4), as long as the frictional forces in the

contact area are not exceeded, and the overall rigidity of the system is increased in each direction. The piezoelectric stack actuator selected has a 30 micron stroke, and 27 mm length, manufactured by Piezomechanik GmbH. The specifications of the clamping unit piezostack are given in Table 3.7. As with the main driving element, the inertial forces of the moving section must be determined to set an adequate preload for the piezoelectric translator. The stiffness of the Clamping Unit flexure have been determined by [34] using finite element analysis, and given as $K_{cu,x} = 250\ [\mathrm{N}/\mu m]$, $K_{cu,y} = 39\ [\mathrm{N}/\mu m]$, and $K_{cu,z} = 143\ [\mathrm{N}/\mu m]$.

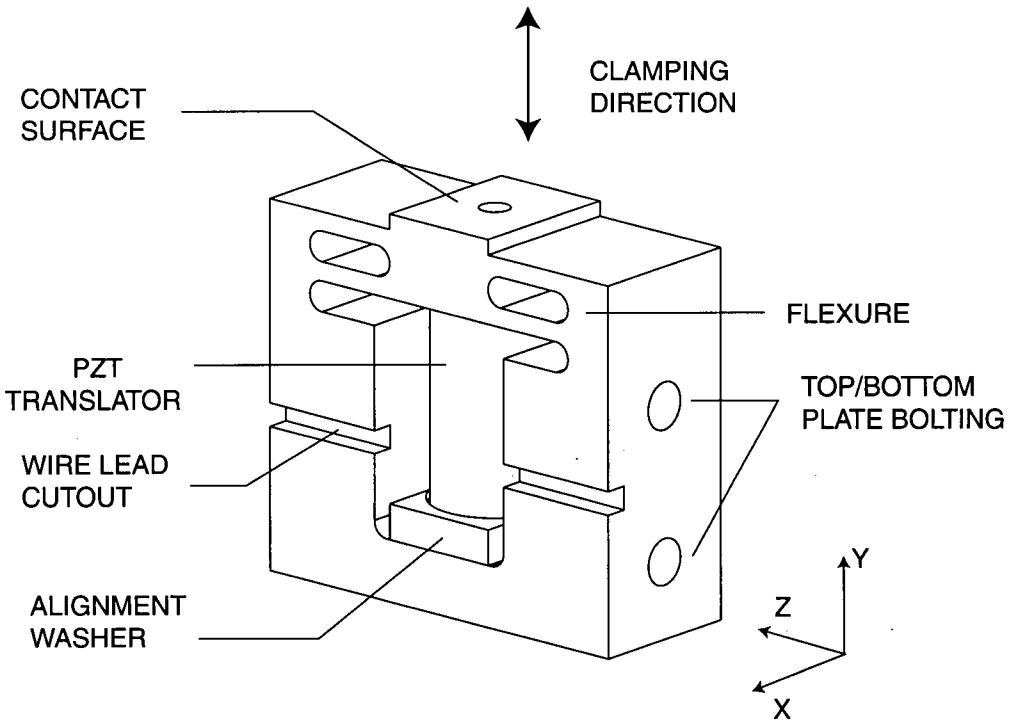

Figure 3.21 : Clamping Unit assembly details.

Stroke	30 micron
Length	27mm
Diameter	16mm
Stiffness	200 N/micron
Resonant frequency	25 KHz
Capacitance	0.3 μF
Blocking force	6000 N
Max. compressive load	6000 N
Voltage range	0 to +1000V

Table 3.7 : Specifications of the Clamping Unit piezostack.

The natural frequency in the y direction is approximated based on $K_{cu,y}$, and the effective mass of the flexure (0.032 Kg), and calculated as 5560 Hz.

$$f_{CU} = \frac{1}{2\pi}\sqrt{\frac{K_{cu,y}}{m_{f,CU}}} = 5560 \quad [\text{Hz}]$$

The amplitude of the dynamic forces due to resonance of the moving section is given by

$$F_{d,CU} = 4\pi^2 f_{CU}^2 \cdot \frac{\Delta L}{2} \cdot m_{f,CU} = 585 \text{ [N]}$$

The preload on the piezostack, $F_{P,CU}$, is set as 1170 N using a factor of safety of 2. The flexures must be deflected an amount δ_{CU} to provide the preload. The flexures are displaced to accommodate the piezostack and alignment washer via fastener locations on the clamping and bottom surface.

$$\delta_{CU} = \frac{F_{P,CU}}{K_{cu,y}} = \frac{1170}{39} = 30 \quad [\text{micron}]$$

The reduction in stroke of the piezostack is determined based on the stiffness of the flexure in the y direction, giving a total stroke of 25 microns.

$$\Delta L_{CU} = \Delta L_{o,CU} \cdot \frac{K_t}{K_t + K_{cu,y}} = 25 \quad [\text{micron}]$$

Clamping of the Guiding Unit is only effective if the generated frictional forces are higher than the radial cutting force, such that mating surface remain in contact. Given a clearance of 10 microns between the contact surface in the unclamped mode (Figure 3.4), the normal force F_N achieved by each clamping unit is the product of the available stroke and stiffness,

$$F_N = (\Delta L_{cl} - 10) \cdot (K_{cu,x} + K_{t,cu}) = 3585 \text{ [N]}$$

Assuming of coefficient of friction of 0.55 for titanium-titanium contact [56], the generated frictional force for by two Clamping Units is 3944 N, which exceeds the maximum expected radial cutting force of 1000 N.

$$F_{friction} = 2\mu F_N = 3944 \text{ [N]}$$

3.6. Summary

An overview of the requirements for the precision turning actuator design were given, which include constraints on motion, stiffness and natural frequency, size, and operability. The design details and operation of the piezoelectric tool actuator have been presented, as well as the structural analysis of the major functional components. The important features of the design are the use of a piezoelectric driving element in series with double parallel flexures to transmit motion to the tool assembly. The actuator accommodates standard exchangeable tooling, and has a compact, symmetric design. In addition force sensors can be mounted at the tool adapter interface for measurement of the radial cutting forces. A capacitive sensor is used for position feedback.

An analytical model was developed for preliminary sizing of flexure hinge geometry based on the desired radial stiffness of 23 N/micron, which resulted in a reduced total actuator stroke of 38 microns. The hinge geometry was further optimized using a finite element model. The natural frequency of the first radial mode is predicted to by 3300 Hz, using the manufacturer's specification for PZT stack axial stiffness. The dominant mode shapes of the Guiding Unit, sensor bracket,

and Bottom Plate were shown to be greater than the design constraints. Based on the inertial loads caused by vibration of the flexures, the preload required to keep the piezoelectric actuator in contact with the mating surfaces was determined to be 1200 N for both the Guiding Unit and the Clamping Unit. To provide the preload the required displacement of the flexures to accommodate the PZT stacks and alignment washers was determined. Based on the predicted maximum radial due to the preload at maximum stroke, the stresses in the flexures were determined using the finite element model and shown to be below the fatigue limit of the titanium alloy.

Chapter 4

System Identification and Control

4.1. Introduction

In this chapter the electrical and mechanical properties of the assembled actuator system are identified and discussed, and a controller is designed to meet the positioning requirements for the precision turning cutting process. An overview of the system instrumentation and signal flow for feedback control is included. Identified system properties include the non-linearities associated with piezoceramic devices, the modal properties of the actuator structure, the calibration of the feedback sensor, and the dynamics of the feedback sensor electronics. A model of the actuator is developed based on the assumption of a second order system, and a static gain relating input voltage to force input to the system. A sliding mode controller design is adopted based on previous work by Zhu et al [32], which demonstrated accurate positioning and rejection of cutting force disturbances when applied to a piezoelectric actuator for precision machining. The controller design steps are outlined, and the control law is obtained. Based on the demands of the precision turning process, the requirements of the closed loop response are determined, and used to optimize the controller gains. The controller is implemented, and the open and closed loop responses of the simulation and actual structure are compared in relation to the closed loop system requirements.

4.2. Instrumentation and system setup

The actuator system is operated under feedback control with the control software residing on a PC. Data processing is performed using an Indy F3 Digital Signal Processing (DSP) board, with a TMS320C32 microcontroller. Digital to analog conversion is performed by a DL3-A1 Analog

Module which interfaces to the DSP board. The gain of the D/A converter is set to one by the manufacturer. The specifications of the DSP board are given in Table 4.1. The control software is written in a Fast Cyclic Executive (FCE) operating system, designed by Otkunc [57], which runs under MS Windows NT/2000. The program reads the input signals, executes the control law, and outputs the control signal every sampling interval T_s. The sampling frequency, f_s, is set to 7500 [Hz]. The output control signal, in the range of 0 to 10 volts, is received by a Physik Instrumente P-270 high voltage amplifier with a gain K_A of 100 [volt/volt]. The amplifier specifications are listed in Table 4.2. The high voltage signal (0 to +1000 V) is input to the piezostack driving element, as well as the clamping unit piezostacks when necessary. The output capacitive sensor signal is processed by a Physik Instrumente E-509 electronics card, which compares the capacitance to a reference capacitor, and outputs a voltage signal of +/- 5 volts. The input and output signals connect to the D/A converter via a BNC junction box. A schematic of the system setup is given in Figure 4.1.

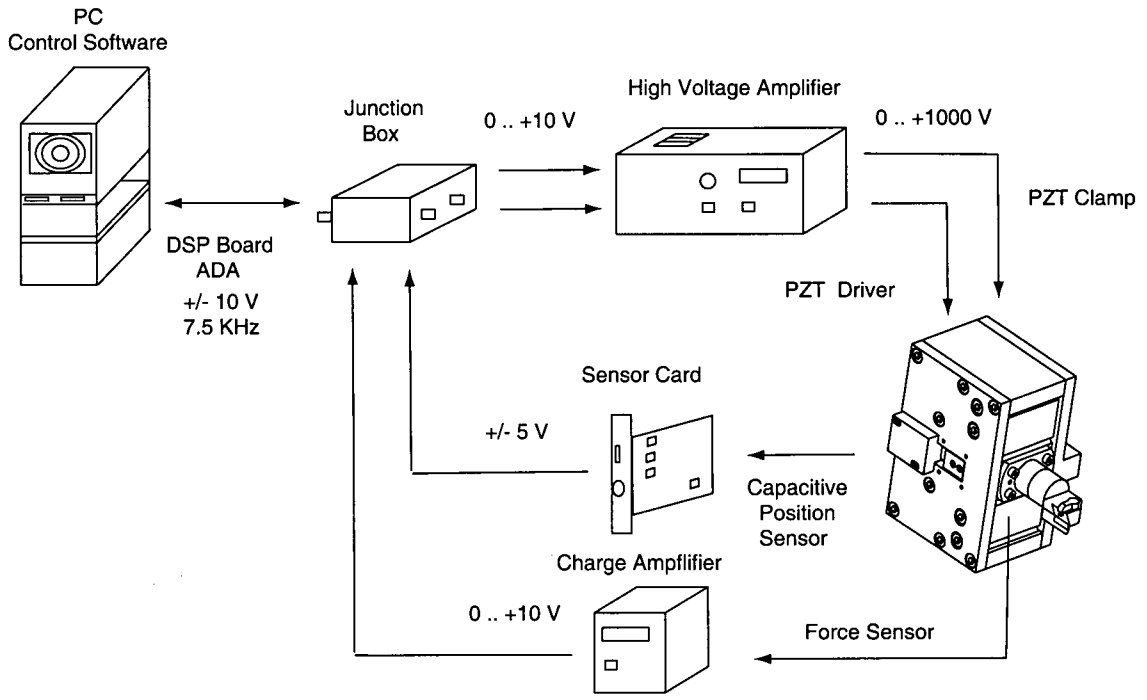

Figure 4.1 : System instrumentation and signal flow.

Processor	Indy F3
Bus configuration	ISA (2K of 16-bit Dual Port RAM)
Analog Input	4 Channels
Analog Output	2 Channels
I/O range	+/- 10 volts

Table 4.1 : Specifications of the Spectrum F3 DSP board.

Output voltage	0 to -1000 V (standard) 0 to +1000 V (optional)
Polarity	switchable
Max. avg. output current	100 mA
Max. peak current	500 mA (<5 msec)
Avg. output power	100 W
Nonlinearity	< 0.5%
Large signal bandwidth	2 Khz
Small signal bandwidth	7 KHz

Table 4.2 : Physik Instrumente P-270 high voltage amplifier specifications.

4.3. Piezoelectric actuator non-linearities

Piezoceramic materials commonly exhibit two types of non-linearity; hysteresis in position for varying input voltage, and position creep over time for a given input voltage. Hysteresis, due to crystalline polarization and molecular friction, is such that the displacement of the actuator is dependent not only on the electric field applied but also whether the actuator was previously operated at a higher or lower voltage. The hysteresis in the system was characterized, and is presented in Figure 4.2. The input voltage was increased from zero to +1000 V (and +500 V), then decreased to zero, and the position at each increment was measured using a laser displacement sensor. The maximum hysteresis is approximately 25%. Figure 4.3 presents the creep over time of the actuator for an input voltage of +150 V, which corresponds to an initial displacement of 5 microns. The actuator creep, due to remanent polarization of the ceramic, shows an exponential

decrease over time. After one minute the displacement increases above 5.9 microns. The relation between displacement and time for a given initial displacement was determined and is given in Equation 4.1, where $x(t)$ [m] is the position at time t [s], and $x(0)$ [m] is the initial displacement.

$$x(t) = x(0) \cdot [1 + 0.109 \cdot t^{0.14}] \quad \text{for } 0 < t < 60s \tag{4.1}$$

The occurrence of these two phenomenon pose a challenge in operating piezoelectric translators in an open loop mode, as the output displacement shows a nonlinear dependence on both input voltage and time. Thus closed loop control is required to accurately position any piezoelectric translator.

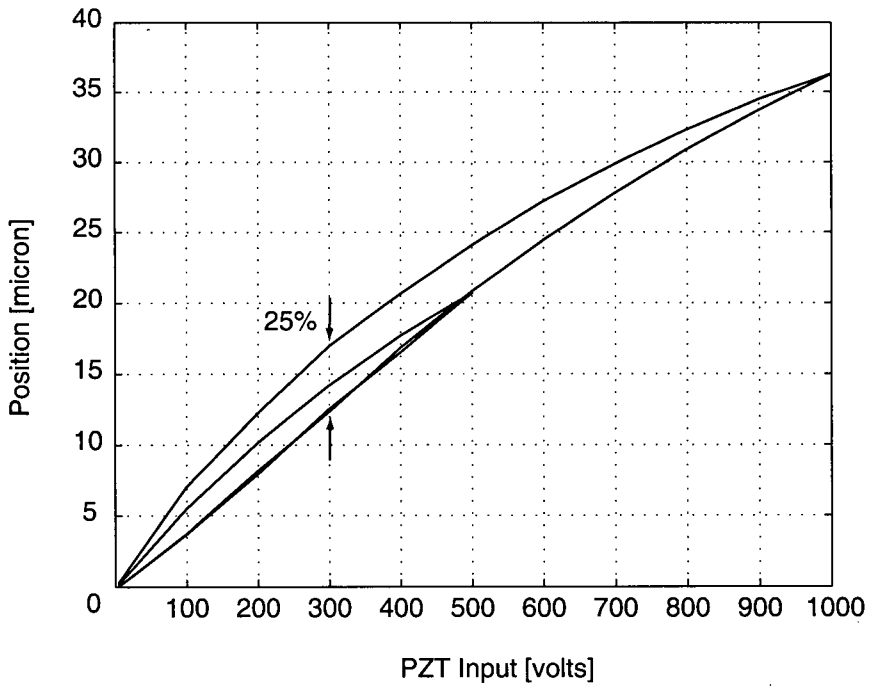

Figure 4.2 : Piezoelectric actuator hysteresis.

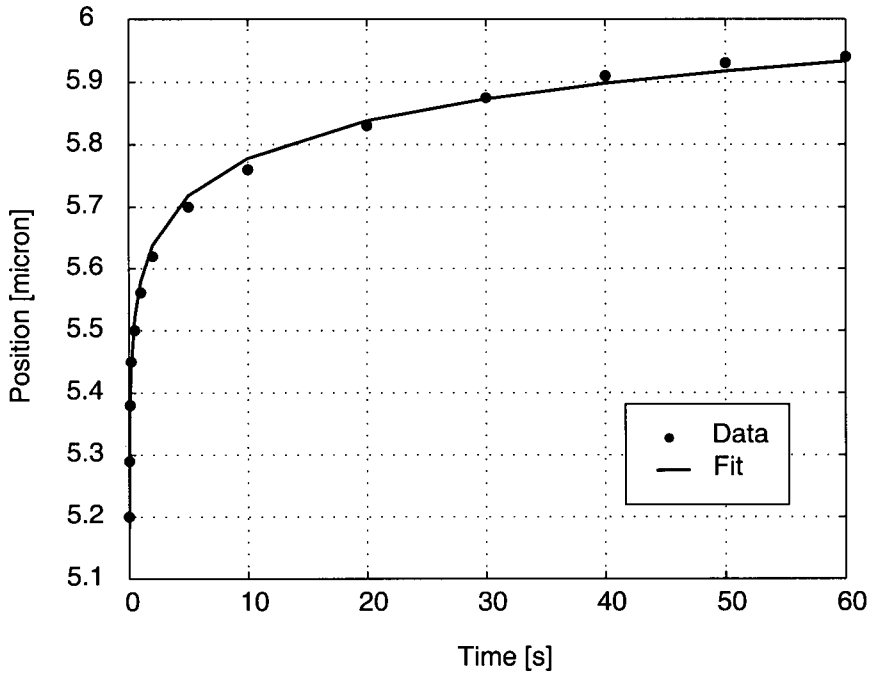

Figure 4.3 : Piezoelectric actuator creep.

4.4. Actuator modal properties

The modal properties of the actuator were determined for each of the three translational degrees of freedom, and for both the clamped and unclamped mode of operation. These properties were identified from the displacement to force direct transfer function obtained experimentally using impact hammer tests in the range of 0-5000 Hz. The structure was excited near the tool tip using an impact hammer instrumented with a force transducer, and the resulting response was measured using an accelerometer. The dominant mode of each transfer function is curve fitted using the MAL-UBC Cutpro modal analysis software, and the properties (natural frequency f, damping C, stiffness K, mass M, and damping ratio ζ) are determined for the given mode. The results are summarized in Table 4.3. The magnitudes G [m/N] of the direct transfer functions in the x, y, and z directions for the unclamped actuator are presented in Figure 4.4. Since the accel-

erations are converted to displacements by dividing by ω^2 at each frequency ω, the magnitude tends toward infinity at low frequencies. The depth of cut in the machining process is affected mainly by the flexibility of the system in the radial direction, as deflection in the feed and tangential directions reflect little deviation in radial position of the tool. The achieved static stiffness in the radial direction is 370 [N/μm], and the natural frequency is 3.2 kHz. The obtained stiffness is lower than the expected value of 473 [N/μm]. The actual stiffness of the Guiding Unit is 20 [N/μm], which agrees well with the predicted value of 23 [N/μm], thus the discrepancy in stiffness is attributed to the manufacturer's quoted value of the piezoelectric translator stiffness. Regardless the stiffness exceeds the design constraint. The clamped mode transfer functions are given in Figure 4.5. Clearly when the clamping units are activated the dominant mode in the radial (x) direction is shifted to a higher frequency of 3.9 kHz, and the static stiffness increases to 626 [N/μm]. As well the rigidity in the y and z directions are noticeably increased when the clamping units are activated.

Mode	Direction	f [Hz]	ζ	M [Kg]	C [Ns/m]	K [N/m]
Unclamped	x	3200	0.027	0.9	985	3.70×10^8
Unclamped	y	1720	0.047	0.54	547	6.30×10^7
Unclamped	z	2000	0.069	0.25	436	3.95×10^7
Clamped	x	3870	0.028	1.059	1442	6.26×10^8
Clamped	y	1790	0.053	0.701	819	8.52×10^7
Clamped	z	2140	0.075	0.42	824	7.18×10^7

Table 4.3 : Identified actuator modal parameters.

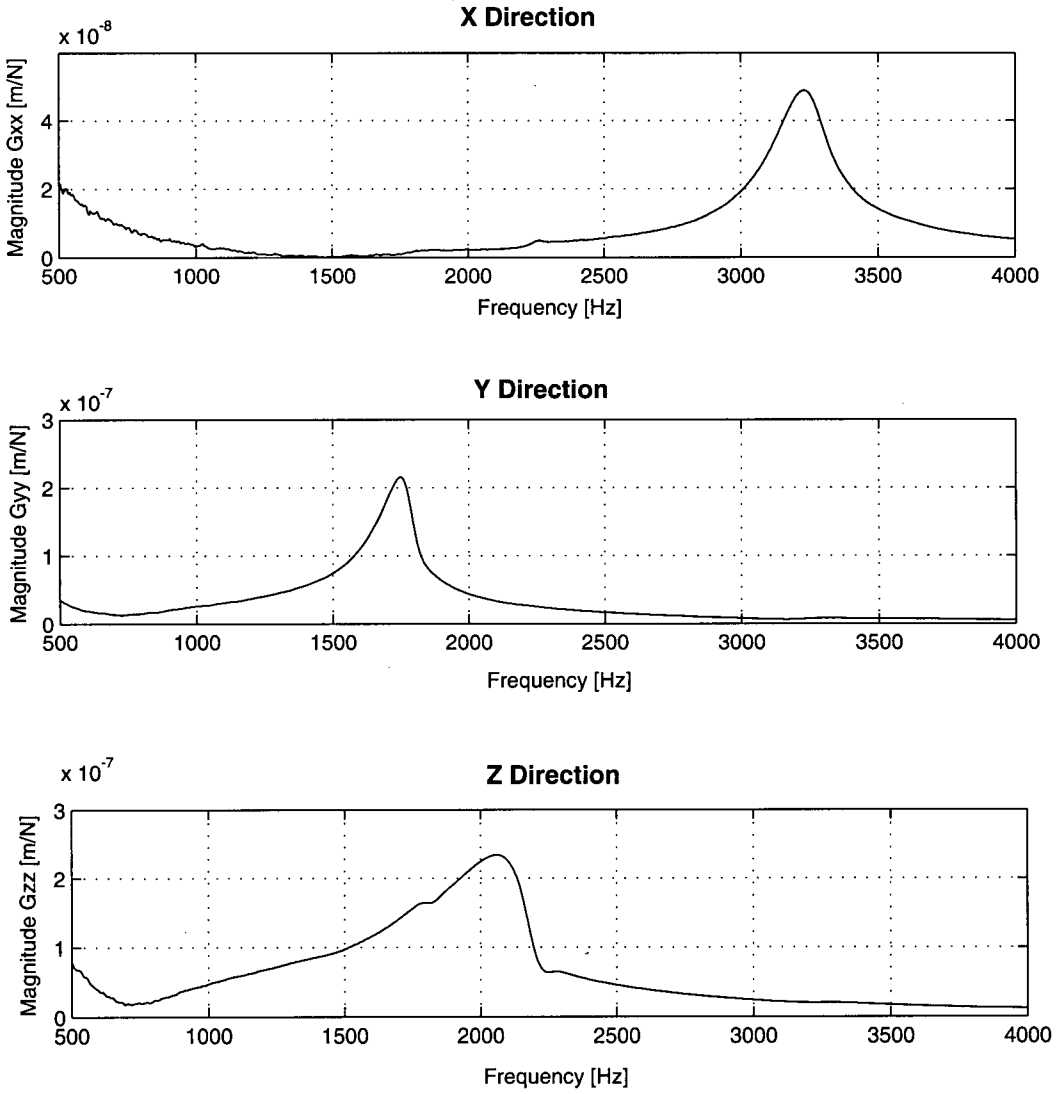

Figure 4.4 : Direct transfer functions for the x, y, and z directions, unclamped mode.

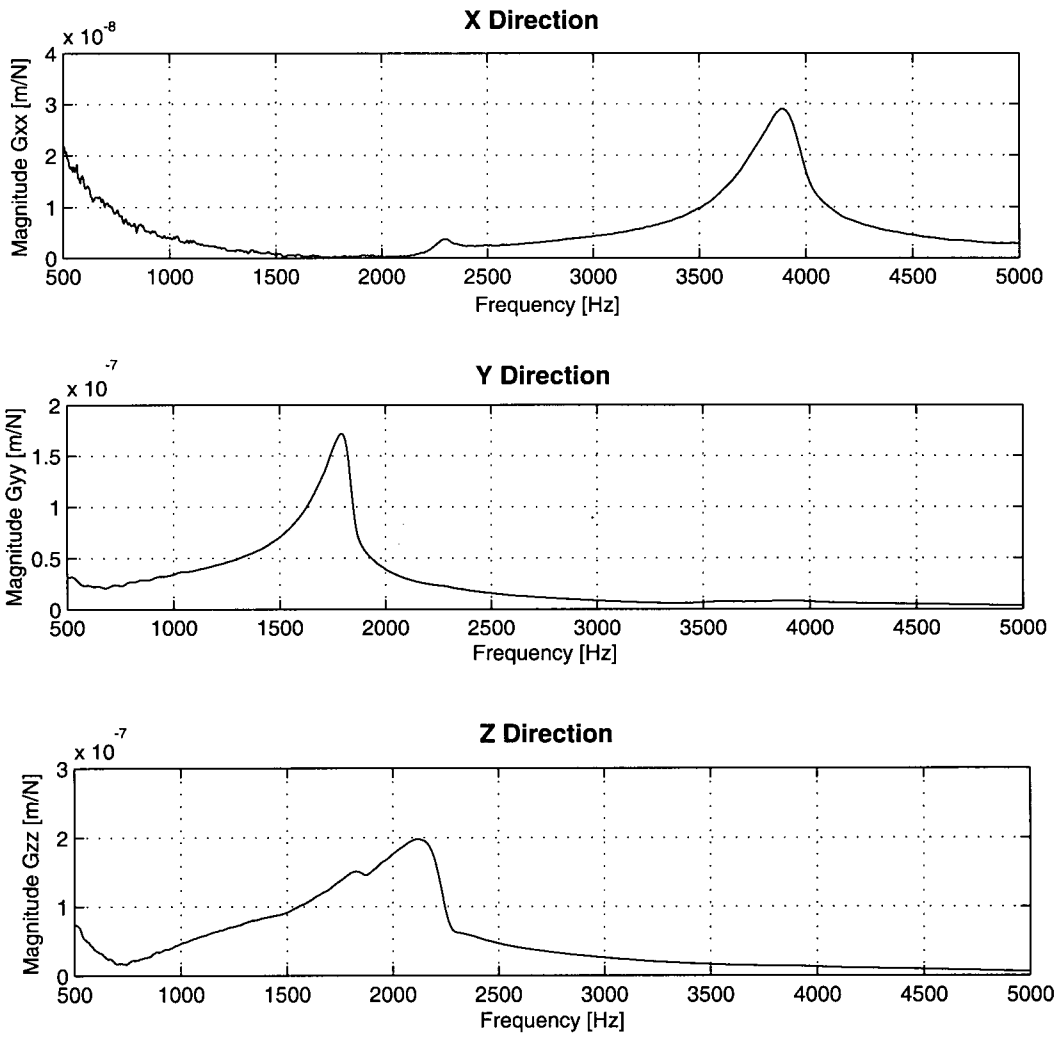

Figure 4.5 : Direct transfer functions for the x, y, and z directions, clamped mode.

4.5. Displacement sensor

The static gain of the capacitive sensor was calibrated using an HP 5517B laser and HP 10706B interferometer with a fundamental optical resolution of 158.2 nm, which is refined to 5 nm using the system electronics. For increments in applied voltage to the piezoelectric actuator the sensor output voltage and laser interferometer position were recorded, shown in Figure 4.6. The initial displacement of the sensor was varied, with the initial output voltage ranging from -9 volts to 1.4 volts (sensor output range is +/- 10 volts). The plots show the sensor is linear over the entire output voltage range of the sensor. The average sensitivity factor is 0.2013 volts/micron, which shows close agreement to the sensor specification of 0.2 volts/micron.

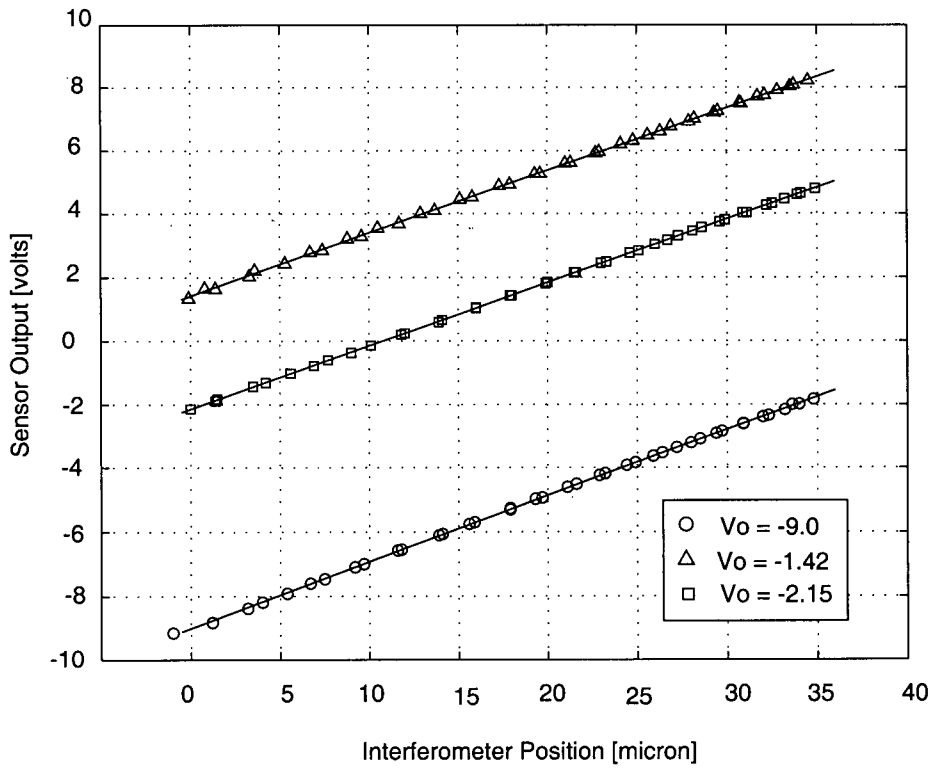

Figure 4.6 : Capacitive displacement sensor calibration.

The Physik Instrumente E-509 capacitive sensor electronics card applies a low pass filter with adjustable bandwidth to the output position signal. In order to avoid aliasing during sampling of the position signal, the sensor bandwidth must be set lower than the Nyquist frequency, f_N. For a sampling frequency of 7500 Hz, the Nyquist frequency is f_N = 3750 Hz, thus the sensor bandwidth is set to the maximum of 3000 Hz. The dynamics of the E-509 capacitive displacement sensor electronics card were identified by comparing the direct transfer function (x-direction) obtained using an accelerometer to measure the response, to the transfer function obtained using the capacitive displacement sensor. Given the pre-determined modal properties in the x-direction (Table 4.3), the sensor dynamics can be solved for by curve fitting the transfer function and assuming a form of the sensor transfer function. A first order filter with a zero and pole is assumed. The measured displacement X_m to actual displacement X transfer function is expressed as Equation 4.2, and the block diagram is shown in Figure 4.7. The bode diagram of the simulated sensor transfer function is given in Figure 4.8. The bandwidth is approximately 2.4 kHz, which is lower than the manufacturer's specification of 3 kHz. The simulated and measured magnitude and phase of the actuator transfer function is shown in Figure 4.9, and the real and imaginary parts of the transfer function are shown in Figure 4.10. The simulated result shows excellent agreement with the measured values. The peak value of the transfer function at the dominant mode (3200 Hz) is approximately 60% of the value obtained from accelerometric data, which agrees with the magnitude of the bode plot in Figure 4.8. The form of the real and imaginary parts of the transfer function clearly show the effect of a higher order system with a zero as they show trends opposite to a typical second order system.

$$G_s(s) = \frac{X_m(s)}{X(s)} = \frac{B_1 s + 1}{B_2 s + 1} = \frac{-0.00004 s + 1}{0.000111 s + 1} \qquad (4.2)$$

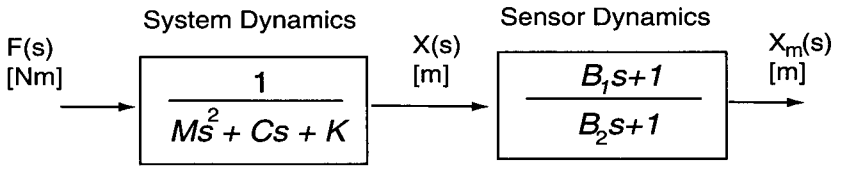

Figure 4.7 : Block diagram of the sensor dynamics.

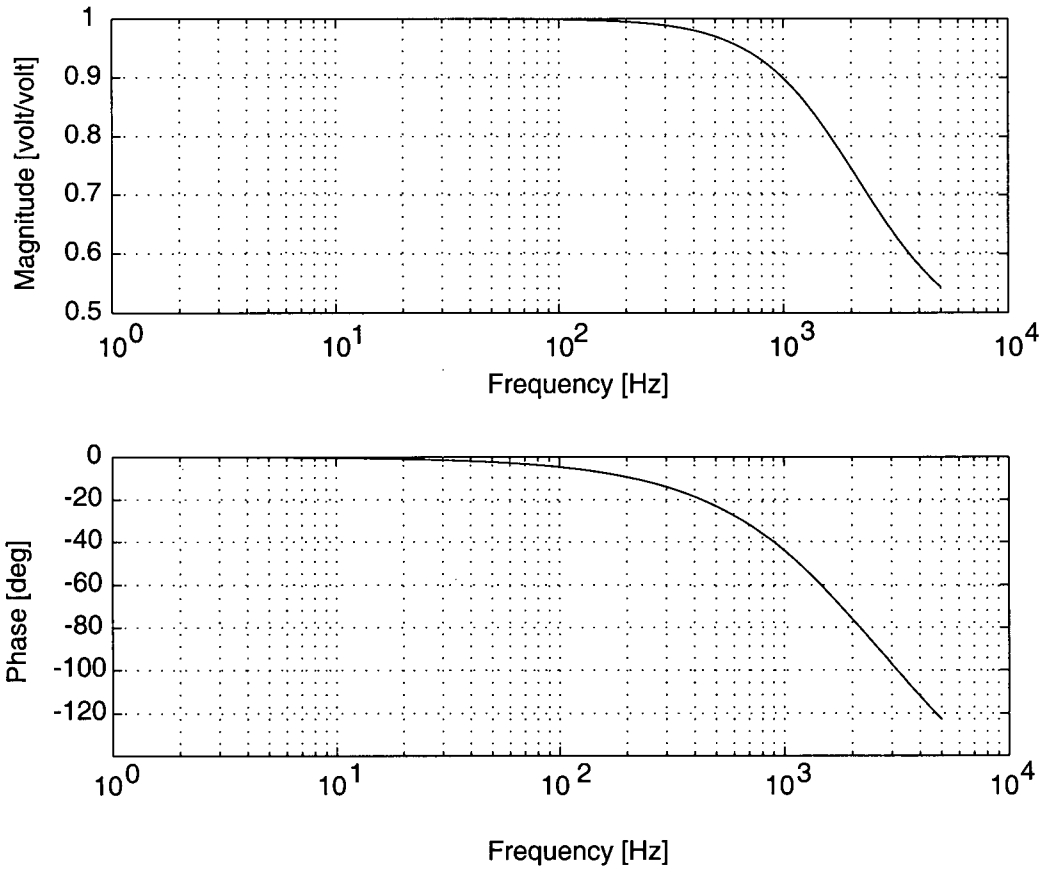

Figure 4.8 : Simulated bode diagram of the sensor dynamics.

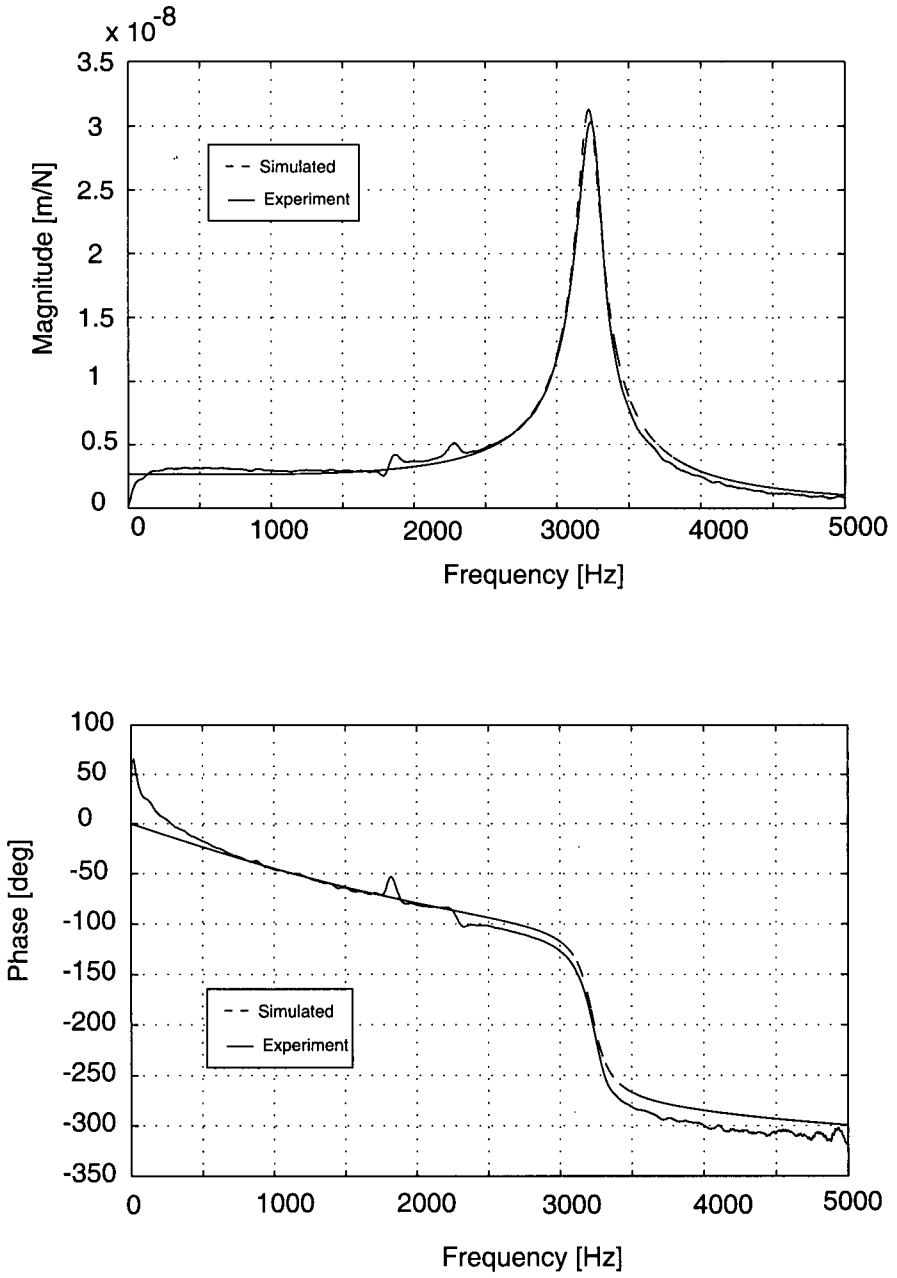

Figure 4.9 : Magnitude and phase of direct transfer function obtained using the displacement sensor.

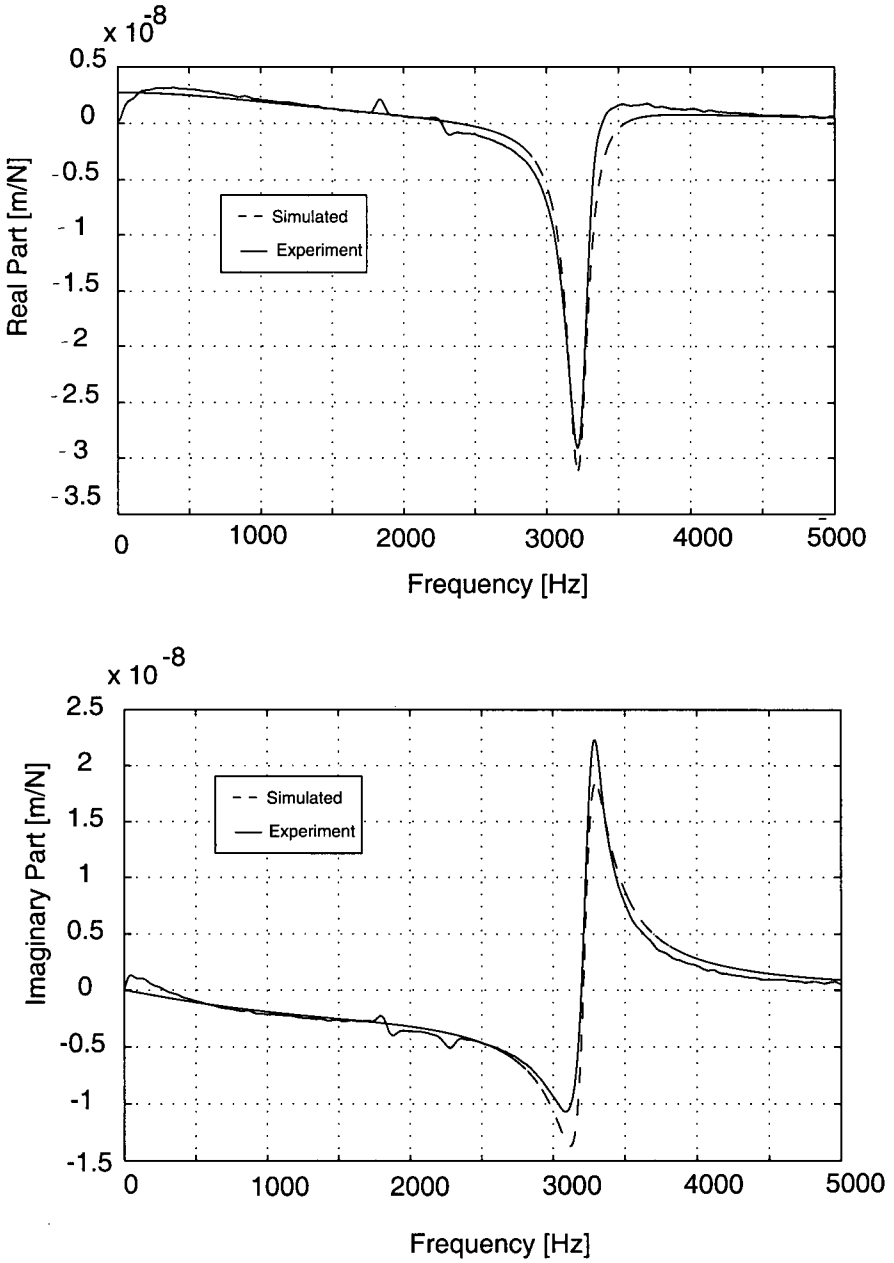

Figure 4.10 : Real and imaginary parts of the transfer function obtained using the displacement sensor.

4.6. Actuator system model

The piezoelectric translator and flexures are modeled as a second order system, and the system model is expressed in Equation 4.3. The effective mass, damping, and stiffness are represented by variables M [Kg], C [Nm/s], and K [N/m], respectively. The displacement and its time derivatives are represented by $x(t)$ [m], $\dot{x}(t)$ [m/s], and $\ddot{x}(t)$ [m/s^2]. The input force to the system is F_i [N], and the force disturbance is F_d [N]. By assuming a constant gain K_F [N/volt] to relate the input voltage to the piezoelectric actuator to the force input to the system, the control signal $u(t)$ [volt] can be introduced as in Equation 4.4 given the amplifier gain K_A [volt/volt]. In Laplace domain the system is described by Equation 4.5, and solving for the displacement yields Equation 4.6. The block diagram of the system is given in Figure 4.11.

$$M\ddot{x}(t) + C\dot{x}(t) + Kx(t) = F_i - F_d \tag{4.3}$$

$$M\ddot{x}(t) + C\dot{x}(t) + Kx(t) = K_A K_F \cdot u(t) - F_d \tag{4.4}$$

$$Ms^2X(s) + CsX(s) + KX(s) = K_A K_F U(s) - F_d(s) \tag{4.5}$$

$$X(s) = \frac{K_A K_F}{Ms^2 + Cs + K} U(s) - \frac{1}{Ms^2 + Cs + K} F_d(s) \tag{4.6}$$

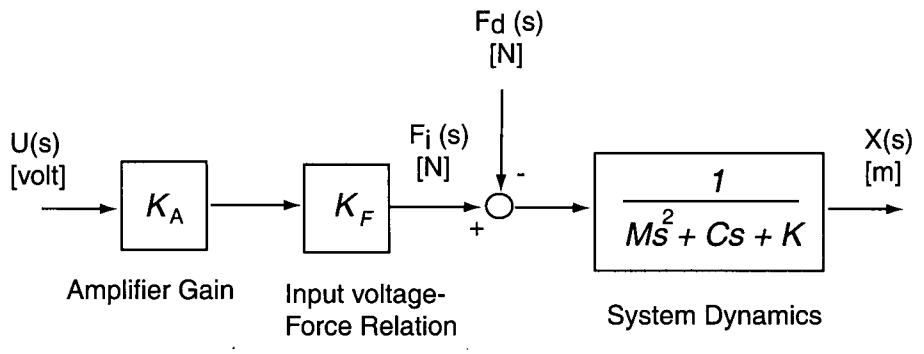

Figure 4.11 : Block diagram of the translator-flexure system.

4.7. Sliding mode controller design

The controller design is based on the methodology proposed by Zhu et al [32] , who developed a sliding mode controller with parameter adaptation to control a piezoelectric actuator for precision turning. The results achieved by Zhu et al showed the sliding mode controller adequately rejected cutting force disturbances and compensated the inherent non-linearities of the piezoelectric translator. Thus the controller design is implemented in this work, and the steps are outlined below.

A sliding surface, S, is designed as in Equation 4.7, where λ [1/s] > 0 is a constant gain which specifies the bandwidth of the response, x [m] is the displacement, and x_d [m] is desired displacement. As the sliding surface contains both the error in displacement and the error in velocity, convergence of the sliding surface to zero ($S \rightarrow 0$) ensures convergence of the system states to the desired values ($x = x_d$ and $\dot{x} = 0$). The actuator is intended for regulation tasks with a fixed position input, thus the derivative of the desired displacement, $\dot{x}_d$, is zero.

$$\begin{aligned} S &= \lambda(x_d - x) + (\dot{x}_d - \dot{x}) \\ &= \lambda(x_d - x) - \dot{x} \end{aligned} \tag{4.7}$$

The time derivative of the sliding surface is expressed as

$$\dot{S} = -(\lambda\dot{x} + \ddot{x}) \tag{4.8}$$

Neglecting the disturbance force included in Equation 4.4, the acceleration $\ddot{x}$ is expressed by Equation 4.9 where $\hat{M}$, $\hat{C}$, and $\hat{K}$ represent the estimated plant parameters.

$$\ddot{x} = \frac{K_A K_F}{\hat{M}} u - \frac{\hat{C}}{\hat{M}}\dot{x} - \frac{\hat{K}}{\hat{M}}x \tag{4.9}$$

Substituting into the derivative of the sliding surface yields

$$\dot{S} = -\left(\lambda\dot{x} + \frac{K_A K_F}{\hat{M}} u - \frac{\hat{C}}{\hat{M}}\dot{x} - \frac{\hat{K}}{\hat{M}}x\right) \tag{4.10}$$

In order to guarantee asymptotic convergence of the sliding surface to zero, the Lyapunov stability theorem is applied. The theorem states the following [55]:

An equilibrium point of a time invariant dynamical system is stable if there exists a continuously differentiable scalar function V(x) such that along the system trajectories the following is satisfied

$$V(x) > 0, \quad V(0) = 0$$
$$\dot{V}(x) = \frac{dV}{dt} = \frac{\partial V}{\partial x} \cdot \frac{\partial x}{\partial t} \leq 0 \tag{4.11}$$

If the condition is a strict inequality then the system is asymptotically stable.

By designing the Lyapunov function to be a function of the sliding surface, satisfying the theorem will ensure convergence of the sliding surface to zero. The Lyapunov function $V(t)$ is chosen to include the sliding surface S, and the error between the disturbance, d [N], and a disturbance observer $\hat{d}$ [N]. A constant gain, ρ >0 [N/m], is included as well. The Lyapunov function is positive definite and continuously differentiable in accordance with the Lyapunov theorem.

$$V(S, (d-\hat{d})) = \frac{1}{2}\left[\hat{M}S^2 + \frac{(d-\hat{d})^2}{\rho}\right] \tag{4.12}$$

The disturbance observer is designed by [59], and given by Equation 4.13. The disturbance observer is an estimate of the sum of all disturbances in the systems, which include the cutting forces, errors in parameter estimates, and unmodeled hysteresis and creep of the piezoceramic actuator. A range of values is applied to the disturbance observer such that $\hat{d} \in [d^-, d^+]$ where d^- and d^+ denote the lower and upper bounds of the disturbance, respectively.

$$\dot{\hat{d}} = \rho S \kappa \tag{4.13}$$

taking the integral yields

$$\hat{d} = \int \rho\kappa S dt = \rho\kappa \int S dt \tag{4.14}$$

where κ is designed to impose limits on the control signal, and is given by

$$\kappa = \begin{cases} 0 & \text{if } \hat{d} \le d^- \text{ and } S \le 0 \\ 0 & \text{if } \hat{d} \ge d^+ \text{ and } S \ge 0 \\ 1 & \text{otherwise} \end{cases} \tag{4.15}$$

In a stable turning process the cutting forces are constant, except for high frequency forces due to chip breaking and frictional forces. For a constant disturbance d the derivative of the Lyapunov function is given by

$$\dot{V} = \frac{\partial V}{\partial S} \cdot \frac{dS}{dt} + \frac{\partial V}{\partial (d - \hat{d})} \cdot \frac{d(d - \hat{d})}{dt}$$

$$\dot{V} = \hat{M} S \dot{S} - \frac{(d - \hat{d})}{\rho} \dot{\hat{d}}$$

Substituting the derivative of the sliding surface (Equation 4.10) and disturbance observer (Equation 4.13) yields Equation 4.16.

$$\begin{aligned} \dot{V} &= -M\lambda S\dot{x} + CS\dot{x} + KSx - SuK_A K_F + Sd - S(d - \hat{d})\kappa \\ \dot{V} &= -\hat{M}\lambda S\dot{x} + \hat{C}S\dot{x} + \hat{K}Sx - SuK_A K_F + S\hat{d} + S(d - \hat{d})(1 - \kappa) \end{aligned} \tag{4.16}$$

According to Equation 4.15, $S(d - \hat{d})(1 - \kappa) \le 0$, thus the derivative of the Lyapunov function can be expressed as

$$\dot{V} \le -\hat{M}\lambda S\dot{x} + \hat{C}S\dot{x} + \hat{K}Sx - SuK_A K_F + S\hat{d} \tag{4.17}$$

By introducing the feedback gain K_s, the following equation will ensure stability since $-K_s S^2 < 0$,

$$-\hat{M}\lambda S\dot{x} + \hat{C}S\dot{x} + \hat{K}Sx - SuK_A K_F + S\hat{d} = -K_s S^2 \tag{4.18}$$

Solving for u yields the control law in Equation 4.19.

$$u = \frac{-\hat{M}\lambda\dot{x} + \hat{C}\dot{x} + \hat{K}x + \hat{d} + K_s S}{K_A K_F} \tag{4.19}$$

Substituting Equation 4.14 for the disturbance estimate yields Equation 4.20.

$$u = \frac{-\hat{M}\lambda\dot{x} + \hat{C}\dot{x} + \hat{K}x + \rho\kappa\int S dt + K_s S}{K_A K_F} \tag{4.20}$$

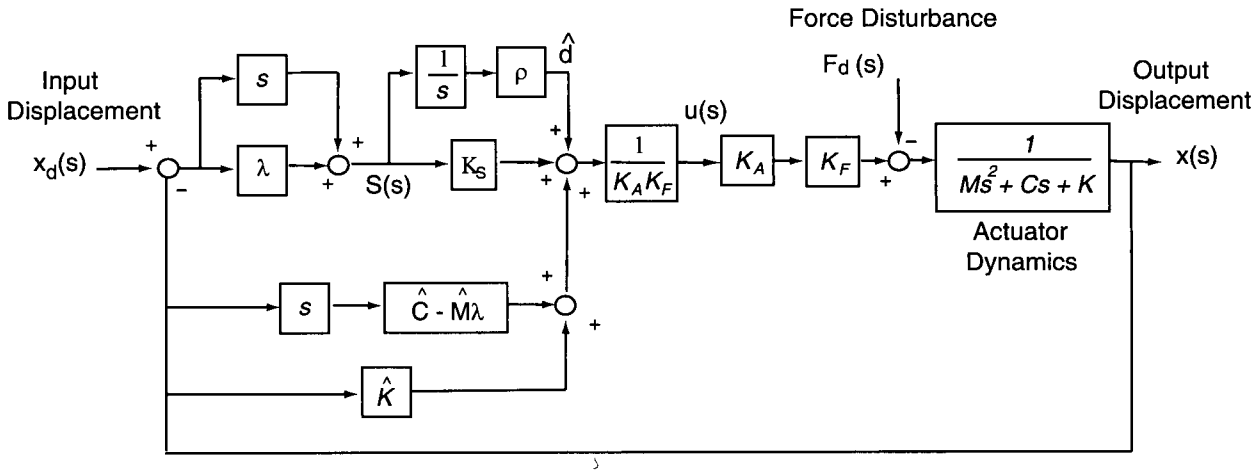

Figure 4.12 : Block diagram of the sliding mode controller with parameter adaptation.

The block diagram of the controller is presented Figure 4.12. The controller consists of error feedback components $K_s S$ and $\rho\kappa\int S dt$, as well as feedback terms $-\hat{M}\lambda\dot{x}$, $\hat{C}\dot{x}$, and $\hat{K}x$. Unlimited bounds are set on the disturbance observer, $\hat{d} \in [-\infty, +\infty]$, such that no limitations are imposed on the controller integral action ($\kappa = 1$ in Equation 4.15). The gain relating the input voltage to the piezoelectric translator to the equivalent force on the system, K_F, is determined by the ratio of the static flexibility K [N/m] to the static gain K_v [volt/m] relating input voltage to displacement at zero frequency. The amplifier gain is assumed constant over the frequency range.

$$K_F = 13.32 \quad [\text{N/volt}]$$
$$K_A = 100 \quad [\text{volt/volt}]$$

The estimated plant parameters determined from the direct transfer function in the radial direction (Table 4.3) are

$$\hat{M} = 0.9 \quad [\text{Kg}]$$
$$\hat{C} = 985 \quad [\text{Ns/m}]$$
$$K = 370x10^6 \quad [\text{N/m}]$$

The constraints on the closed loop response of the system are the rise time and overshoot. The rise time must be such that the cutting tool responds to a step disturbance in the machining process before the next revolution of the part. In this way any form error on the part due to controller response is limited to the first revolution. The worst case of a high cutting speed of 400 m/min and a small part diameter of 25 mm dictates that the rise time be less than 20 msec. The controller must be tuned such that the desired value is not overshot, which would cause grooving on the surface of the part, although completely no overshoot from a critically damped system would result in a slow system response. Thus the maximum overshoot is set to 1%. Through simulation using Matlab/Simulink software the control parameters are tuned to achieve the desired response. The tuned constants used in the controller are:

$$\lambda = 350 \quad [1/\text{s}]$$
$$\rho = 7.0x10^7 \quad [\text{N/m}]$$
$$K_s = 2.3x10^3 \quad [\text{Ns/m}]$$

A low pass filter is applied to the velocity computation to reduce the effect of noise from the capacitive sensor. In discrete time domain the velocity is computed from the displacement as in Equation 4.21, where T_s [s] is the sampling interval, and α is set to 0.5. The control law is implemented in digital form in the control software. For integration the sliding surface is approximated as a constant over the sampling interval in discrete time domain as given in Equation 4.22.

$$\dot{x}(k) = \alpha\dot{x}(k-1) + \frac{(1-\alpha)}{T_s}[x(k) - x(k-1)] \tag{4.21}$$

$$\int Sdt(k) = \int Sdt(k-1) + S(k)T_s \tag{4.22}$$

4.8. System response

The measured and simulated open loop response of the system for a step control input u of 0.5 volts is presented in Figure 4.13. The simulated response shows an offset in the static gain of 5%, and much less damping compared to the actual response. This may be explained by the assumption of a static gain relating input voltage to input force. In the actual system the dynamics of the input voltage to displacement transfer function may not simply be a ratio of the input force to displacement transfer function. As well actuator creep is such that the final position changes over time and is not fixed as with the simulation. The rise time of the open loop actuator is 0.4 ms, and the settling time is 4 ms.

The closed loop response of the actuator and simulation is presented Figure 4.14 for the sliding mode controller parameters listed in section 4.7. The response is the result of a unit step displacement input of 1 micron. Clearly the desired response is achieved, as the final value is 1 micron and the oscillations and creep associated with the uncontrolled system are eliminated. The actuator rise time is 10 ms, and the overshoot is less than 1%. The steady state error is 0.010 micron, due to sensor noise. The simulated response shows excellent agreement with the actual response, despite the discrepancies in the simulated open loop system. The rise time of the controlled system is twenty five times that of the open loop system, thus the controller significantly slows the response such that the effect of unmodeled dynamics in the simulation is negligible.

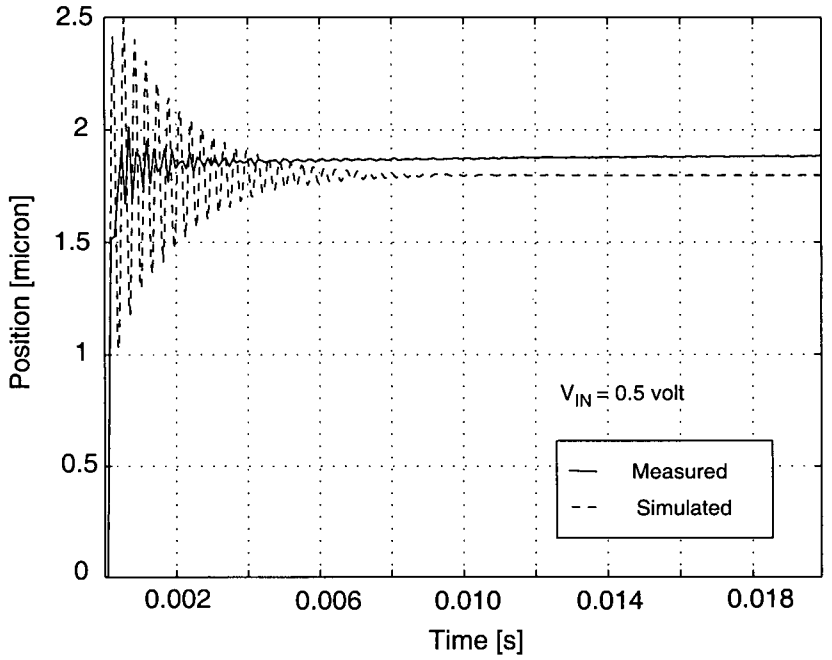

Figure 4.13 : Open loop System response to a step voltage input.

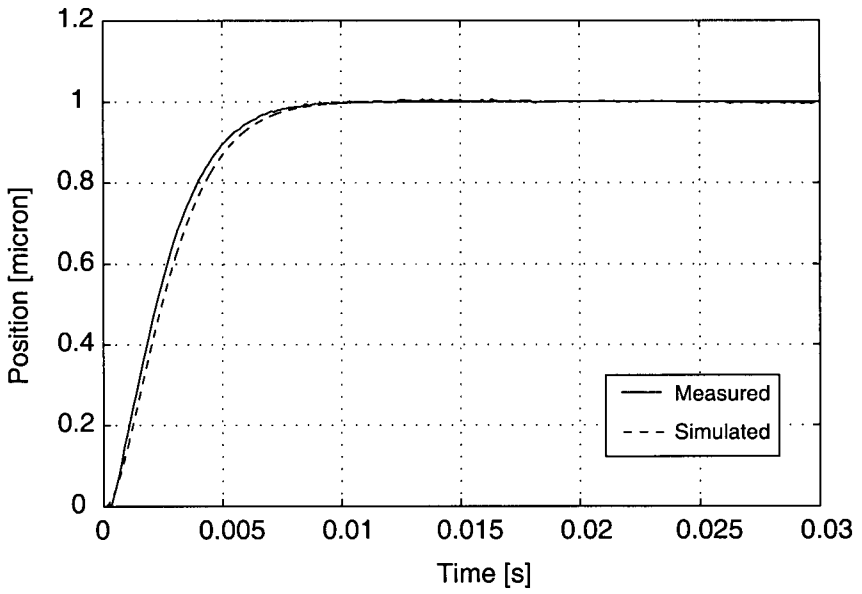

Figure 4.14 : Closed loop system response to a unit displacement step input.

4.9. SMC and feedforward force control

By measuring the radial cutting force using the integrated force sensor arrangement (section 3.5.1) a feedforward force control scheme can be investigated. The block diagram of the feedforward controller is given in Figure 4.15. The force sensor charge signal is processed by a charge amplifier, which outputs a voltage V_f proportional to the measured force. Using the calibration factor of the sensors, K_{FS}, the measured force is obtained. The feedforward transfer function G_{ff} is simply a static gain designed to cancel the force disturbance F_d [60], thus $G_{ff} = \frac{1}{K_A K_F}$. In this way corrective action by the controller is taken before the process is influenced by the force disturbance. Implemented in discrete time domain the measured force $F_m(k)$ is filtered to remove high frequency components as given by Equation 4.23, where α_f is set to 0.8.

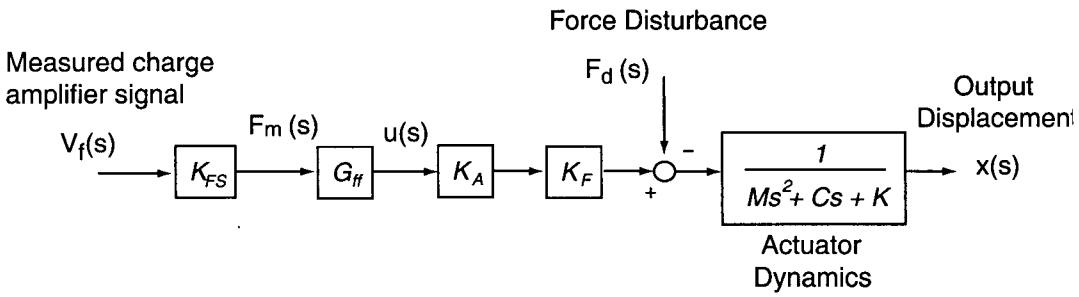

Figure 4.15 : Block diagram of the feedforward force controller.

$$F_m(k) = \alpha_f F_m(k-1) + (1-\alpha_f)F_m(k) \tag{4.23}$$

Since no position feedback is included this controller will only compensate the tool deflection due to radial cutting forces. Position will be affected by hysteresis, creep, variation in the force sensor calibration, and any errors in the transfer function G_{ff}. The feedforward force control can be combined with the sliding mode controller designed in section 4.7 to allow position feedback control. In this case the measured disturbance force F_m is included in the system model

as an approximation of the actual force disturbance F_d as represented in Equation 4.4, and the acceleration of the tool is expressed by Equation 4.24.

$$\ddot{x} = \frac{K_A K_F}{\hat{M}} u - \frac{\hat{C}}{\hat{M}} \dot{x} - \frac{\hat{K}}{\hat{M}} x - \frac{F_m}{\hat{M}} \tag{4.24}$$

Substituting Equation 4.24 into the derivative of the sliding surface yields

$$\dot{S} = -\left(\lambda \dot{x} + \frac{K_A K_F}{\hat{M}} u - \frac{\hat{C}}{\hat{M}} \dot{x} - \frac{\hat{K}}{\hat{M}} x - \frac{F_m}{\hat{M}} \right) \tag{4.25}$$

Using the Lyapunov function (Equation 4.12) and following the steps outlined in section 4.7 the control law given by Equation 4.26 is obtained. The block diagram of the controller is presented in Figure 4.16.

$$u = \frac{-\hat{M}\lambda \dot{x} + \hat{C}\dot{x} + \hat{K}x + \rho\kappa \int S dt + K_s S + F_m}{K_A K_F} \tag{4.26}$$

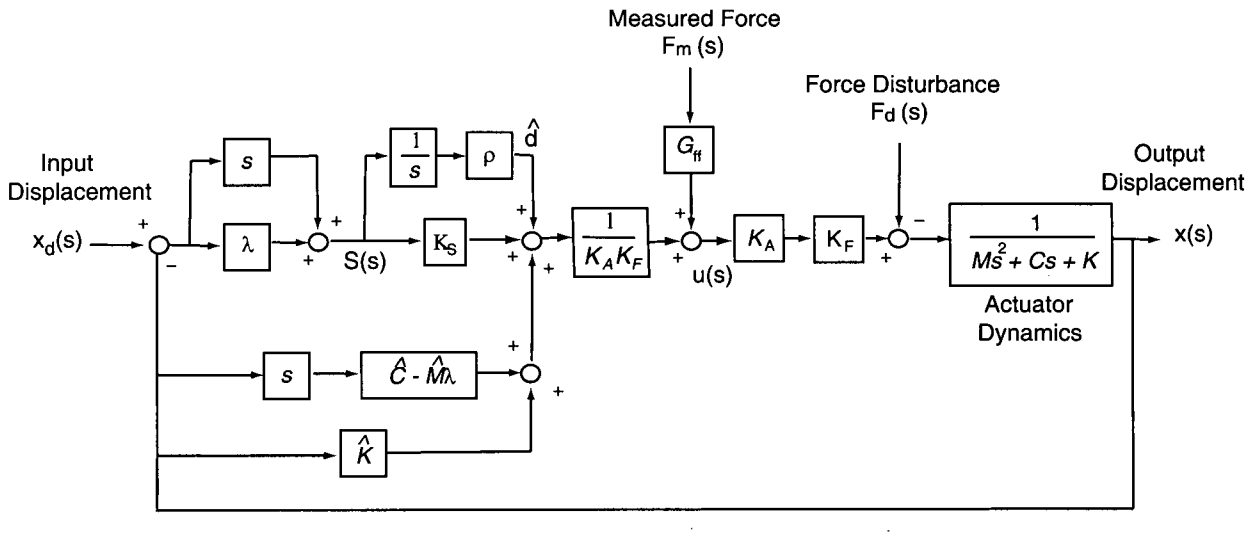

Figure 4.16 : Block diagram of sliding mode controller with feedforward force control.

4.10. Summary

In this chapter the important actuator system properties were identified. The instrumentation used for operation of the actuator was presented, as well the dynamics of the sensor electronics card were discussed. The piezoelectric actuator exhibited two types of non-linearity; hysteresis and creep. The hysteresis was as high as 25%, and creep showed exponential decrease over time. Both phenomenon make it necessary to operate the actuator under closed loop position control. The modal properties of the structure were identified, in both the unclamped and clamped mode. All natural modes are above 1000 Hz. In the radial (x) direction the unclamped properties of the dominant mode are a natural frequency of 3200 Hz and a damping ratio of 2.7%. Using the obtained mass (0.9 kg), stiffness (3.7e8 N/m), and damping (985 Ns/m) the output displacement to input force transfer function was identified. Activating the Clamping Units showed a signification increase in stiffness for each direction.

Combined with a static gain representing output force to input PZT voltage and the amplifier gain, the x-direction transfer function was used to model the actuator displacement given an input control signal. A sliding mode control law was developed with three control parameters, tuned through simulation and experiment. Simulation results for the actuator model showed less damping compared with the experimental values, as well as the unmodeled PZT creep. The simulated control response showed excellent agreement with the actual response. The system performance for a step input was a rise time of 10 ms, and 1% overshoot. Finally feedforward force control was added to the sliding mode controller to compensate the cutting force disturbance during machining before the tool position is affected.

Chapter 5

Experimental Results

5.1. Introduction

The performance of the piezoelectric actuator was evaluated by performing cutting test experiments on conventional machine tools. This chapter presents the results of precision turning experiments performed at the UBC Manufacturing Automation Laboratory. Of prime interest is the achievable positioning accuracy of the actuator, which is characterized by examination of the feedback position signal and the part dimensions. The use of the actuator for micro profiling of shafts is presented, and compared to a conventional machine. An investigation of the achievable surface finish in precision turning of both mild and hardened steels is included in order to determine the deviation from an ideal turned surface. The actuator was installed and operated at two industrial sites; Pratt & Whitney Canada and Caterpillar Inc. The purpose was to determine the feasibility of the actuator in an industrial setting, and the achievable level of part tolerances (diameter, surface roughness) given a practical amount of tool wear. These results are presented, and discussed with respect to the specific industrial application.

5.2. Experimental setup

The cutting experiments were performed on a Hardinge Superslant GN6T two-axis CNC horizontal turning centre in the Manufacturing Automation Laboratory at UBC. The setup of the actuator on the turning centre is presented in Figure 5.1. The toolholder used was a Komet MVJNL16 left handed toolholder, which accommodates 35 degree diamond shaped inserts suitable for finishing. The back rake angle is -9 degrees, the side rake -5 degrees, and the lead angle

is 3 degrees. Two types inserts were used, depending on the application. For low hardness materials coated carbide inserts were used, and for high hardness material cubic boron nitride (CBN) inserts were used. The properties of each insert are listed in Table 5.1. Two workpiece material types were tested, AISI 4340 and AISI 4320 steel, the former being a medium hardness steel (35-40 HRC) and the latter being a high hardness steel (58-62 HRC). The composition and selected properties of each are given in Table 5.2. For tests using carbide inserts CIMPERIAL 1070 cutting fluid with 5% dilution was used to reduce tool wear by removing heat from the cutting zone.

Supplier	Valenite	Sandvik
ISO Designation	VNMG 16 04 04 -1W SV325	VBMW 16 04 04 S01020 CB20
No. Sides	2	1
Chipbreaker	Yes	None
Chamfer	None	0.1mm x 20deg
Material	Carbide	low content CBN w/ TiN
Coating	Al2O3, TiC, TiN	None

Table 5.1 : Inserts used for the cutting tests.

Steel Grade	AISI 4340	AISI 4320
Composition (Weight%)	0.80 Cr, 1.8 Ni, 0.25 Mo, 0.38/0.43C	0.35/0.65 Cr, 1.55/2.0 Ni, 0.2/0.3 Mo, 0.4/0.7 Mn, 0.17/0.23 C
Treatment	Heat Treated	Carburized (0.79 mm case depth)
Hardness	35-40 HRC	58-62 HRC
α–γ Transition temperature	723-775 C	723-825 C
Diameter	75 mm	70 mm
Length	50 mm	150 mm
Supplier	Pratt & Whitney Canada	Timken Research

Table 5.2 : Workpiece material specifications.

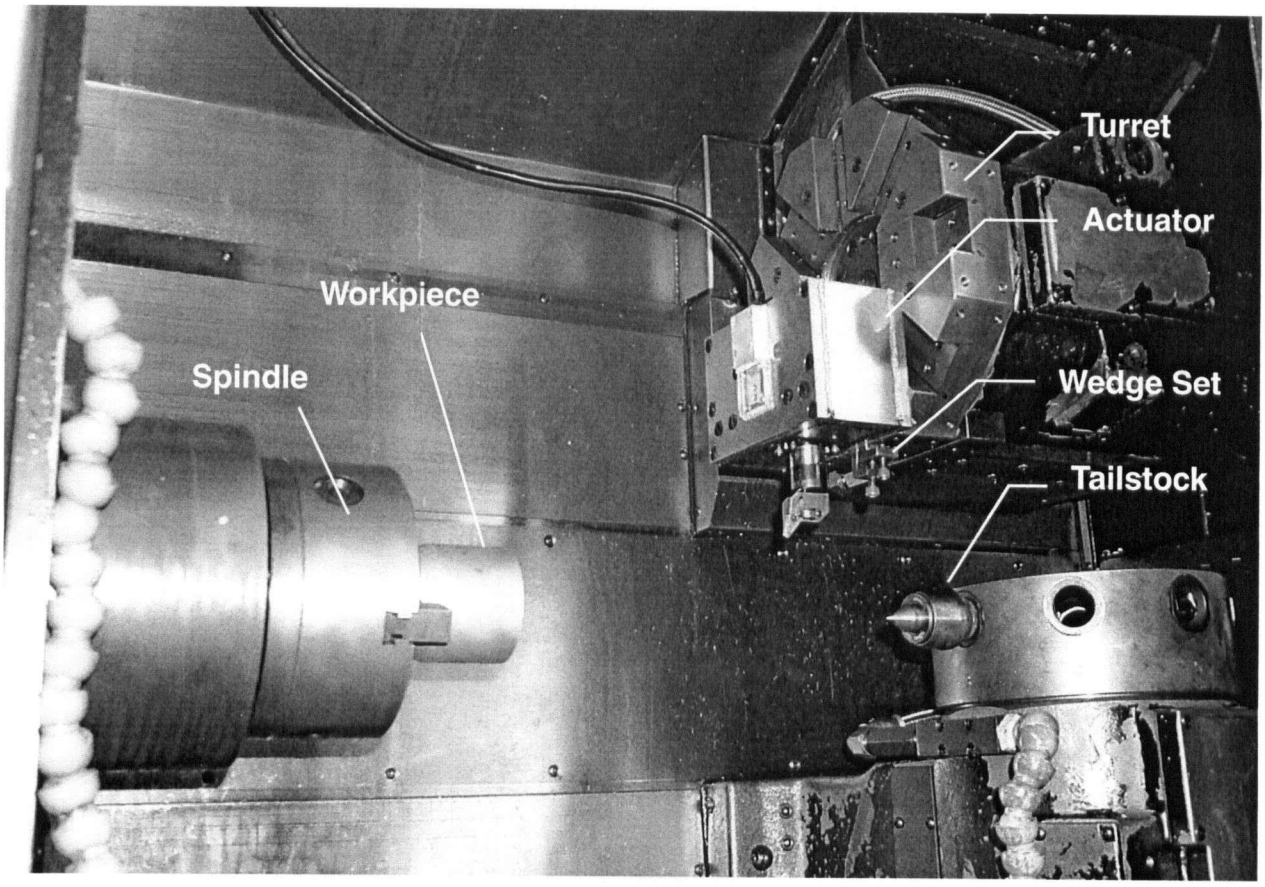

Figure 5.1 : Experimental setup on the Hardinge lathe at MAL-UBC.

5.3. Position control

The controller performance during cutting was investigated by considering the position sensor signal. Figure 5.2 presents the tool position during the cutting process for both the open loop and controlled cases at a 0.1 mm depth of cut. Included is the radial cutting force measured using the integrated force sensors discussed in section 3.5.1, as well as the control signal input to the amplifier. The results are for the 4340 steel and carbide insert, at 125 m/min cutting speed and 0.05 mm/rev feed rate. In the uncontrolled case the tool deflects 0.07 microns when the average cutting force of 24 N is applied. This corresponds to a stiffness of 343 N/micron, which shows

close agreement to the identified radial stiffness of 370 N/micron (Table 4.3). Including the actuator creep and sensor noise the total position error is approximately 0.1 microns such that the effective stiffness is 240 N/micron. Under control the stiffness is increased to 686 N/micron, as the position is held to within 0.035 microns. For the case of precision finishing at a 5 micron depth of cut, the average cutting force measured using the integrated force sensors is 6 N. The position is held to within 0.020 microns as shown in Figure 5.3. The corresponding stiffness is 300 N/micron, clearly limited by the sensor noise. With the machine on and spindle rotating and no cutting, the base noise in the sensor signal is 0.010 microns, and the uncertainty in the achieved position control is roughly twice that value. The results show that for both semi-finish (0.1 mm) and finish (0.005 mm) machining the actuator has low static deformation in the radial direction, and that the controlled tool position is held to less than 0.1 microns given in the design constraints (Chapter 3).

It is clear that the inherent non-linearities of the piezoelectric translator, namely the hysteresis and creep, as well as the actuator deflection under cutting force disturbance are compensated for by the sliding mode controller. The effects of creep and force disturbances can be clearly seen in the input control signals given in Figures 5.2 and 5.3. Considering the positioning resolution of conventional machines can range from 5 to 20 microns, the piezoelectric actuator system augments the resolution up to 1000 times for precision finishing operations. The level of achieved resolution is such that the system positioning is on the level of high precision machines, although only within the 35 micron stroke of the actuator.

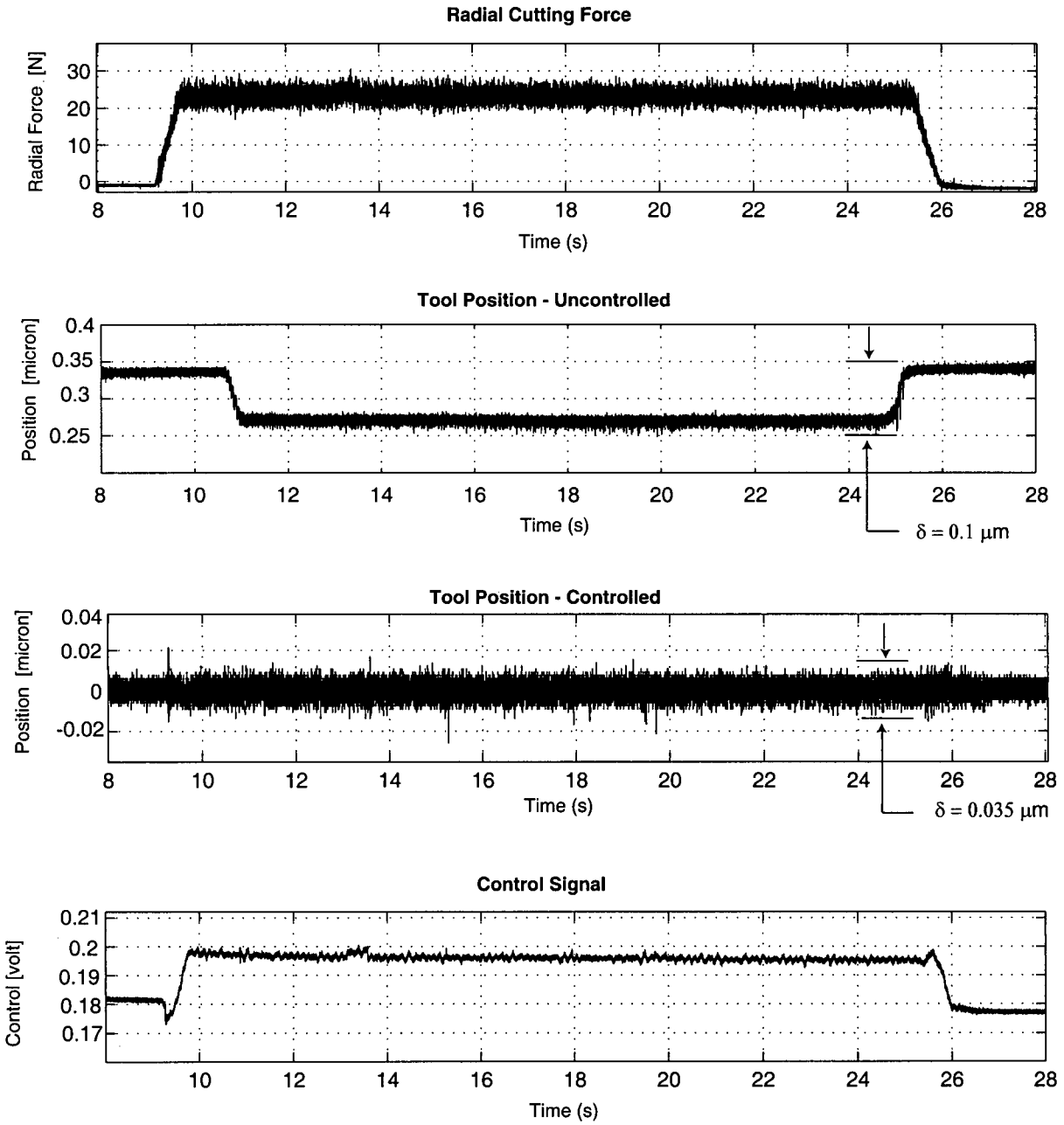

Figure 5.2 : Radial cutting force and tool positioning for a 0.1 mm depth of cut.

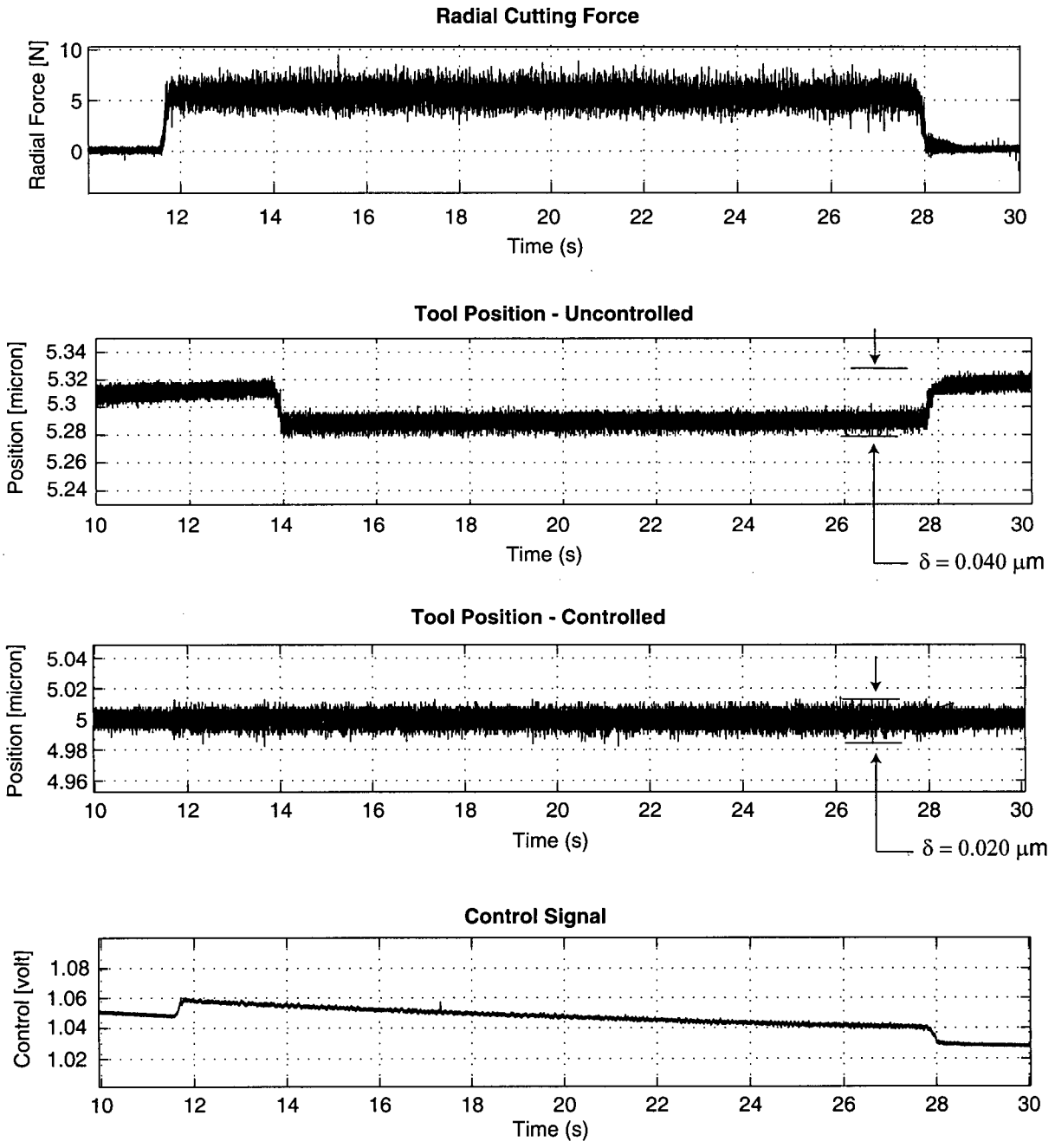

Figure 5.3 : Radial cutting force and tool positioning for a 0.005 mm depth of cut.

Figure 5.4 presents the tool position during machining at 0.1 mm depth of cut for the feedforward force controller alone as well as combined with the sliding mode controller, as outlined in section 4.9. Using the simple feedforward force controller the disturbance due to the radial cutting is rejected, although there is a slight overshoot indicating small errors in the force sensor calibration as well as the feedforward transfer function G_{ff}. When combined with the sliding mode controller the position is controlled to the reference value without offset. The achieved resolution remains limited by the sensor noise, thus the addition of the feedforward force controller shows no improvement in the controller performance. As two additional force signals are sampled in each control interval, the sampling frequency must be decreased to guarantee all computations are performed within the sampling period. Based on this drawback, and the comparable positioning resolution, the sliding mode controller alone is used for position control.

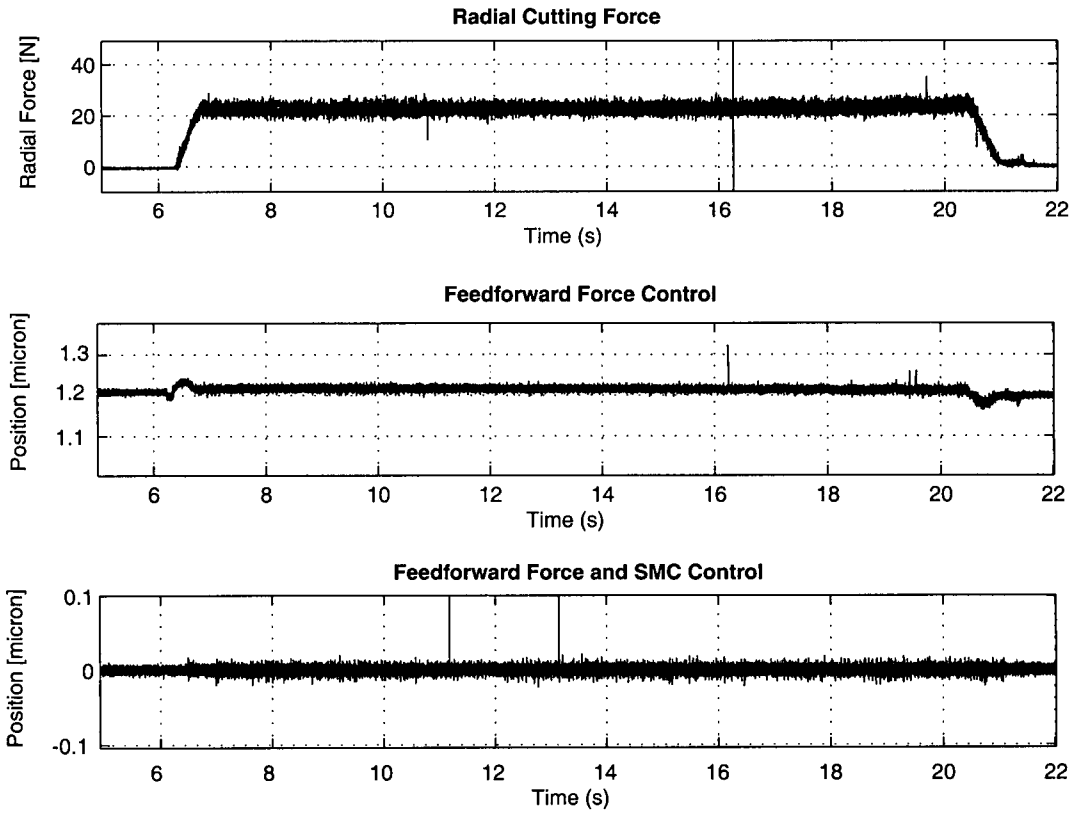

Figure 5.4 : Position control using feedforward force compensation for a 0.1 mm depth of cut.

5.4. Micro profiling

Although the position feedback is controlled to less than 0.025 microns for precision finishing, this alone provides no information as to the quality of the machined part. Since only the radial direction is controlled, the actuator and tool are subject to static deflection in the feed and tangential directions. As well no compensation is provided for the static and thermal deflection of the machine tool, the control resolution of the CNC x-axis, or the alignment of the z-axis. Thus for a given command input to the actuator, the actual change in dimensions reflected on the part is of interest. Experiments were performed to investigate the achievable micro profiles in hard turning of 4320 steel (58-62 HRC), these included step, taper, and convex profiles. The command input to the controller was incremented in each sampling interval to achieve the desired input profile. The cutting conditions for all tests are 125 m/min cutting speed, and 0.05 mm/rev feed rate. The insert used was the chamfered CBN tool, and tests were performed without cutting fluid to avoid fracture of the CBN material due to thermal shock.

The surface profiles were measured with a Mitutoyo stylus type surface analyzer. The achieved profiles for a 5 micron and 1 micron step change are presented in Figure 5.5. The profile shown is the unfiltered profile, which contains both the roughness and waviness components of the profile. For both the 5 micron and 1 micron step changes in command position, the profile reflected on the surface of the workpiece shows excellent agreement. Due to the roughness and waviness of the surface it is difficult to determine the error between the desired and achieved change in position, a value of 0.1 microns is estimated. For comparison the same step change commands were given to the CNC of the machine with standard tooling, the obtained surface profile is shown in Figure 5.6 for a 5 micron and 1 micron step change. The resulting error in tool positioning by the feed drive is approximately 3 microns. Although it is considered a precision turning machine, clearly it alone cannot deliver submicron positioning. As well the start of the feed drive motion in the radial direction is jerky and causes grooving.

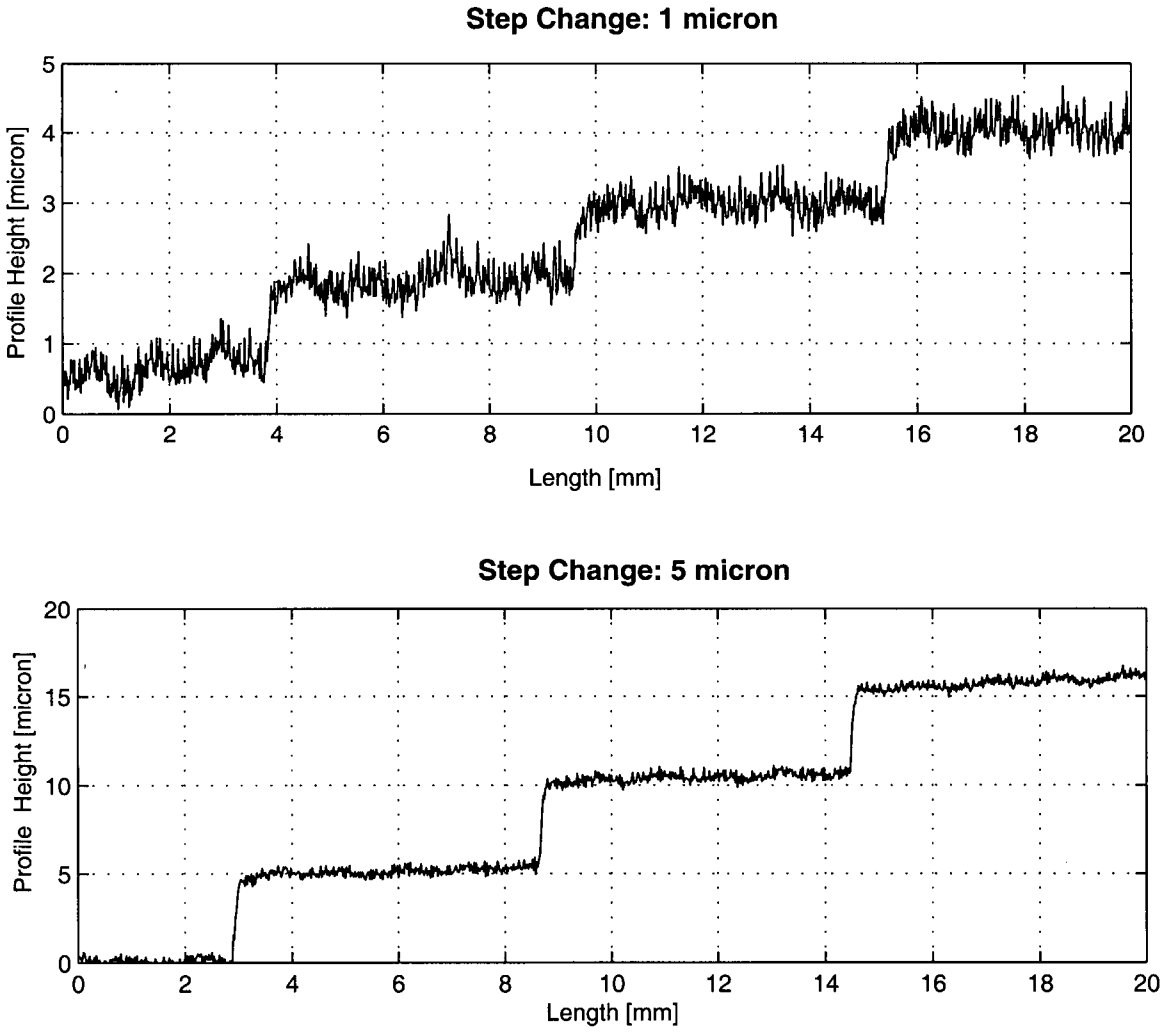

Figure 5.5 : Step change in depth of cut, actuator control.

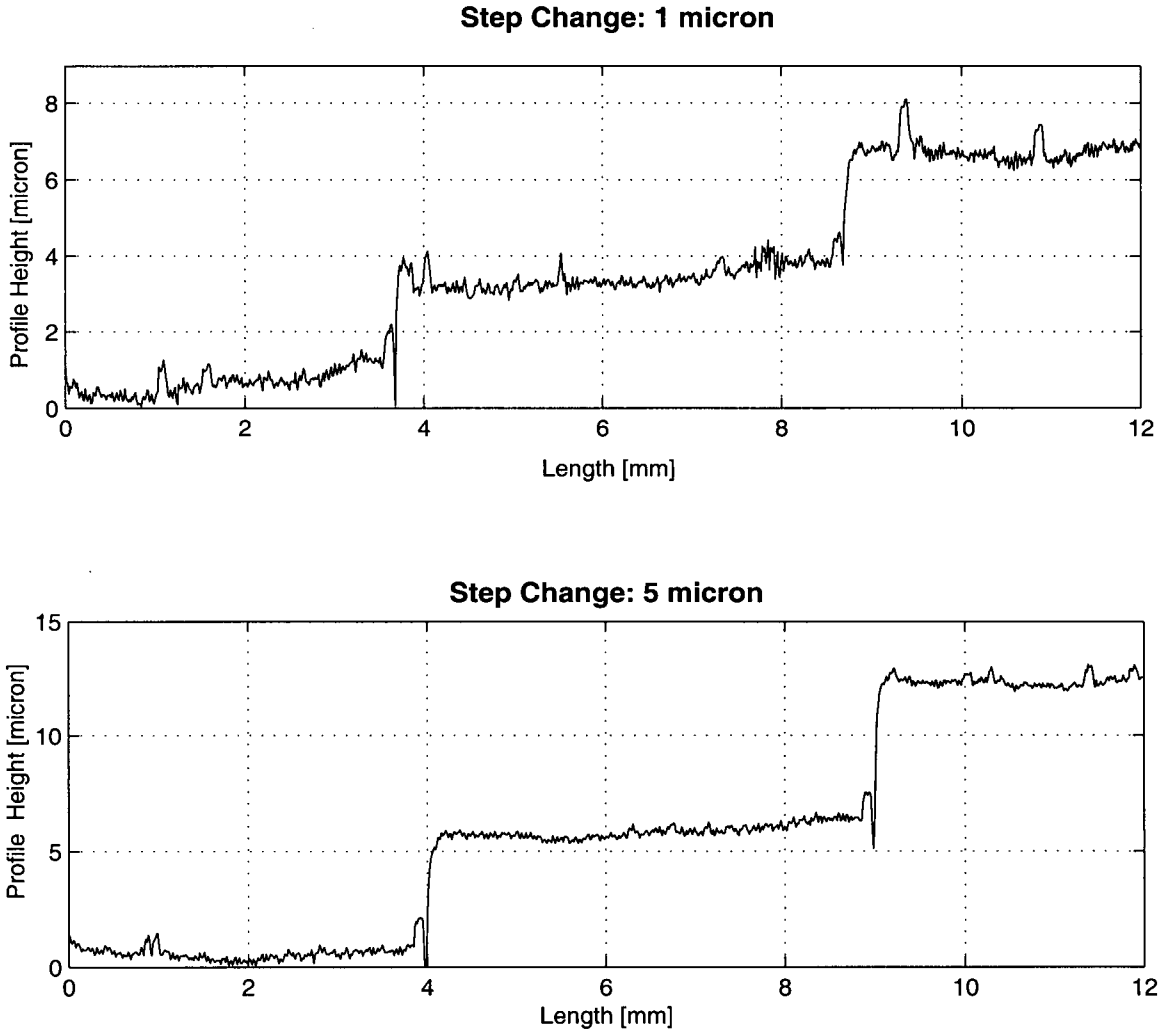

Figure 5.6 : Step change in depth of cut, machine CNC control.

The use of the actuator for dynamically varying the depth of cut is investigated as well. Although the sliding mode controller has been designed assuming constant input command, the magnitude of the commanded displacement input change at each sampling interval is small, such that tracking errors are negligible. The achievable micro profile in hard machining a fine taper is presented in Figure 5.7 for precision turning using both the piezoelectric actuator system and the machine CNC feed drive control. The desired taper height is 10 microns, with a length of 10 mm. Under actuator control the profile is smooth and the desired taper height is achieved. Using the linear interpolation of the CNC controller the profile is jagged with a three micron error in height. Although the manufacturer's specification for control resolution is +/- 0.25 microns, clearly the effects of the feed drive friction and backlash are reflected on the part profile. By allowing such a smooth change in tool position over time the actuator may be suitable for fine compensation of thermal growth in machine tools, given a known deviation in part diametrical tolerance as a function of machining time. For precision bearing design a micro convex profile can be applied to the bearing surface to reduce edge pressures. Figure 5.8 presents the machined surface profiles for convex and concave profiling of the hardened steel, in which the desired profile height is 10 microns. The measured profiles show close agreement with the input command. It should be noted that no compensation was provided for the tool nose radius, thus cutting took place at varying locations along the cutting edge for the circular path such that the profile differs slightly from a true convex or concave shape. Including the surface waviness and roughness the desired trajectory is followed within 0.2 microns. The cutting conditions for both the linear and circular profiling were 125 m/min and 0.05 mm/rev feed rate, using CBN tooling.

From the achieved part micro profiles it is evident that the positioning accuracy of a conventional machine can be significantly improved when the piezoelectric actuator system is incorporated. As well it has been shown that the commanded controller input is reflected as an equivalent change in depth of cut during finish machining. Thus the design constraint of sub-micron positioning resolution is satisfied.

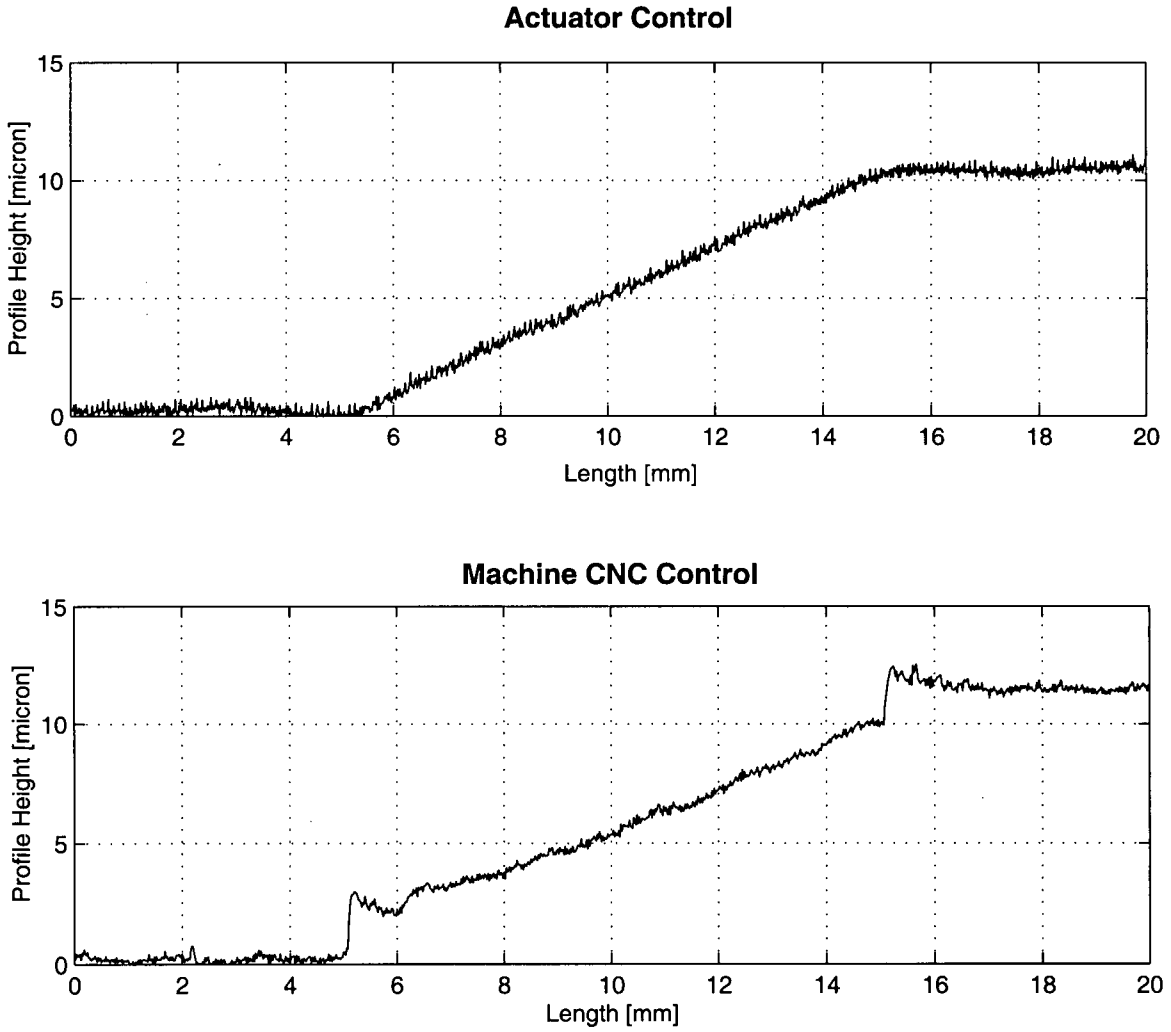

Figure 5.7 : Tapered profile for both actuator and CNC control.

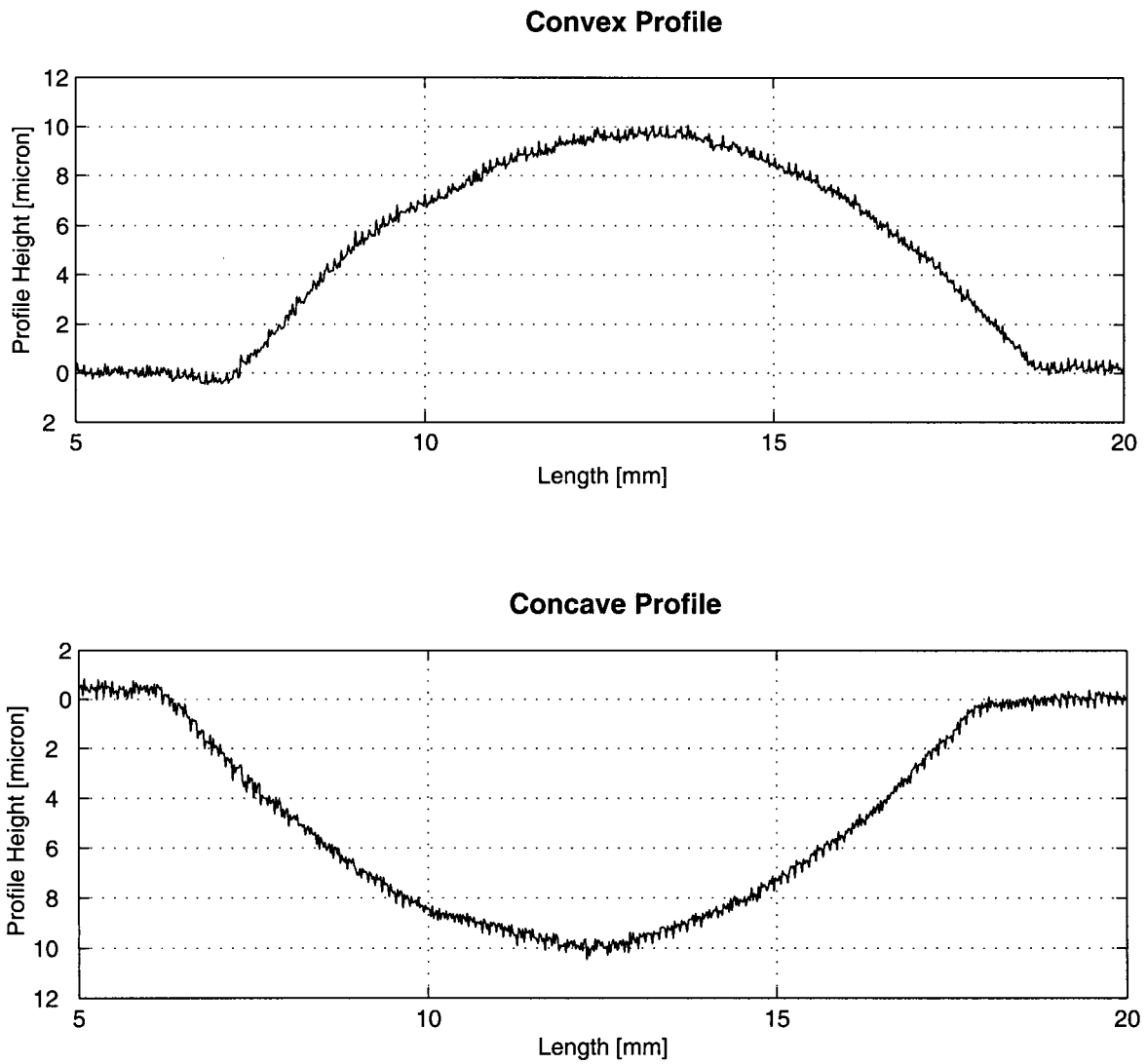

Figure 5.8 : Convex and concave surface profiles.

5.5. Surface roughness

The surface roughness after finish turning was investigated for both the mild and hardened steels. For each measured 2-D profile the analysis software corrects for inclination and edge effects to obtain the unfiltered (P) profile, and then a filter is applied to obtain the roughness (R) profile. The roughness parameters are evaluated according to the JIS JB0601-1994 standard, and are highly sensitive to the filter type and amplitude transmittance. The filter specified by the JIS standard is Gaussian, whereby the amplitude transmittance is 50% at a specified cutoff value (λ_c). The cutoff value, based on the expected range of average roughness, is set to 0.8 mm for the range 0.1 microns < R_a < 2.0 microns [61]. The evaluation length of the profile is 8 mm which is in accordance with the minimum value of 4 mm specified in the standard. The parameters investigated are the average roughness R_a, the ten point height of irregularities R_z, and the maximum peak to valley height R_y. The average roughness, commonly specified in design, provides no information as to the shape of the profile. In general R_z provides a more meaningful description of the profile than R_y, as it is determined by the sum of the average height of the five highest peaks and the average depth of the five deepest values. The surface roughness parameters were determined for cutting speeds of 150 m/min and 200 m/min, and for feed rates of 0.03 mm/rev, 0.04 mm/rev, and 0.05 mm/rev based on the recommendations of Zhu et al [32] for 4340 steel. Each cutting test consisted of a semi-finish pass at 0.1 mm depth of cut, followed by a finish pass at a depth of cut of 5 microns. The length of cut was 10 mm. As well a new insert was used for each test to reduce the effect of tool wear on achievable roughness. For each cutting condition the profile was measured at three locations around the circumference of the shaft.

The obtained surface roughness values for machining of 4340 steel (38 HRC) are presented in figures 5.9 and 5.10 for cutting speeds of 150 m/min and 200 m/min, respectively. Plotted are the mean value for each cutting condition, with the error bars indicating the scatter in values measured along the circumference of the shaft. As expected the maximum roughness R_y is slightly

higher than the average of the five highest peaks and five lowest valleys, R_z. For the given feed rates there is no effect of cutting speed on roughness. Scatter between results along the circumference is low when considering the average roughness, and a maximum of 0.3 microns when considering R_z. Feed rate had a minimal effect on roughness. The achieved average roughness is 0.25 microns, and 1.3 microns R_z.

The roughness results for hard turning of 4320 steel (60 HRC) for cutting speeds of 150 m/min and 200 m/min in figures 5.11 and 5.12, respectively. For the harder material the surface finish shows definite improvement compared with the softer material. This is explained by the reduced plasticity and softening of the harder material for the same cutting conditions. Reduction in the plasticity serves to reduce the amount of plastic flow around the tool in the feed and tangential directions, thus improving the surface texture. The average roughness for the carburized steel is as low as 0.1 microns at 0.03 mm/rev feed rate, with a corresponding R_z of 0.7 microns. The values are slightly lower at higher cutting speed, although there is not enough data to confirm this trend. Tables 5.3 and 5.4 summarize the results for all cutting conditions, along with the associated cutting lengths.

The ideal average and maximum roughness based solely on feed rate and tool nose radius (Equation 2.1) is included in Figures 5.9 through 5.12. Note that in the ideal case R_z equals R_y. For the 4340 carburized steel the results show close agreement with the ideal value at a feed rate of 0.05 mm/rev. At lower feeds the roughness values do not decrease. This may be explained by the increased fraction of the chip which has a chip thickness lower than the minimum value for chip formation (see Figure 2.6). Where the chip thickness is less than the minimum value only elastic and plastic deformation take place, and the material is ploughed by the cutting tool. Thus the achievable surface finish for the cutting tool used is limited. Decreasing the chamfer angle and increasing the sharpness of the cutting edge, effectively decreasing the rake angle, would reduce the radial force component and reduce the minimum chip thickness. In practice this may

be difficult as tool manufacturer's provide a limited range of tool geometry, and values for the cutting edge sharpness are not given.

Feed [mm/rev]	Speed [m/min]	Cutting Length [m]	R_a [micron]	R_z [micron]	R_y [micron]
0.03	150	147	0.22	1.47	1.78
0.03	200	147	0.21	1.37	1.57
0.04	150	110	0.24	1.52	1.87
0.04	200	110	0.26	1.82	2.16
0.05	150	88	0.25	1.60	1.85
0.05	200	88	0.29	1.81	2.07

Table 5.3 : Surface roughness results for 4340 steel (35-40 HRC).

Feed [mm/rev]	Speed [m/min]	Cutting Length [m]	R_a [micron]	R_z [micron]	R_y [micron]
0.03	150	157	0.13	0.82	0.94
0.03	200	157	0.11	0.70	0.79
0.04	150	118	0.12	0.75	0.85
0.04	200	118	0.12	0.74	0.81
0.05	150	94	0.14	0.83	0.89
0.05	200	94	0.12	0.80	0.90

Table 5.4 : Surface roughness results for 4320 steel (58-62 HRC).

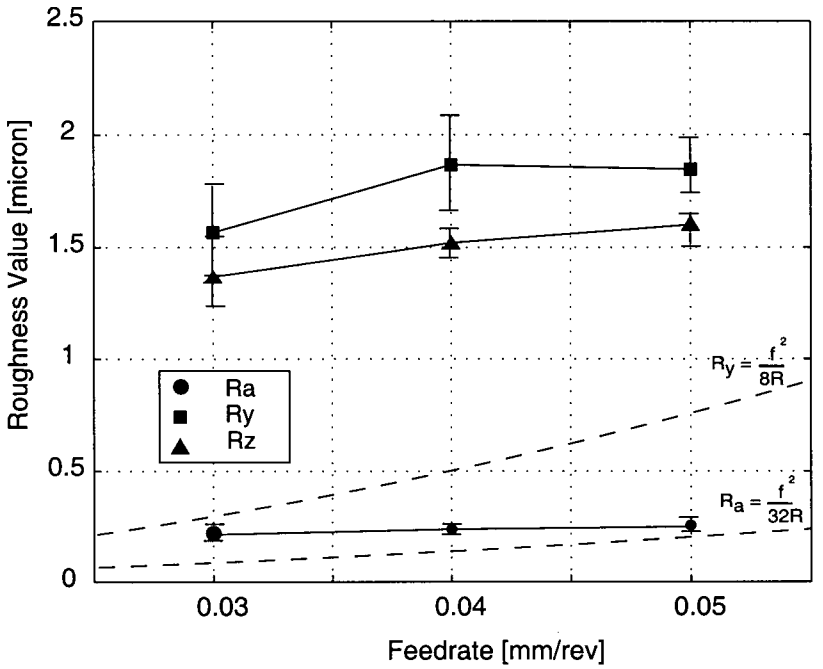

Figure 5.9 : Surface roughness of 4340 steel at 150 m/min.

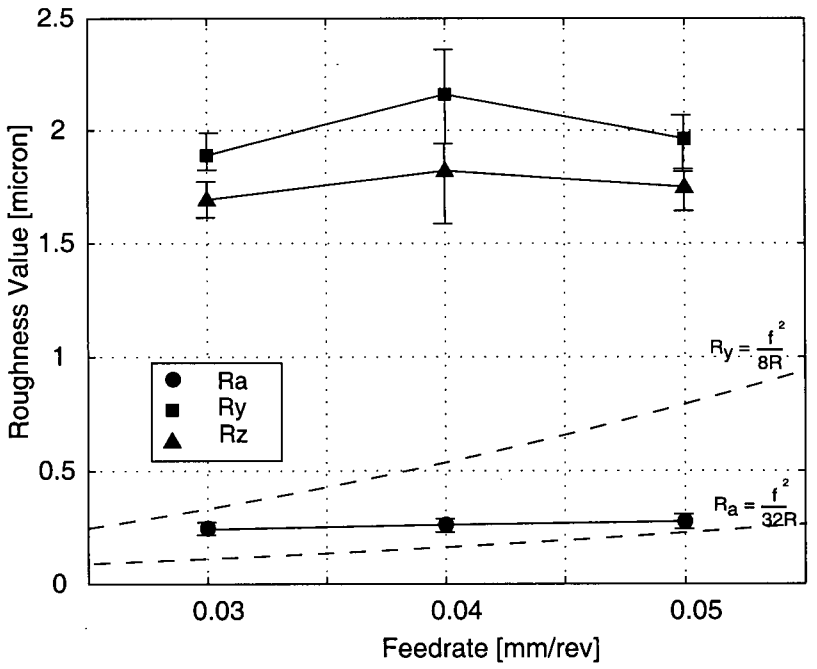

Figure 5.10 : Surface roughness for 4340 steel at 200 m/min.

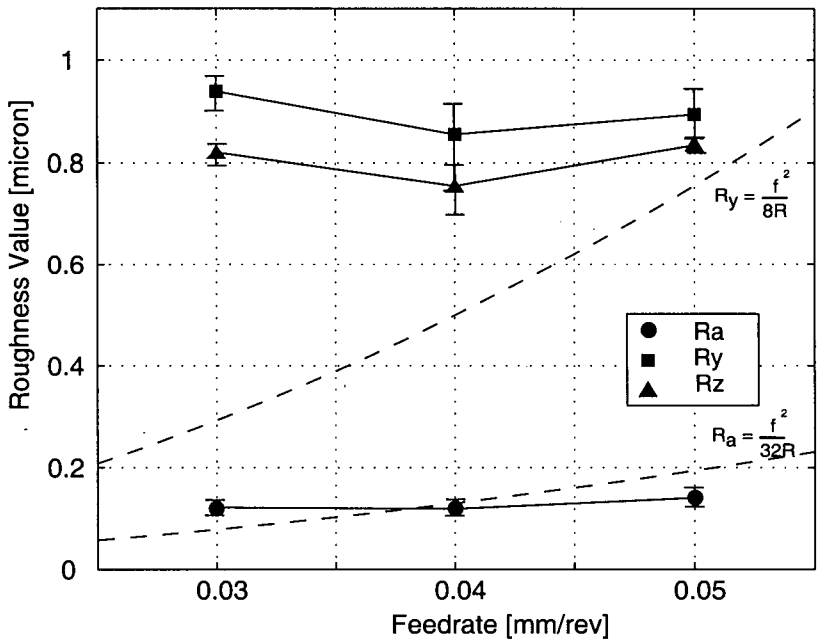

Figure 5.11 : Surface roughness for 4320 steel at 150 m/min.

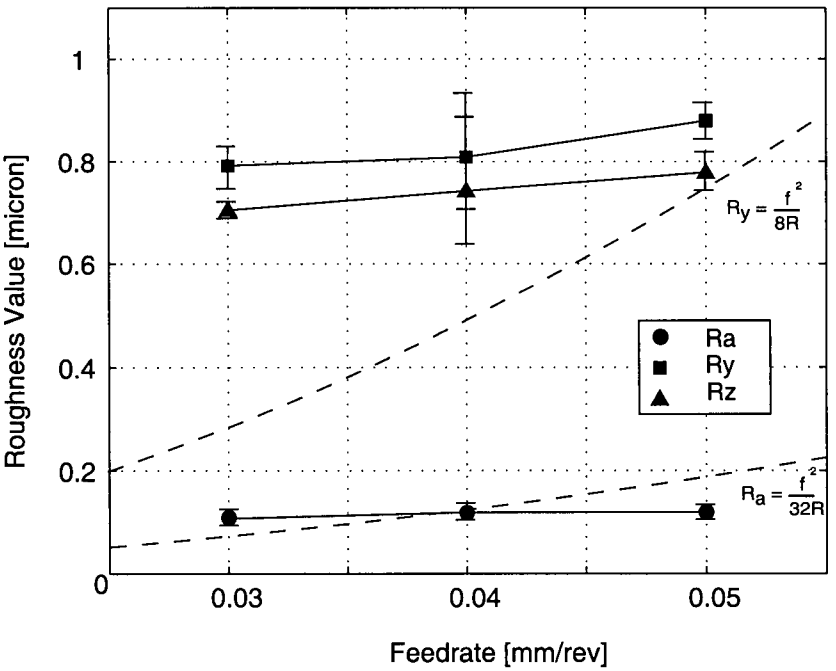

Figure 5.12 : Surface roughness for 4320 steel at 200 m/min.

5.6. Industrial application 1: Pratt & Whitney Canada

To determine the feasibility of the system in an industrial application the actuator was tested at Pratt & Whitney Canada (PWC) in Longueuil, Quebec, with the support of Manufacturing Engineering Development. The machine tool used was an Okuma LB45 two-axis horizontal CNC turning centre. The system setup is shown in Figure 5.13. The workpieces tested were medium hardness turbine shafts and disks. The current machining operations for the turbine shafts include rough turning followed by grinding. Although surface finish requirements are met in the turning operation, high diametrical tolerances cannot be met due to the positioning accuracy of the turning machine, thus the grinding operation is required. The same coated carbide cutting inserts used in production were selected. The purpose of the tests was to determine the positioning accuracy, the achievable surface roughness, as well as the logistics for practical implementation of the actuator system.

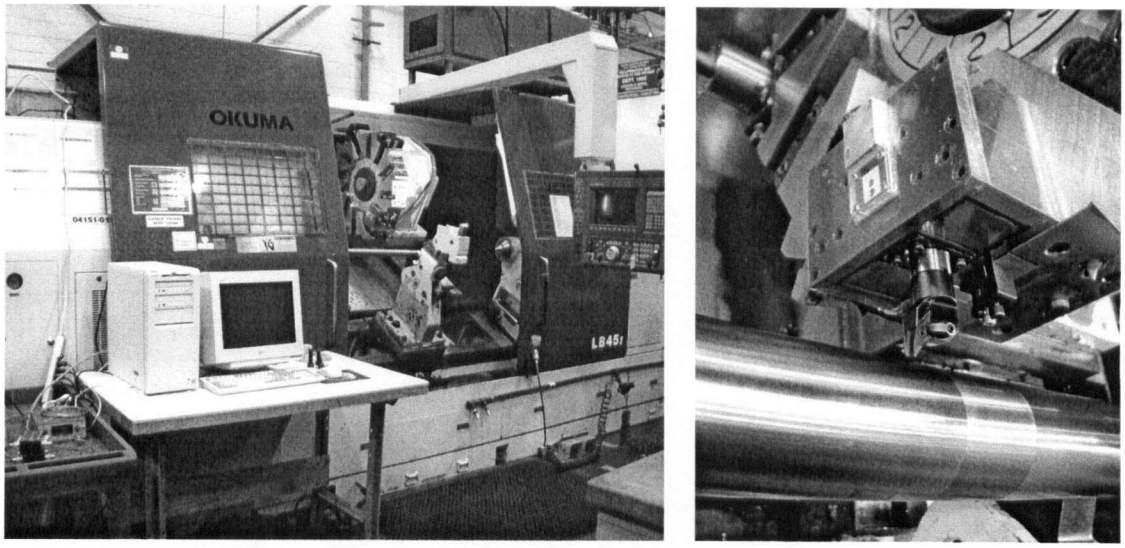

(Courtesy of Pratt & Whitney Canada)

Figure 5.13 : Actuator setup at Pratt & Whitney Canada.

Cutting tests were performed in which a step change in command position was given to the actuator. The desired shaft diameter reduction is plotted against the measured value in Figure 5.14. The actual change in shaft diameter was measured using a laser scanner. For diameter reductions greater than 10 microns the results are within 5% of the desired value. At smaller changes in depth of cut (<5 microns) there is a high degree of scatter in the results. In general the obtained results are within a few microns of the intended values. Although significant improvement was achieved compared with conventional machines, the results were worse than those achieved at MAL-UBC for hardened steel. The discrepancies may be explained by the achievable surface roughness for the tool-material pair. Extrapolating the average roughness measurements yields peak to valley roughness values of 1 to 4 microns. In measuring the size of the step change an average of several diameter measurements around the circumference of the shafts were measured before and after the step. A diameter measurement taken in the valley of the feed mark may show 2 to 8 microns difference compared to one measured on a peak, thus there is inherent error in the diameter measurement.

The average roughness of the measured surfaces are presented in Figure 5.15 for the range of feed rates $0.02 < f < 0.1$ [mm/rev], along with the ideal turned surface roughness. The trend is comparable to that of the ideal result, with roughness showing an exponential dependence on feed rate. The shifting of the obtained values is most likely due to tool wear, as well as plastic flow of the work material around the tool during the cutting process. The obtained surface finish values are within the tolerances specified by PWC. The actuator is sufficiently compact that there was no interference with other tools in the lathe turret. The main drawbacks of the system were determined to be the short stroke, limitations to subsequent cutting operations due to the interference of the actuator cabling (eg. tool changes), and the need for integration with the CNC controller of the machine.

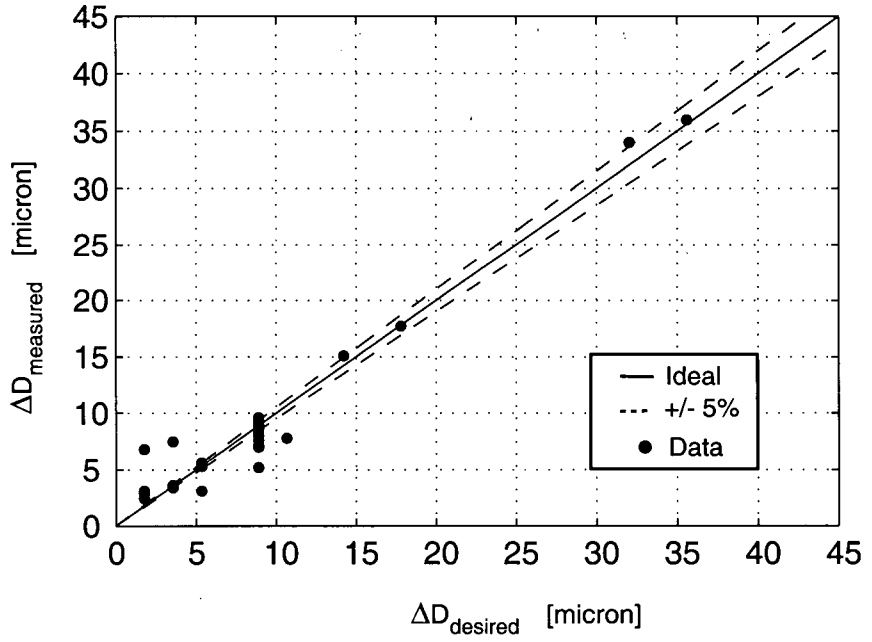

Figure 5.14 : Diameter reductions for PWC tests.

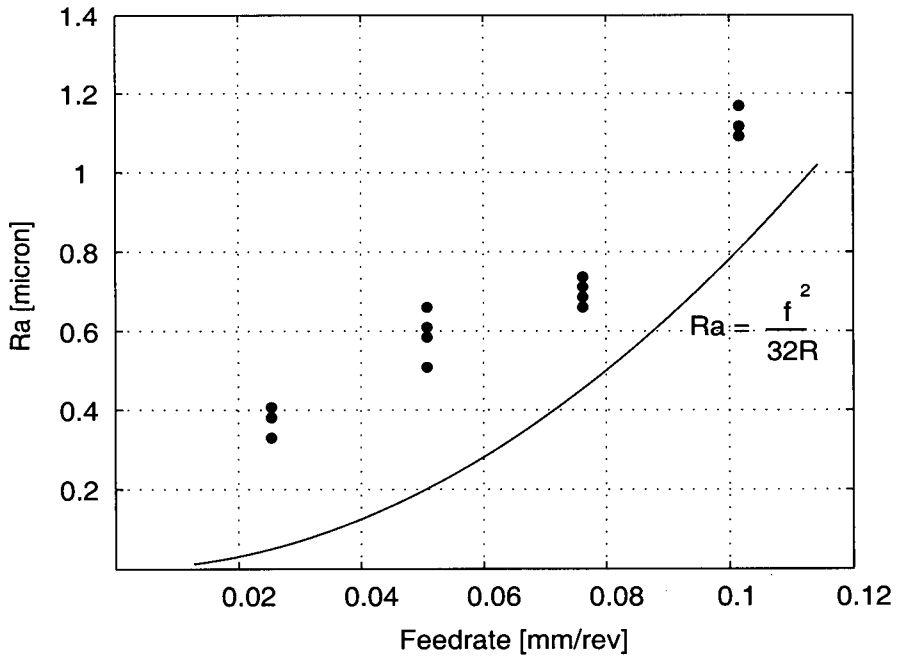

Figure 5.15 : Average roughness values for PWC tests.

5.7. Industrial application 2: Caterpillar Technical Center

Hard turning tests were performed at the Caterpillar Inc. Technical Services Division in Peoria, Illinois. The objectives were to determine the achievable surface texture, form, and surface integrity in machining roller shafts with various cutting conditions and tool geometry at low depth of cut. Currently roller shaft components are manufactured by first rough turning, followed by grinding to meet surface finish requirements. The actuator system was mounted to a five-axis Mazak Integrex 300Y turning machine as shown in Figure 5.16. An adapter plate was machined to provide an interface to the actuator body from the machine tooling system (Sandvik Capto C6). The work material was a 52 HRC alloy steel. The cutting tests comprised of rough, semi-finish, and finish turning with the same cutting insert to represent a practical amount of tool wear. The rough and semi-finish cuts were performed at 0.2 mm depth of cut, and a length of cut of 100 mm. The finishing depth of cut was 0.02 mm, for a length of 80 mm. In this way the microstructure of the semi-finish and finish pass could be compared at the same location for the same tool. The test variables considered were cutting speeds of 125 and 185 m/min, feed rates of 0.04 and 0.08 mm/rev, and tool nose radius of 0.4 and 0.8 mm. Low CBN content inserts were used, with a 0.1 mm x 20^{o} chamfer.

The average roughness results (using 50% Gaussian filter) are presented in Figure 5.17 for the 0.4 mm nose radius tool, and in Figure 5.18 for the 0.8 mm nose radius tool. Included is the ideal average roughness based on feed rate and geometry (Equation 2.1). At a feed rate of 0.08 mm/rev the average roughness shows good agreement with the ideal value. When the feed rate is decreased the roughness decreases as well, but to a lesser extent compared with the ideal. Again, this may be explained by the increased fraction of the chip having less than the minimum chip thickness at lower feed rate, causing increased ploughing of the work material. In comparison with cutting tests performed at MAL-UBC for hardened steel at the same cutting conditions and tool geometry, the results show roughness three times higher. This is attributed to the reduced

hardness of the material (52 versus 60 HRC), which allows increased plastic flow around the tool edge and increased tool wear. The cutting tests at Caterpillar had a cutting length of 1720 m (at 0.04 mm/rev feed), which is fifteen times larger than the tests conducted at MAL-UBC. The increased cutting length causes increased wear in the flank of the tool, which increases rubbing against the newly machined surface. The lowest achievable average roughness was 0.3 microns, which met the part specification.

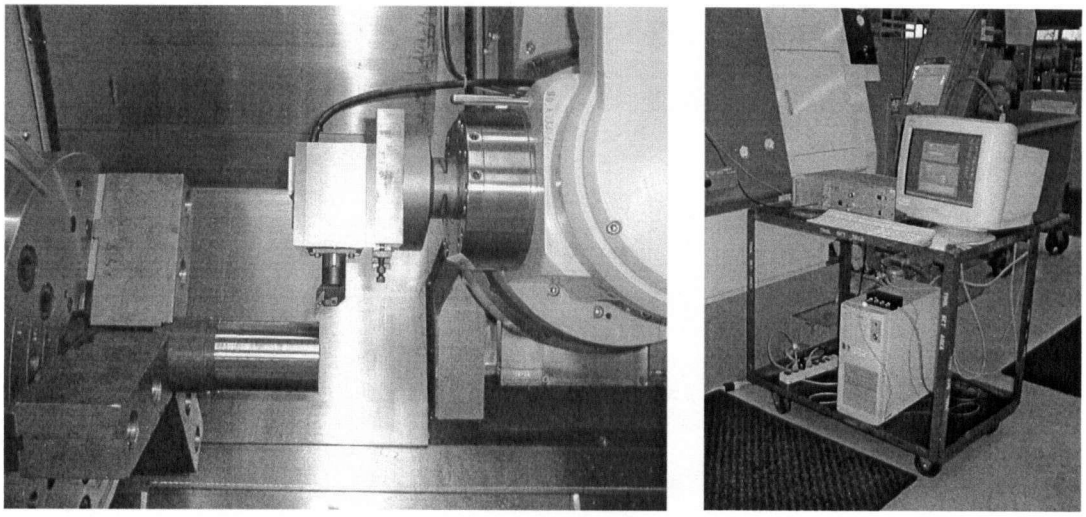

(Courtesy of Caterpillar Inc.)

Figure 5.16 : Actuator setup at Caterpillar Technical Center.

The form of the machined shafts was investigated for the actuator-machine setup. The form errors of interest were the roundness and straightness of the machined shafts. Roundness errors are attributed to spindle eccentricity, as well as tool and machine vibration. Straightness errors are the result of machine, tool, and workpiece deflection, thermal deformation, and vibration of the machine, tool, and workpiece. The effects of the piezoelectric actuator on achievable form include increased tool deflection due to the addition of flexible interfaces, increased bending

moments on the machine tool structure due to the large tool stick out in the feed direction, and any vibration of the actuator body which may be reflected as surface waviness on the part. The roundness error was measured at four locations along the length of the test shafts, and the results given in Figure 5.19. The maximum roundness is 6 microns. Straightness errors are less than 7 microns for a 78 mm length, shown in Figure 5.20. The form errors are within the part tolerances, indicating that the machine tool combined with the actuator had sufficient stiffness for precision machining of roller shafts.

The effect of low depth of cut on surface integrity was investigated by comparing the shaft microstructure in the semi-finish and finish pass. Microstructure samples were prepared by sectioning the workpieces using wire EDM (at slow feed to reduce the risk of thermal damage) and then polished and etched. The obtained microstructures are presented for depths of cut of 0.2 mm and 0.02 mm in Figures 5.20 and 5.21 for cutting speeds of 125 m/min and 185 m/min, respectively. In all cases there exist a 1-4 micron white layer, indicating that the reduced cutting forces at low depth of cut were not a factor in white layer generation. Although the residual stresses were not measured, the existence of the thin damaged surface layer indicates tensile residual stresses are expected on the shaft surface. Below the surface highly compressive stresses are expected due to the high mechanical stresses generated by the machining process. The tensile surface stresses may cause the shaft to be susceptible to the initiation of micro cracks on the surface, which would affect the part functional behaviour (wear resistance, lubrication). The effect of the white layer on fatigue life of the shaft is difficult to predict without experimental fatigue tests. From axial fatigue tests it has been argued by Smith and Melkote [28] that the white layer is simply an artifact of the machining process, and has no significant affect on the axial fatigue life of a hard turned specimen. As well Tonshoff et al [8] showed results indicating that the surface integrity had a minor influence on the fatigue life of roller bearings subjected to rolling contact loads.

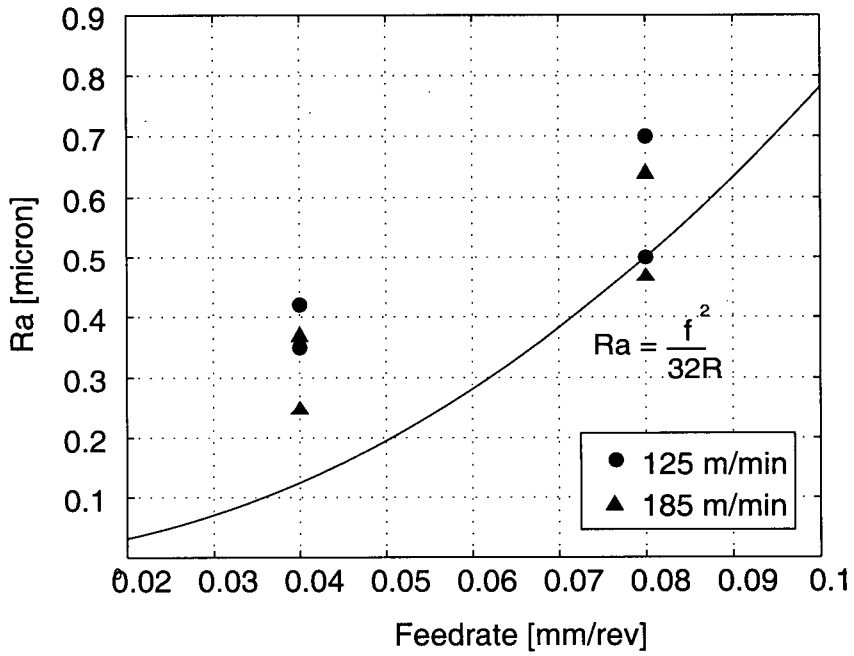

Figure 5.17 : Average roughness for Caterpillar tests, 0.4 mm nose radius.

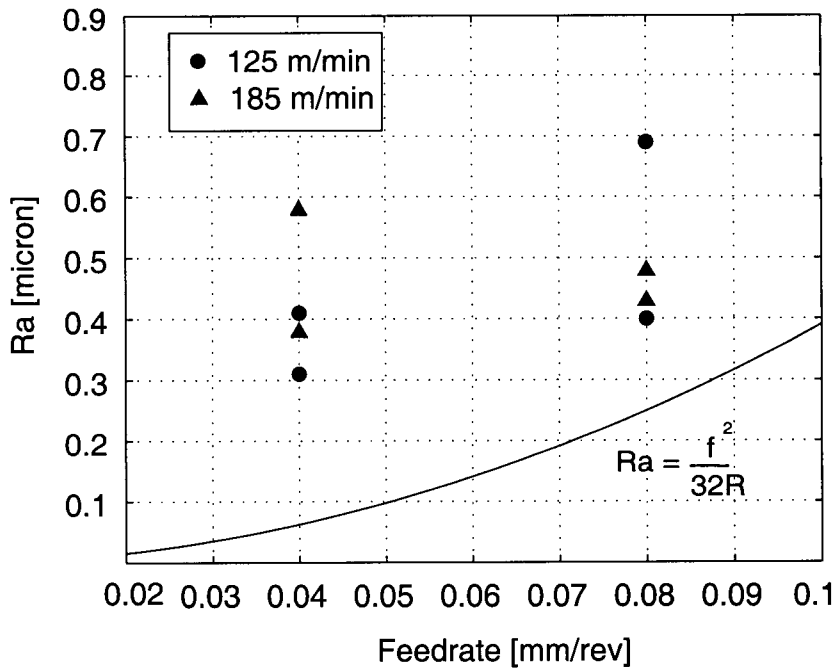

Figure 5.18 : Average roughness for Caterpillar tests, 0.8 mm nose radius.

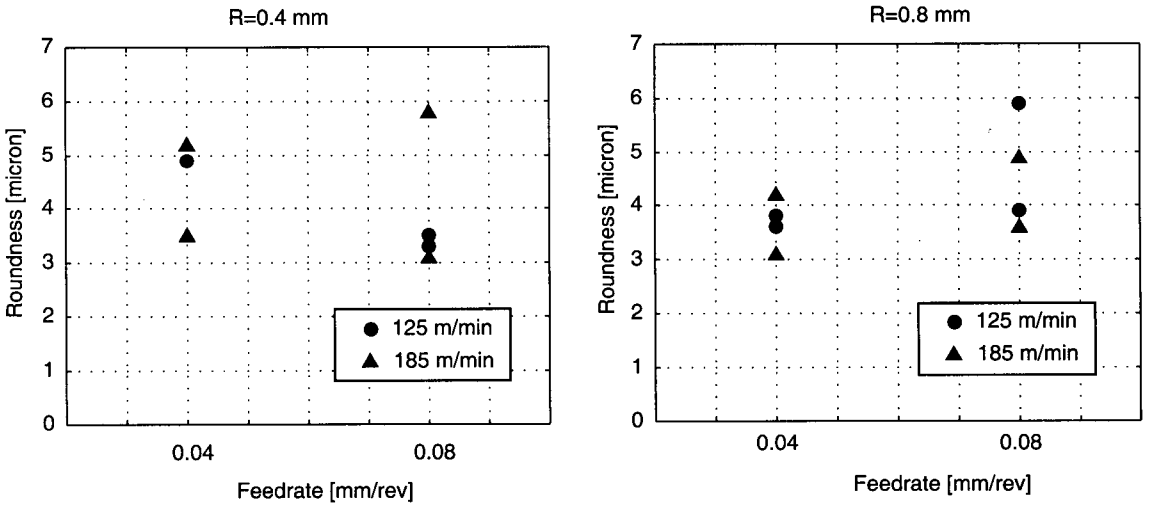

Figure 5.19 : Roundness errors for tests conducted at Caterpillar.

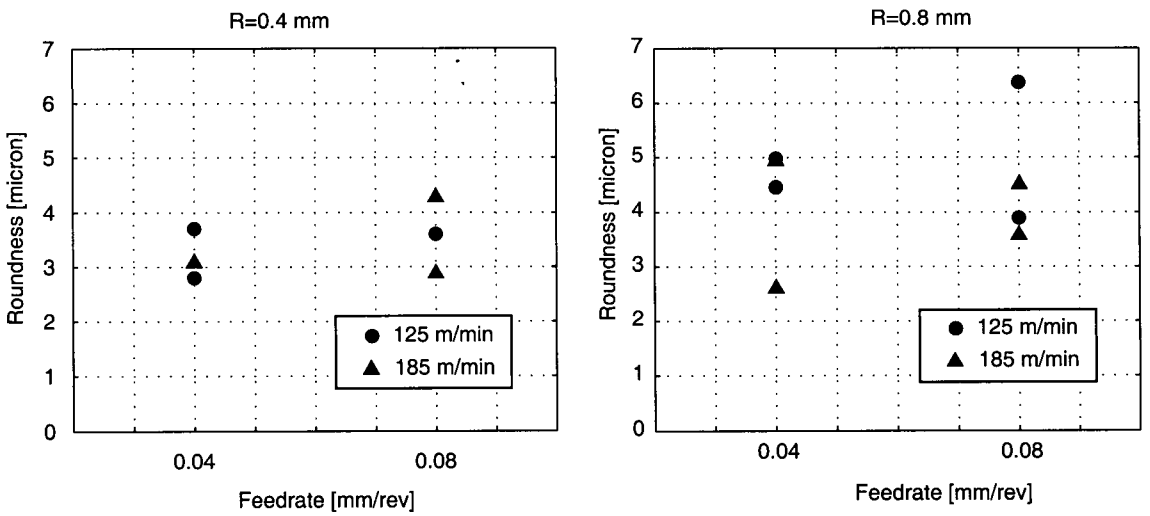

Figure 5.20 : Straightness errors for tests conducted at Caterpillar.

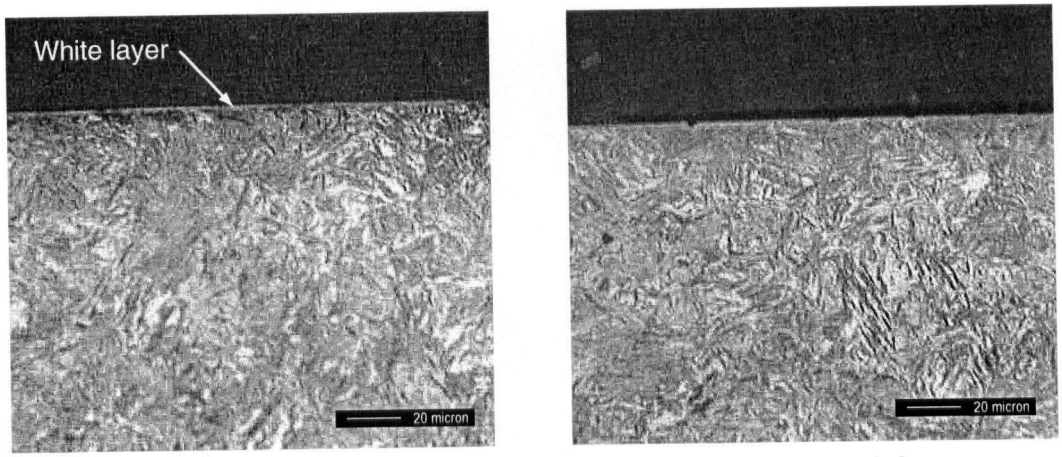

Figure 5.21 : Surface microstructure at 125 m/min, 0.4 mm nose radius.

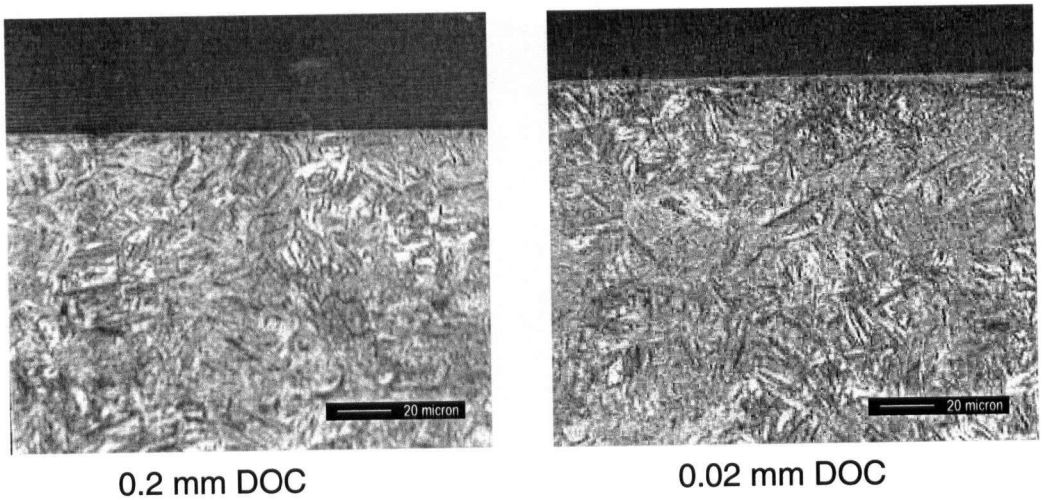

Figure 5.22 : Surface microstructure at 185 m/min, 0.4 mm nose radius.

5.8. Summary

In this chapter the experimental results obtained for precision turning using the piezoelectric actuator have been presented. In machining of a medium hardness 4340 steel the achieved positioning resolution for a finishing depth of cut of 5 microns was 0.02 microns. Investigation of the controlled position as well as the control signal shows that the sliding mode controller rejects disturbances caused by cutting forces as well as actuator non-linearity to precisely control the tool position. To ensure the commanded position to the controller is reflected as an equivalent change in depth of cut on the machine part, a series of micro profiles were machine on a hardened 4320 steel workpiece. Position step changes of 5 microns and 1 micron showed that the desired position change was achieved to a high degree of accuracy, measured using a surface analyzer. Similar precision was achieved in machining a micro taper, convex, and concave profiles. The profiles were compared to those obtained using a Hardinge precision turning centre. The precision machine showed positioning errors up to 3 microns, as well as jerky motion between linear interpolation blocks. An investigation of the attained surface roughness was performed for both the medium and high hardness steels, at low feed rates (0.03 mm/rev to 0.05 mm/rev) and high cutting speeds (150 m/min and 200 m/min). The high hardness 4320 steel showed precision quality roughness, with maximum roughness R_y less than 1 micron, and average roughness R_a of 0.1 micron. The 4340 steel showed increased roughness, due to the increased level of plasticity causing material side flow around the tool.

The actuator system was evaluated at two industrial sites, Pratt & Whitney Canada and Caterpillar Inc., for precision machining of shafts. Results from Pratt & Whitney for turbine shaft machining showed accurate tool positioning and acceptable surface finish. In precision turning of hardened roller shafts at Caterpillar Inc. no significant improvement was achieved with regards to surface texture or integrity. In this case the actuator was not a viable alternative to grinding operations.

Chapter 6

Conclusions and Recommendations

6.1. Conclusions

In this thesis, a piezoelectric tool actuator for precision turning of shafts has been designed, analyzed, manufactured, and implemented. The actuator is designed to be mounted on conventional turning machines to provide fine tool positioning otherwise not achievable due to the limitations of machine tool drives. The actuator is intended to be operated by first performing semi-finish machining in which the machine tool feed drives executes both radial and feed motions. Following the semi-finish pass the shaft diameter is measured, and compared to the design specification. The radial axis of the machine is then fixed, the actuator is retracted a small amount to clear the workpiece, and the feed motion of the machine brings the tool to the start of the cut. The final finishing depth of cut is input to the actuator, and is precisely controlled during the finishing pass. In this way the shaft is precision turned on a conventional machine, and subsequent operations on a high precision lathe or grinding machine are not required, provided the surface roughness tolerances are met.

The design of the actuator was driven by constraints on overall size (dimensions, compactness), structural properties (stiffness, natural frequency), motion (useful range and resolution, friction free), and operability (tooling, force measurement, rigid clamping). The design constraints were satisfied through design for minimal size and maximum stiffness based on optimization of parallel flexure geometry. As well careful selection of the integrated components (piezoelectric driving element, capacitive sensor, tool adapter) ensured conformance to the design constraints to provide a practical and useful system.

For control purposes the actuator was modeled as a 2^{nd} order system, based on the experimentally determined transfer function of output displacement to input force. A static gain relating input voltage to input force was assumed. Using the system model a sliding mode controller was derived. The control parameters were tuned to achieve the desired closed loop system response. The controller was implemented in discrete time domain in a Fast Cyclic Executive real-time operating system on a host PC with a control sampling frequency of 7500 Hz. The specifications of the assembled system are as follows:

- Range of motion: 36 micron
- Position control resolution: 0.020 micron (for DOC < 10 micron)
- Rise time for a step input: 10 ms
- Radial stiffness: 370 N/micron (unclamped), 626 N/micron (clamped)
- Natural frequency, radial mode: 3200 Hz (unclamped), 3870 Hz, (clamped)
- Maximum force generation: 16 000 N (at zero displacement)

The achievable surface roughness in precision finishing at a 5 micron depth of cut was investigated for medium and high hardness steels. For a feed rate range of 0.03 mm/rev to 0.05 mm/rev, and cutting speeds of 150 m/min and 200 m/min, the obtained surface roughness parameters are given below.

- AISI 4340, 36-40 HRC: R_a<0.3 micron, R_z<2.0 micron, R_y<2.2 micron
- AISI 4320, 58-62 HRC: R_a<0.15 micron, R_z<0.9 micron, R_y<1.0 micron

Through experimentation at two industrial sites, useful data on the benefits as well as the drawbacks of the actuator was gathered. The compact design of the actuator proved to be sufficient on an industrial machine, as no interference occurred with other tools in the turret. Identified drawbacks of the actuator include the limited stroke, the need for integration with CNC control, and potential tangling of the actuator cables. The achievable positioning accuracy in turning turbine shafts exceeded that of the existing turning process. Average surface roughness values were typically higher than those achieved in the laboratory, for medium hardness turbine

shafts as well as hardened roller shafts. The increase in roughness is attributed to higher levels of tool wear as the cutting lengths were greater than for the tests conducted at MAL-UBC. Finally, finishing hardened shafts at small depth of cut (0.020 mm) showed no reduction in white layer generation, indicating in this case the actuator provided no improvement over conventional machining processes.

6.2. Recommendations for future research

The practical use of the piezoelectric actuator for precision turning is limited to components with short length. With increased shaft length the effects of machine tool deformation, alignment of the translational axes, and feed drive motion become significant, and the machining process can no longer be considered a precision turning operation. In order to perform precision turning of large shafts on conventional machine tools, information of the important part features is required during machining. This is accomplished through in process gaging of the workpiece. Information such as part diameter can be input to the piezoelectric actuator controller, which can then compensate the errors (due to deflection, alignment, etc.) by updating the tool position.

Based on the evaluation of the actuator at industrial sites, it is recommended that the next generation actuator have a longer stroke, at least 60 microns, to reduce the number of semi-finish passes required for the desired depth of cut to be within the actuator stroke. As well for some profiling operations the actuator body can interfere with features on the workpiece. If an actuator is required for such an application, the design constraints should specify the maximum distance between the tool tip and the actuator body in the feed direction.

Although not the focus of this study, the achieved positioning resolution of the actuator is such that it is a likely candidate for real-time compensation of machine tool thermal drift and workpiece deflection. Given accurate and repeatable off-line measurement of machine tool and workpiece deformation, the actuator position can be updated to ensure a constant depth of cut.

References

[1] Altintas, Y., Manufacturing Automation, Cambridge University Press, New York , 2000.

[2] ASM Metals Handbook, Ed. 9, Vol. 16 Machining, 1997.

[3] Konig, W., Berktold, A., Koch, K.-F., "Turning versus grinding - a comparison of surface integrity aspects and attainable accuracies", Annals of the CIRP, Vol. 42, No. 1, pp. 39-43, 1993

[4] Rao, S. B., "Metal cutting machine tool design - a review", Transactions of the ASME Journal of Manufacturing Science and Engineering, Vol. 119, pp. 713-716, 1997.

[5] Ni, J., "CNC machine accuracy enhancement through real-time error compensation", Transactions of the ASME Journal of Manufacturing Science and Engineering, Vol. 119, pp. 717-725, 1997.

[6] Stephenson, D. A., Barone, M. R., Dargush, G. F., "Thermal expansion of the workpiece in turning", Transactions of the ASME Journal of Engineering for Industry, Vol. 117, pp. 542-550, 1995.

[7] Knuefermann, M. M. W., Read, R. F. J., Nunn, R., Clark, I. E., Fleming, M. A., "Ultra-precision turning of hardened steel with amborite DBN45 on the DeltaTurn40 lathe", Industrial Diamond Review, Vol. 2, pp. 107-113, 2000.

[8] Tonshoff, H. K., Arendt, C., Ben Amor, R., "Cutting hardened steel", Annals of the CIRP, Vol. 49, No. 2, pp. 1-19, 2000.

[9] Jochman, S., Wirtz, H., "Achieving precision grinding quality by hard turning", ASME MED Vol. 10, Manufacturing Science and Engineering, pp.817-823, 1999.

[10] Kim, J.-D., Kim, D.-S., "Waviness compensation of precision machining by piezoelectric micro cutting device", International Journal of Machine Tools & Manufacture, Vol. 38, pp. 1305-1322, 1998.

[11] Fawcett, S. C., "Small amplitude vibration compensation for precision diamond turning", Precision Engineering, Vol. 12, No. 2, pp. 91-96, 1990.

[12] De Chiffre, L, Lonardo, P., Trumpold, H., Lucca, D. A., Goch, G., Brown, C. A., Raja, J., Hansen, H. N., "Quantitative characterisation of surface texture", Annals of the CIRP, Vol. 49, No. 2, pp. 635-652, 2000.

[13] Jun, M. B.-G., "Precision turning of shafts with piezoelectric actuator tool", M.A.Sc. thesis, University of British Columbia, 2000.

[14] Shaw, M. C., Crowell, J. A., "Finish machining", Annals of the CIRP, Manufacturing Technology, Vol. 13, pp. 5-22, 1965.

[15] El-Wardany, T. I., Attia, M. H., Mohammed, E., "Surface finish in turning of hardened steel", ASME PED-Vol. 62, Engineered Surfaces, pp. 141-159, 1992.

[16] Schey, J. A., "Introduction to manufacturing processes", Ed.2, McGraw-Hill, Toronto, 1987.

[17] Kishawy, H. A., Elbestawi, M. A., "Effects of process parameters on material side flow during hard turning", International Journal of Machine Tools & Manufacture, Vol. 39, pp. 1017-1030, 1999

[18] Chen, W., "Cutting forces and surface finish when machining medium hardness steel using CBN tools", International Journal of Machine Tools & Manufacture, Vol. 40, pp. 455-466, 2000.

[19] Sata, T., "Surface finish in metal cutting", Annals of the CIRP, Manufacturing Technology, Vol. 12, pp. 190-197, 1964.

[20] El-Wardany, T. I., Mohamed, E., Elbestawi, M. A., "Material side flow in finish turning of hardened steel with ceramic tools", ASME PED Vol. 67/TRIB Vol. 4, Contact Problems and Surface Interaction in Manufacturing and Tribological Systems, pp. 159-170, 1993.

[21] Davies, M. A., Chou, Y., Evans, C. J., "On chip morphology, tool wear and cutting mechanics in finish hard turning", Annals of the CIRP, Vol. 45, No.1, pp.77-82, 1996.

[22] Poulachon, G., Moisan, A. L., "Hard turning: chip formation mechanisms and metallurgical aspects", Transactions of the ASME Journal of Manufacturing Science and Engineering, Vol. 122, pp. 406-412, 2000.

[23] Davies, M. A., Burns, T. J., Evans, C. J., "On the dynamics of chip formation in machining hard metals", Annals of the CIRP, Vol. 46, No. 1, pp.25-30, 1997

[24] Shaw, M. C., Vyas, A., "The mechanism of chip formation with hard turning steel", Annals of the CIRP, Vol. 47, No.1, pp.77-82, 1998.

[25] Thiele, J. D., Melkote, S. N., Peascoe, R. A., Watkins, T. R., "Effect of cutting edge geometry and workpiece hardness on surface residual stresses in finish hard turning of AISI 52100 steel", Transactions of the ASME Journal of Manufacturing Science and Engineering, Vol. 122, pp. 642-649, 2000.

[26] Matsumoto, Y., Hashimoto, F., Lahoti, G., "Surface integrity generated by precision hard turning", Annals of the CIRP, Vol. 48, No. 1, pp. 59-62, 1999.

[27] Ramesh, A., Thiele, J. D., Melkote, S. N., "Residual stress and sub-surface flow in finish hard turned AISI 4340 and 52100 steels: a comparative study", ASME MED-Vol. 10, Manufacturing Science and Engineering, pp. 831-837, 1999.

[28] Smith, S., Melkote, S. N., "Effects of surface integrity on fatigue life of hard turned surfaces", French-German High Speed Machining Conference, Metz, France, June 27-29, 2001.

[29] Ueda, T., Huda, M. A., Yamada, K., Nakayama, K., "Temperature measurement of CBN tool in turning of high hardness steel", Annals of the CIRP, Vol. 48, No.1, pp. 63-66, 1999.

[30] Chou, Y. K, Evans, C. J., "White layers and thermal modeling of hard turned surface", International Journal of Machine Tools & Manufacture, Vol. 39, pp. 1863-1881, 1999.

[31] Wang, J. Y., Liu, C. R., "The effect of tool flank wear on the heat transfer, thermal damage and cutting mecanics in finish hard turning", Annals of the CIRP, Vol. 48, No. 1, pp. 53-58, 1999.

[32] Zhu, W.-H., Jun, M. B., Altintas, Y., "A fast tool sevo design for precision turning of shafts on conventional CNC lathes", International Journal of Machine Tools & Manufacture, Vol. 41, pp. 953-965, 2001.

[33] Schumacher, A., "Design and manufacture of a piezo-actuator for active chatter vibration control of a turning center", Diplomarbeit, WZL-Laboratory for Machine Tools, Aachen University of Technology (RWTH), 1996.

[34] Bracht, M., "Design of a fine positioning actuator for precision turning", Diplomarbeit, Laboratory for Machine Tools and Production Engineering WZL Aachen, 1998.

[35] Sugita, K., Yamakawa, Y., Nobumitsu, H., Shibukawa, T., Kunihiko, U., "Development of a high speed non-circular turning machine using hybrid system with VCM and PZT", ASME Japan/USA Symposium on Flexible Automation, Vol. 2, 1992.

[36] Pahk, H. J., Lee, D. S., Park, J. H., "Ultra precision positioning system for servo motor-piezo actuator using the dual servo loop and digital filter implementation", International Journal of Machine Tools & Manufacture, Vo. 41, pp. 51-63, 2001.

[37] Zhu, Z., Zhang, B., "A linear piezomotor integrated by a monolithic flexural frame", Transactions of the ASME, Journal of Mechanical Design, Vol. 119, pp. 414-417, 1997.

[38] Cuttino, J. F., Miller, Jr., A. C., "Performance optimization of a fast tool servo for single-point diamond turning machines", IEEE/ASME Transactions on Mechatronics, Vol. 4, No. 2, pp. 169-178, 1999.

[39] Rasmussen, J. D., Tsao, T.-C., Hanson, R. D., Kapoor, S. G., "Dynamic variable depth of cut machining using piezoelectric actuators", International Journal of Machine Tools & Manufacture, Vol. 34, No. 3, pp. 379-392, 1994.

[40] Hara, Y., Motonishi, S., Yoshida, K., Ikawa, N., "A new micro-cutting device with high stiffness and resolution", Annals of the CIRP, Vol. 39, No. 1, pp. 375-378, 1990.

[41] Shamoto, E., Moriwaki, T., "Ultraprecision diamond cutting of hardened steel by applying elliptical vibration cutting", Annals of the CIRP, Vol. 48, No. 1, 1999.

[42] Okazaki, Y., "A micro-positioning tool post using a piezoelectric actuator for diamond turning machines", Precision Engineering, Vol. 12., No. 3, pp. 151-156, 1990.

[43] Kim, J.-D., Nam, S.-R., "Development of a micro-depth control system for an ultra-precision lathe a piezo-electric actuator", International Journal of Machine Tools & Manufacture, Vo. 37, No. 4, pp. 495-509, 1997.

[44] Hanson, R. D., Tsao, T.-C., "Development of a fast tool servo for variable-depth-of-cut machining", ASME Dynamic Systems and Control, Vol. 2, pp. 863-871, 1994.

[45] Schellekens, P., Rosielle, N., Vermeulen, J., Vermeulen, M., Wetzels, S., Pril, W., "Design for precision: current status and trends", Annals of the CIRP, Vol. 47, No. 2, pp.557-586, 1998.

[46] Her, I., Chang, J. C., "A linear scheme for the displacement analysis of micropositioning stages with flexure hinges", Transactions of the ASME Journal of Mechanical Design, Vol. 116, pp. 770-776, 1994.

[47] Xiaowei, L., Zhixin, J., Jiaqi, Z., Jinchun, L., "A combined electrical machining process for the production of a flexure hinge", Journal of Materials Processing Technology, Vol. 71, pp. 373-376, 1997.

[48] Xu, G., Qu, L., "Some analytical problems of high performance flexure hinge and micromotion stage design", Proceedings of the IEEE International Conference on Industrial Technology, 1996.

[49] Xu, W., King, T. G., "Mechanical amplifier design for piezo-actuator applications", IEE Colloquium (Digest), No. 170, pp.1-5, 1995.Ryu, J. W., Gweon, D.-G., "Error analysis of a flexure hinge mechanism induced by machining imperfection", Precision Engineering, Vol. 21, pp. 83-89, 1997.

[50] Ryu, J. W., Gweon, D.-G., "Error analysis of a flexure hinge mechanism induced by machining imperfection", Precision Engineering, Vol. 21, pp.83-89, 1997.

[51] Furukawa, E., Mizuno, M, Doi, T., "Development of a flexure-hinged translation mechanism driven by two piezoelectric stacks", JSME International Journal Series C, Vol. 38, No. 4, pp. 743-748, 1995.

[52] Ryu, J. W., Gweon, D.-G., Moon, K. S., "Optimal design of a flexure hinge based XYθ wafer stage", Precision Engineering, vo. 21, pp. 18-28, 1997.

[53] Yang, R., Jouaneh, M., "Design and analysis of a low profile micro-positioning stage", Precision Machining: Technology and Machine Development and Improvement, ASME PED, Vol. 58, pp. 131-142, 1992.

[54] Paros, J. M., Weisbord, L., "How to design flexure hinge", Machine Design, Vo. 37, pp. 151-157, 1965.

[55] Hibbeler, R. C., Mechanics of Materials, Ed. 2, Prentice Hall, New Jersey, 1994.

[56] Blau, P. J., "Friction science and technology", Marcel Dekker Inc., New York 1996.

[57] Otkunc, B. C., "Open architecture controllers: real-time capabilities and interopterability", M.A.Sc. thesis, University of British Columbia, 2000.

[58] Gajic, Z., Qureshi, M. T. J., "Luyapunov matrix equation in system stability and control", Academic Press, 1995.

[59] Zhu, W. H., Chen, H.-T., Zang, Z.-J., "A variable structure robot control algorithm with an observer", IEEE Transactions on robotics and automation, Vol. 8, No.4, pp.485-492, 1992.

[60] Astrom, K. J., Wittenmark, B., Computer Controlled Systems - Theory and Design, Prentice Hall International Inc., Toronto, 1997.

[61] Mitutoyo Surpak User's Manual, No. 4796-3GB, Series No. 178, Surface Texture Parameter.